

## TABLE OF CONTENTS

<b>Table of Contents</b>	<b>i</b>
	<b>Page</b>
<b>Introduction</b>	<b>1</b>
<b>1 High energy nuclear physics</b>	<b>3</b>
1.1 Standard model . . . . .	3
1.1.1 Quantum chromodynamics . . . . .	5
1.1.2 Parton distribution functions . . . . .	9
1.1.3 QCD phase diagram . . . . .	13
1.2 Relativistic heavy-ion physics . . . . .	15
1.2.1 History of heavy-ion accelerators . . . . .	15
1.2.2 Geometry of nucleus-nucleus collisions . . . . .	17
1.2.3 Evolution of heavy-ion collisions . . . . .	19
1.2.4 Experimental probes of the QGP . . . . .	21
<b>2 Experimental setup</b>	<b>33</b>
2.1 The Large Hadron Collider . . . . .	33
2.1.1 LHC heavy-ion schemes in 2015-2016 . . . . .	37
2.2 The Compact Muon Solenoid . . . . .	39
2.2.1 Subdetectors . . . . .	42
2.2.2 Trigger system . . . . .	50
2.2.3 Reconstruction . . . . .	57
<b>3 Charmonia</b>	<b>63</b>
3.1 Theory . . . . .	63
3.2 Analysis . . . . .	63
3.3 Results . . . . .	63

---

**TABLE OF CONTENTS**

---

<b>4 W BOSON PRODUCTION IN PROTON-LEAD COLLISIONS</b>	<b>65</b>
4.1 Theory . . . . .	66
4.1.1 History of weak theory . . . . .	66
4.1.2 Electroweak theory . . . . .	69
4.1.3 Nuclear PDF . . . . .	71
4.1.4 PDF global fits . . . . .	72
4.1.5 Production of W bosons at LHC . . . . .	75
4.2 W boson production in pPb collisions at $\sqrt{s_{\text{NN}}} = 8.16 \text{ TeV}$ . . . . .	79
4.2.1 Observables . . . . .	79
4.2.2 Comparison with theoretical models . . . . .	81
4.2.3 Comparison with other LHC experiments . . . . .	83
<b>5 Conclusion</b>	<b>87</b>
<b>Bibliography</b>	<b>89</b>
<b>List of Tables</b>	<b>103</b>
<b>List of Figures</b>	<b>105</b>

## **INTRODUCTION**



## HIGH ENERGY NUCLEAR PHYSICS

This chapter introduces the concepts of high energy nuclear physics relevant for the analysis of the production of W bosons and J/ $\psi$  mesons in heavy-ion collisions.

The elementary particles and fundamental interactions of the standard model are described in Section 1.1. In addition, the extreme state of hot dense hadronic matter known as the Quark-Gluon Plasma (QGP) and the study of its properties in heavy-ion collisions is reviewed in Section 1.2.

### 1.1 Standard model

The standard model (SM) is a theoretical framework that describes the properties of elementary particles and their interactions. The SM was developed during the 20th century through the collaborative effort of many physicists. According to the SM, all matter in the universe is composed, at the most fundamental level, of elementary particles called fermions. Fermions are particles with half-integer spin which behave according to Fermi-Dirac statistics formulated by Enrico Fermi [1] and Paul Dirac [2] in 1926. As a consequence, fermions are restricted by the Pauli exclusion principle [3] which dictates that two or more fermions with the same quantum numbers cannot occupy the same quantum state.

In addition, fermions can be classified as leptons or quarks. There are six leptons arranged in three "generations": the electron ( $e^-$ ) and the electron neutrino ( $\nu_e$ ), the muon ( $\mu^-$ ) and the muon neutrino ( $\nu_\mu$ ), and the tau ( $\tau^-$ ) and the tau neutrino ( $\nu_\tau$ ).

The neutrinos are electrically neutral and almost massless, while the other leptons have negative electric charge (-1) and sizeable masses. In the case of quarks, there are six "flavours" paired also in three generations of increasing mass. The up and down quarks belong to the first generation, while the more heavier quarks are included in the second generation (charm and strange quarks) and third generation (top and bottom quarks). The up (u), charm (c) and top (t) quarks have positive electric charge (+2/3) while the down (d), strange (s) and bottom (b) quarks have negative electric charge (-1/3). Each quark also carry another quantum number called colour charge that can have three different values labelled as red, green and blue. Moreover, each fermion has an associated antiparticle with the same mass but with opposite charges. The positron ( $e^+$ ) is the antiparticle of the electron, while the name of the rest of antiparticles simply starts with the prefix "anti" (e.g. anti-quarks  $\bar{q}$ , anti-neutrinos  $\bar{\nu}$  or anti-leptons  $\ell^+$ ).

The interactions between fermions are described in the standard model by three fundamental forces: electromagnetism, strong nuclear force and the weak nuclear force. The gravitational force is currently not included in the SM but the effect of gravity at the quantum level is so small that it is considered negligible. In the SM, each fundamental force is mediated by the exchange of integer spin particles called bosons that follows the Bose-Einstein statistics proposed in 1924 by Sateyndra Bose [4] and Albert Einstein [5].

The electromagnetic and the weak nuclear forces are described in the SM by the electroweak theory. The electromagnetic interactions between particles with electric charge are mediated by photons which are massless and chargeless spin one particles. On the other hand, the weak interactions can act on all fermions but the strength of the weak force is roughly  $10^{-5}$  weaker than the electromagnetic force. The weak interactions are mediated by three massive vector bosons: the electrically charged  $W^\pm$  bosons and the electrically neutral Z boson. Processes involving neutrinos or the change of quark flavour are only possible through weak interactions. Moreover, the strong nuclear force is responsible for the interactions between colour charged particles (i.e. quarks) described by the theory of Quantum Chromodynamics (QCD). The strong interactions are mediated by spin one bosons called gluons which carry colour and anti-colour charge. Thus, unlike the photon, gluons can interact with themselves confining the quarks in colourless configurations known as hadrons. Hadrons compose of three (anti-)quarks are called baryons while those made of a quark and an anti-quark are called mesons. Exotic hadrons containing four and five quarks have been recently observed by the Belle [6] and LHCb [7] collaborations, respectively.

The generation of mass of the elementary particles is explained in the SM by the

Brout-Englert-Higgs (BEH) mechanism [8, 9]. The weak bosons and the fermions acquire their mass by interacting with the Higgs field. The stronger a particle couples to the Higgs field, the more massive it becomes. The interaction with the Higgs field is mediated by a scalar boson, the so-called Higgs boson. The BEH mechanism was experimentally confirmed after the CMS [10] and ATLAS [11] collaborations announced the discovery of the Higgs boson in 2012. The basic properties of leptons, quarks and bosons of the SM are summarized in Table 1.1.

	Name	Symbol	Mass	Charge	Spin	Interactions	
Quark	$1^{st}$	Up	u	2.2 MeV	2/3	1/2	All
		Down	d	4.7 MeV	-1/3	1/2	All
	$2^{nd}$	Charm	c	1.28 GeV	2/3	1/2	All
		Strange	s	96 MeV	-1/3	1/2	All
	$3^{rd}$	Top	t	173.5 GeV	2/3	1/2	All
		Bottom	b	4.18 GeV	-1/3	1/2	All
Lepton	$1^{st}$	Electron	$e^-$	511 keV	-1	1/2	Electroweak
		Electron neutrino	$\nu_e$	<2 eV	0	1/2	Weak
	$2^{nd}$	Muon	$\mu$	106 MeV	-1	1/2	Electroweak
		Muon neutrino	$\nu_\mu$	<2 eV	0	1/2	Weak
	$3^{rd}$	Tau	$\tau$	1.78 GeV	-1	1/2	Electroweak
		Tau neutrino	$\nu_\tau$	<2 eV	0	1/2	Weak
Boson	Photon	$\gamma$	$< 10^{-18}$ eV	0	1	Electromagnetic	
	Gluon	g	0	0	1	Strong	
	W boson	$W^\pm$	80.4 GeV	$\pm 1$	1	Electroweak	
	Z boson	Z	91.2 GeV	0	1	Electroweak	
	Higgs boson	H	125.1 GeV	0	0	BEH mechanism	

Table 1.1: Basic properties of quarks, leptons and bosons from the SM. The table includes the mass, electric charge, spin and type of interactions of each particle. The values are taken from Ref. [12]

### 1.1.1 Quantum chromodynamics

The development of new experimental techniques, such as the synchrocyclotron and the bubble chamber, led to the discovery of many hadronic resonances during the 1950s and 1960s. In an attempt to organize these new hadrons, Murray Gell-Mann [13] and Yuval Ne'eman [14] proposed in 1961 the Eightfold Way classification. The Eightfold Way scheme managed to sort the hadrons into representations of the SU(3) group leading to

the creation of the quark model. The quark model, developed in 1964 by Gell-Mann [15] and George Zweig [16], considered the hadrons as composite objects made of valence quarks and anti-quarks. Even though the quark model was successful at describing the properties of most hadrons known at the time, it had problems explaining the structure of the  $\Omega^-$  baryon. The  $\Omega^-$  baryon is made of three strange quarks with parallel spins but such configuration was forbidden by the Pauli exclusion principle. To solve the spin-statistics paradox, Oscar Greenberg [17] proposed that each quark also carried a 3-valued quantum number named the colour charge. The description of the strong interactions using the concept of colour charges was formally developed in the theory of QCD by Harald Fritzsch, Heinrich Leutwyler and Murray Gell-Mann [18] in 1973.

Quantum chromodynamics is a non-abelian quantum field theory with gauge symmetry group  $SU(3)$ , that describes the strong interactions between colour charged particles. The primary objects of QCD are the quarks which carry one colour charge (e.g. green) and the gluons which carry a colour and an anti-colour charge (e.g. red-antiblue). There are eight different gluons which form an octet representation of  $SU(3)$ . The lagrangian of QCD is:

$$L_{QCD} = \sum_f \bar{q}_{f,i} \left( i\gamma^\mu D_\mu^{i,j} - m_f \delta^{a,b} \right) q_{f,j} - \frac{1}{4} F_{\mu,\nu}^a F_a^{\mu,\nu} \quad (1.1)$$

where  $g_s$  is the strong gauge coupling constant, and  $\gamma^\mu$  are the Dirac  $\gamma$ -matrices. The  $q_{f,i}$  represents the Dirac spinor of a quark with flavour  $f$ , mass  $m_f$  and colour index  $i$  running from  $i = 1$  to 3. The QCD gauge covariant derivative  $D_\mu^{i,j}$  and the gluon field strength tensor  $F_{\mu,\nu}^a$  are given by:

$$\begin{aligned} D_\mu^{i,j} &= \delta^{i,j} \partial_\mu - i \frac{g_s}{2} \lambda_a^{i,j} G_\mu^a \\ F_{\mu,\nu}^a &= \partial_\mu G_\nu^a - \partial_\nu G_\mu^a + g_s f_{bc}^a G_\mu^b G_\nu^c \end{aligned} \quad (1.2)$$

where  $f_{bc}^a$  are the  $SU(3)$  structure constants,  $\lambda_a^{i,j}$  are the Gell-Mann matrices, and  $G_\mu^a$  is the vector field of a gluon with index  $a$  that runs from  $a = 1$  to 8.

Expanding the terms in Eq. (1.1), one can derive three different types of vertices representing the interaction between quarks and gluons, and the gluon self-interactions as shown in Fig. 1.1.

### 1.1.1.1 Running coupling constant

In quantum field theory, physical quantities are calculated by performing a perturbative expansion of the theory in terms of its coupling constant. The first order of the expansion

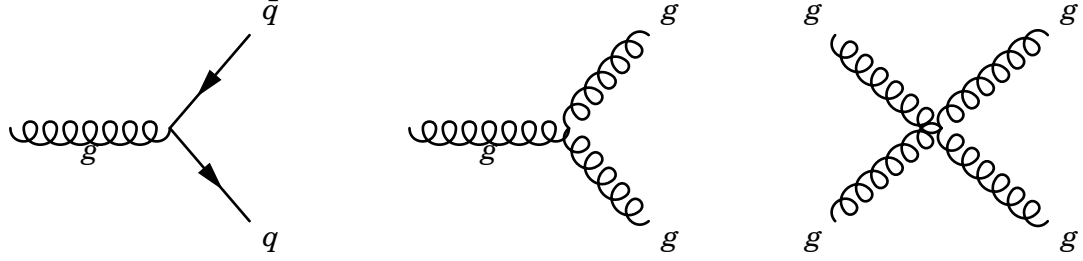


Figure 1.1: Feynman diagrams of the QCD vertices for quark-gluon coupling (left), triple gluon self-coupling (middle) and quadri gluon self-coupling (right).

is called the leading order (LO). At higher orders, some of the terms contain loops (infinite integrals) which diverge due to high momentum particles in the loop (ultraviolet divergence). The ultraviolet (UV) divergences can be removed from the perturbation series by renormalizing the Lagrangian.

The renormalization procedure consist of replacing the bare parameters of the Lagrangian by finite renormalized parameters, and then treat the divergences by applying a regularization scheme. There are many regularization schemes but one of the most often used is the Minimal Substraction (MS) scheme based on dimensional regularization. The MS scheme consists on solving the loop integrals in  $d$  arbitrary spacetime dimensions introducing a scale  $\mu$  in the process [19]. In order to keep the physical observables independent of the renormalization scale, the dependence of the renormalized parameters on the scale  $\mu$  is fixed by renormalization group equations (RGE) [19].

In the case of QCD, the strength of the strong interactions is parametrized by the strong coupling constant  $\alpha_s = 4\pi g_s^2$ . The UV divergences in perturbative QCD (pQCD) appears from loop diagrams like those shown in Fig. 1.2.

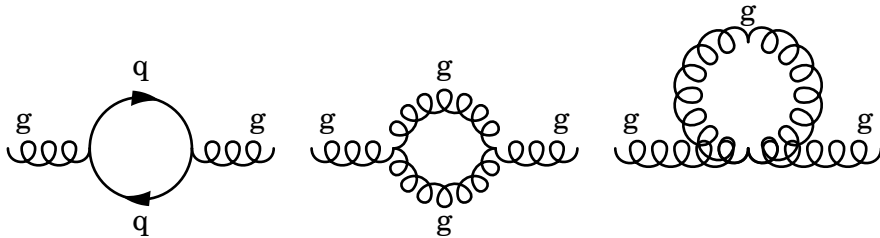


Figure 1.2: Feynman diagrams of 1-loop contributions to pQCD.

The renormalized strong coupling constant  $\alpha_s(\mu^2)$  satisfies the following RGE [12]:

$$\mu^2 \frac{d\alpha_s(\mu^2)}{d\mu^2} = \beta(\alpha_s) = -\alpha_s^2 (\beta_0 + \beta_1 \alpha_s + \dots) \quad (1.3)$$

where  $\beta_0 = 7/(4\pi)$  and  $\beta_1 = 13/(8\pi^2)$  are the 1-loop and the 2-loop coefficients of the  $\beta$ -function, respectively [12]. In the one-loop approximation,  $\alpha_s(\mu^2)$  can be expressed as:

$$\alpha_s(\mu^2) = \frac{1}{\beta_0 \ln\left(\frac{\mu^2}{\Lambda_{\text{QCD}}^2}\right)} \quad (1.4)$$

where  $\Lambda_{\text{QCD}}$  is the QCD Landau pole (i.e. the scale at which the coupling becomes infinite). The factorization scale  $\mu$  is generally associated to the energy scale  $Q$  of a given process. This means that  $\alpha_s(\mu^2)$  is not really a constant but depends on the energy scale, so it is also known as the QCD running coupling constant. Fig. 1.3 presents the latest results on the measurement of  $\alpha_s(Q^2)$  as function of the energy scale  $Q$  [12].

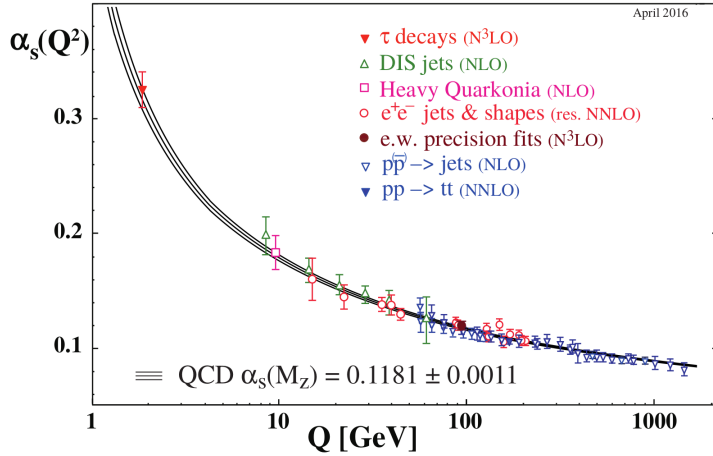


Figure 1.3: Summary of measurements of  $\alpha_s$  as a function of the energy scale  $Q$ . Figure taken from the PDG [12]

### 1.1.1.2 Asymptotic freedom

One important consequence of the non-abelian nature of QCD is the asymptotic freedom of colour charged particles discovered in 1973 by David Gross and Frank Wilczek [20], and also by David Politzer [21]. As can be observe in Fig. 1.3, the strength of the strong nuclear force gets asymptotically reduced as the energy scale is increased. Perturbative QCD can then be fully applied in the asymptotic free regime since the strong coupling constant is small.

Considering the inverse relation between the wavelength of particles and their momentum (de Broglie hypothesis [22]), asymptotic freedom implies that the strong nuclear interactions between quarks gets weaker at larger momentum or at shorter distances. This phenomenon can be understood qualitatively as derived from the interaction with the QCD vacuum. The presence of virtual quark-antiquark pairs from the vacuum acts as colour dipoles reducing (screening) the strength of the colour charge field. In addition, virtual gluons can couple to other gluons increasing (antiscreening) the net effect of the colour charge seen at larger distances. Thus, there is an interplay between quark-antiquark pair colour screening and gluon colour antiscreening, where the later effect dominates in QCD.

#### 1.1.1.3 Colour confinement

The fact that quarks and gluons have never been observed isolated in normal conditions is due to another phenomenon of QCD called colour confinement. The intensity of the strong nuclear force increases when the energy scale is reduced or the distance is increased as seen in Fig. 1.3. The large strong interactions between colour charged particles force the quarks and gluons to be confined in hadrons. The divergent behaviour of  $\alpha_s$  at the Landau pole shown in Eq. (1.4), is a consequence of the inability of pQCD to describe the low energy regime which becomes non-perturbative. An alternative way to study the low energy regime is to use Lattice QCD calculations.

The strong nuclear force can be described qualitatively as a string. When a quark and anti-quark gets separated, the gluon string that mediates their strong interaction elongates increasing the energy. The string eventually breaks when it becomes more energetically favorable to create a light quark-antiquark pair, splitting the original meson into two mesons as shown in Fig. 1.4. This leads to a process called hadronization where quarks and gluons produce a cascade of hadrons. The presence of colour charged particles in high energy collisions can be measured experimentally using jets derived by clustering the final state hadrons in narrow cones.

#### 1.1.2 Parton distribution functions

The production of particles in hadronic collisions depends on the evolution of the partons (i.e. quarks and gluons) inside the hadrons and the parton momentum transfer during the hard scattering. Since the strong coupling constant decreases with increasing momentum scales, partons can be considered asymptotically free within the hadron during collisions

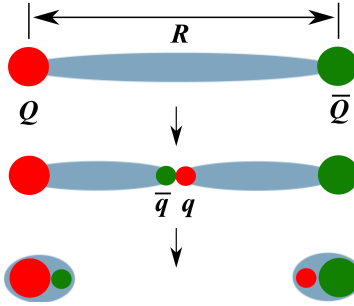


Figure 1.4: Sketch of the gluon string breaking between a quark  $Q$  and an anti-quark  $\bar{Q}$  due to  $q\bar{q}$  pair creation. Figure taken from Ref. [23]

involving large momentum transfer. In this case, each parton carries a fraction of the total momemtum of the hadron, represented by the quantity called Bjorken  $x$  [24] (labelled simply as  $x$ ), given by:

$$p_{parton} = x p_{proton} \quad (1.5)$$

The quantum properties of the hadrons, such as the electric charge or spin, are derived from the valence quarks. The interaction between valence quarks is mediated by the exchange of gluons. Gluons can also produce virtual quark-antiquark pairs and other gluons through self interactions. The virtual quarks produced inside the hadrons are called sea quarks. The gluons and sea quarks do not contribute to the quantum numbers of the hadrons but they play a key role in the interaction of hadrons with other particles.

A convenient way of studying the evolution of partons within hadrons is through the parton distribution functions (PDFs). The PDF of a hadron represents the probability that a parton carries a given fraction  $x$  of the total momemtum of the hadron.

According to the QCD factorization theorem, the cross section of a given hard scattering process in hadronic collisions can be factorized into a partonic cross section times the PDFs of each incoming hadron. The advantage of the factorization theorem is that the partonic cross section can be derived using perturbative QCD and does not depend on the colliding hadrons. On the other hand, the PDFs can not be currently calculated from first principles due to the non-perturbative nature of QCD, but they can be determined from global fits to experimental data since the PDFs are independent of the initial scattering process (i.e. universal). The hadronic cross section in a given final state can be expressed at LO, using the factorization theorem, as:

$$\sigma_{h_1, h_2} = \sum_{f_1, f_2 = (q, \bar{q}, g)} \int_0^1 dx_1 dx_2 f_1^{h_1}(x_1, Q^2) f_2^{h_2}(x_2, Q^2) \hat{\sigma}_{f_1 f_2} \quad (1.6)$$

where  $Q^2$  is the momentum scale,  $f^{h_1}(x, Q^2)$  is the PDF of a given incoming hadron  $h_1$ , and  $\hat{\sigma}_{f_1 f_2}$  represents the partonic cross section of the scattering process between partons  $f_1$  and  $f_2$ .

The  $Q^2$  scale dependence of the PDFs is described by the parton evolution equations developed by Dokshitzer, Gribov, Lipatov, Altarelli and Parisi (DGLAP) [25–27]. In the DGLAP formalism, the PDFs can be expressed in terms of kernels  $P_{q_1 q_2}$  (called splitting functions), and the evolution equations of the parton densities can be written as:

$$\begin{aligned} \frac{d}{dt} q_i(x, t) &= \frac{\alpha_s(Q)}{2\pi} [q_i \circledast P_{qq} + g_i \circledast P_{qg}] \\ \frac{d}{dt} g(x, t) &= \frac{\alpha_s(Q)}{2\pi} \left[ \sum_i (q_i + \bar{q}_i) \circledast P_{gq} + g_i \circledast P_{gg} \right] \\ [q \circledast P] &= \int_x^1 d\epsilon \frac{q(\epsilon, t)}{\epsilon} \times P\left(\frac{x}{\epsilon}\right) \end{aligned} \quad (1.7)$$

where  $t \propto \text{Log}(Q^2)$ , and  $P_{q_1 q_2}$  represents the probability of finding a parton  $q_1$  in another parton  $q_2$ . In other words, the DGLAP evolution equations state that the PDF of a given parton  $q$  at an  $x$  value is determined from the contribution of all the partons at higher momentum fraction considering their probability of decaying into the parton  $q$ .

From the definition of the PDFs, one can also formulate a set of structure functions defined as:

$$F_2^p(x) = \sum_q e_q^2 f(x, Q^2) x \quad (1.8)$$

where  $e_q$  is the electric charge of a given quark flavour  $q$ . The structure functions were extensively measured in Deep-Inelastic Scattering (DIS) collisions at the Hadron-Elektron-Ringanlage (HERA) accelerator. The DIS process consists on the inelastic scattering of electrons off protons as presented in Fig. 1.5. In the DIS process, the momentum transferred from the electron to the proton is defined as  $Q^2 = -q^2 = -(k - k')^2$  and the corresponding Bjorken  $x$  fraction is  $x = Q^2/(2p \cdot q)$ .

The measurements of the  $F_2$  structure function performed by the ZEUS collaboration [28] at HERA are shown in Fig. 1.6. Even though DIS experiments were not able to probe the gluons directly, the DIS data showed that valence quarks did only carry half of the proton momentum been the other half carried by the gluons.

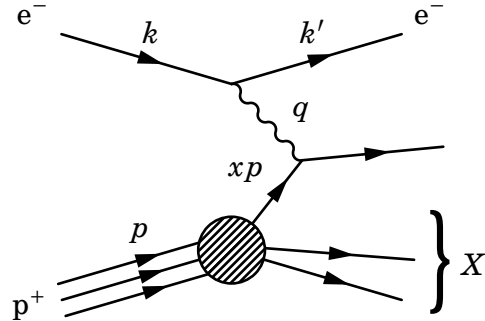


Figure 1.5: Feynman diagram of deep inelastic scattering of electrons against protons

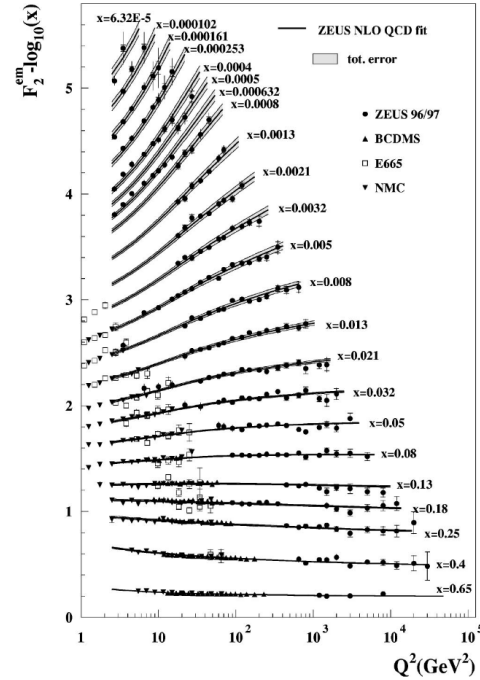


Figure 1.6: NLO QCD fits to the to the ZEUS  $F_2$  structure function data from 1996, 1997 and proton fixed-target at HERA. The error bands of the fit represent the total experimental uncertainty from both correlated and uncorrelated sources. Figure taken from Ref. [28]

Another important process used to constrain PDFs is the production of electroweak bosons such as W bosons or Drell-Yan (DY). In the DY process, a quark from one hadron and an anti-quark from another hadron annihilate into a virtual photon ( $\gamma^*$ ) or Z boson which then decays to a pair of leptons as shown in Fig. 1.7. The measurement of DY production can be used to constrain the quark PDFs in a wide range of momentum fraction  $x$  depending on the invariant mass of the dilepton pair. In addition, the measurement of the production of positive and negative charged W bosons in hadronic collisions is used to disentangle the flavour dependence of the quark PDFs. More details about the W boson production will be provided in Chapter 4.

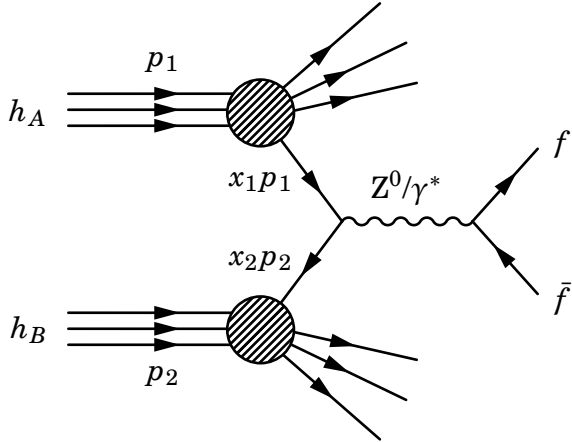


Figure 1.7: Feynman diagram of neutral charged Drell-Yan process

### 1.1.3 QCD phase diagram

The first attempt to describe the temperature dependence of matter at high energies was performed by Rolf Hagedorn in 1965 [29]. Hagedorn considered matter at high energies as a gas made of hadrons and employed a thermodynamical bootstrap approach to describe the hadron gas. After studying the mass spectrum of all the hadron species measured at the time, Hagedorn realized that the density of hadron species grows exponentially until it diverges at a temperature  $T_H \approx 158$  MeV, known as the Hagedorn temperature. Years later, with the advent of QCD, it was understood that the Hagedorn temperature described a transition from a hadron gas to a state of matter where quarks and gluons are asymptotically free called the Quark Gluon Plasma (QGP).

The description of the QCD phase transition turned out to be complicated because the critical temperature was close to the QCD scale  $\Lambda_{\text{QCD}} \approx 255 \text{ MeV}$  [30], where perturbative calculations are no longer reliable. An alternative method to study the non-perturbative regime of QCD consists of solving numerically the QCD field equations on a discrete space-time grid using a method called Lattice QCD. Nowadays, lattice QCD is able to describe the evolution of matter at finite temperatures and low densities. A sketch of the QCD phase diagram in terms of the temperature  $T$  and the baryon chemical potential  $\mu_B$ <sup>1</sup> is shown in Fig. 1.8.

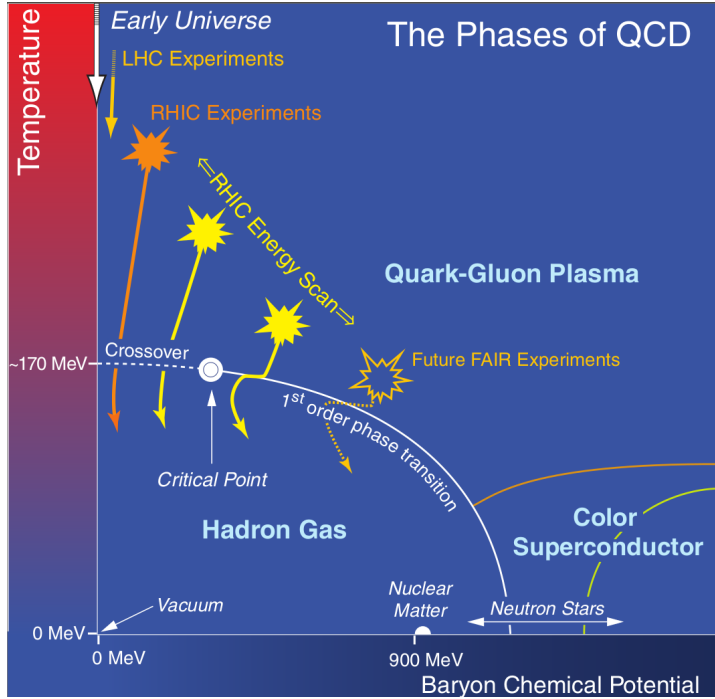


Figure 1.8: Schematic of the QCD phase diagram for nuclear matter. The solid lines show the phase boundaries and the solid circle represents the critical point. Figure taken from Ref. [31]

Normal matter exists in nature at low temperatures. At higher densities, matter undergoes a phase transition to a degenerate gas of fermions known as neutron gas, which is present in dense stellar objects such as white dwarfs or neutron stars. It is theorized that at even higher densities matter could reach a state of colour superconductivity where quarks bind together into Cooper pairs [32]. On the other hand, matter present at the beginning of the universe or produced in TeV-scale particle collisions has very

<sup>1</sup>The baryon chemical potential can be viewed as a measure of the excess of matter over anti-matter.

low baryon chemical potential. At  $\mu_B = 0$ , matter is described at low temperatures as a hadron gas and it becomes a QGP when the temperature exceeds the critical point. The phase transition between the hadron gas and the QGP has been established, using lattice QCD, to be a crossover where the two states coexist [33, 34].

## 1.2 Relativistic heavy-ion physics

Heavy-ion colliders have become essential tools to explore the fundamental properties of matter. Collisions of nuclei are used to probe the phase transitions of QCD and to recreate the QGP in the laboratory. The QGP is believed to have existed at the beginning of the Universe and to be part of the core of some astrophysical objects such as neutron stars. The study of the QGP allows to test QCD in the most extreme regimes and provides an insight on the evolution of the Universe. Some of the primary research goals of the heavy-ion physic programme is to understand the formation and properties of the QGP, and how does matter interact with the nuclear medium. Nowadays, the experimental study of ultra-relativistic (i.e. at energies above  $\sqrt{s_{NN}} > 10 \text{ GeV}$ ) heavy-ion collisions is performed at the Brookhaven National Laboratory (BNL) and at the European Organization for Nuclear Research (CERN).

### 1.2.1 History of heavy-ion accelerators

The interest in probing the QCD phase diagram in the laboratory arose in the 1970s after Werner Scheid, Hans Müller and Walter Greiner predicted that nuclear matter could be compressed in heavy-ion collisions at nucleus-nucleus energies larger than 100 MeV/nucleon [35]. The shock compression mechanism could reach matter densities up to five times higher than the density of atomic nuclei ( $\rho_0 = 0.16 \text{ baryons/fm}^3$ ) [35]. Coinciding in time, the Lawrence Berkely Laboratory (LBL) decided to transform their proton synchrotron accelerator Bevatron into a heavy-ion experiment called Bevalac. Heavy ions were produced in the Bevalac using the heavy-ion linear accelerator Super-HILAC and then sent to the Bevatron where the ions were further accelerated against a fixed target with energies of up to 2.6 GeV/nucleon [36]. The goal at the time was to investigate the equation of state (EoS) of hadronic matter at high densities. The understanding of the relation between the pressure and the energy density of dense matter was a key element needed to describe the dynamics of astrophysical objects such as supernovae and neutron starts [37, 38].

The successful creation of compressed nuclear matter at the Bevatron motivated the construction of several heavy-ion accelerators at higher energies. The first one was the Alternating Gradient Synchrotron (AGS) particle accelerator at the Brookhaven National Laboratory (BNL). The AGS became the first facility in 1960 to accelerate protons to an energy of 33 GeV, which allowed to discover the muon neutrino in 1962, to observe the CP violation of the weak interactions in Kaon decays in 1964, and to discover the  $J/\psi$  meson in 1974. An electrostatic accelerator called the Tandem Van de Graaf was built in 1970 to provide beams of ions to the AGS. The relativistic heavy-ion programme started at AGS in 1986 and lasted for 12 years during which several experiments were performed (e.g. E802, E858, E866, E896 and E917). AGS accelerated Si beams at 14.6 GeV/nucleon and Au beams at 11.1 GeV/nucleon, and collided them against different types of fixed targets (e.g. Al and Au).

In addition, CERN built the Super Proton Synchrotron (SPS) in 1976. To study the QGP, CERN added an Electron-Cyclotron Resonance (ERC) ion source in 1986 which initially accelerated ions of oxygen and sulphur at 200 GeV/nucleon. A subsequent upgrade of the ion injector in 1994 allowed to accelerate Pb ions up to an energy of 158 GeV/nucleon which were collided against fixed targets located in two experimental halls: one in the SPS north area (NA) and the other in the SPS west area (WA). Several fixed target experiments were built at the SPS between 1986 and 2005. After years of analyzing the Pb-Pb and Pb-Au fixed target collision data from SPS, CERN announced in 2000 that the combined results of the experiments NA44, NA45, NA49, NA50, NA52, WA97/NA57 and WA98, provided a first evidence of the creation of a new state of matter consistent with the QGP [39].

In the meantime, the first nucleus-nucleus collider known as the Relativistic Heavy Ion Collider (RHIC) started operations at the BNL in 2000. Two beams of Au are pre-accelerated at the AGS to an energy of 8.86 GeV/nucleon and then sent to RHIC where the Au beams are collided at  $\sqrt{s_{NN}} = 130\text{ GeV}$ . Other collision systems explored at RHIC include: p-p, p-Al, p-Au, d-Au, h-Au, Cu-Cu, Cu-Au and U-U. There are four detectors at RHIC called BRAHMS, PHENIX, STAR, and PHOBOS. Currently, only the STAR and PHENIX detectors are still active, while PHOBOS ceased operations in 2005 and BRAHMS in 2006. After four years of meticulously studying the system produced in Au-Au collisions with the four detectors, RHIC finally announced in 2005 the discovery of a strongly coupled QGP. Contrary to the expected gaseous behaviour, the QGP observed at RHIC turned out to resemble more a liquid with very little viscosity [40].

Currently, the largest heavy-ion collider is the Large Hadron Collider (LHC) at CERN

built in 2008. The SPS is used as injector to the LHC accelerating the Pb beams to energies of 1.38 TeV. The first nucleus-nucleus collisions at LHC took place in 2010 using Pb beams at 2.76 TeV. Since then, the LHC has collided different configurations involving ions, including p-Pb at 2.76 TeV (2013), Pb-Pb at 5.02 TeV (2015), p-Pb at 8.16 TeV (2016), Xe-Xe at 5.44 TeV (2017), and at the end of 2018 LHC is planning to provide a larger set of Pb-Pb collisions at 5.02 TeV. There are four detectors at the LHC called ALICE, CMS, ATLAS and LHCb. The four experiments are nowadays participating in the heavy-ion programme at LHC. Due to the large beam energies, the LHC is an ideal collider to study the QGP at very high temperatures, where one expects smaller QGP formation times and larger hot medium densities, compared to RHIC.

### 1.2.2 Geometry of nucleus-nucleus collisions

The number of particles produced in a nucleus-nucleus collision depends on the geometry of the collision. Since nuclei are extended objects made of nucleons (i.e. protons and neutrons), the number of nucleon-nucleon (NN) interactions increases the more head-on or central is the collision. The nucleons that participate in the collision are called participants while those that do not participate are called spectators. The overlap region of the collision is parameterized by the impact parameter  $\vec{b}$  which is the transverse distance between the centers of the two colliding nuclei as shown in Fig. 1.9.

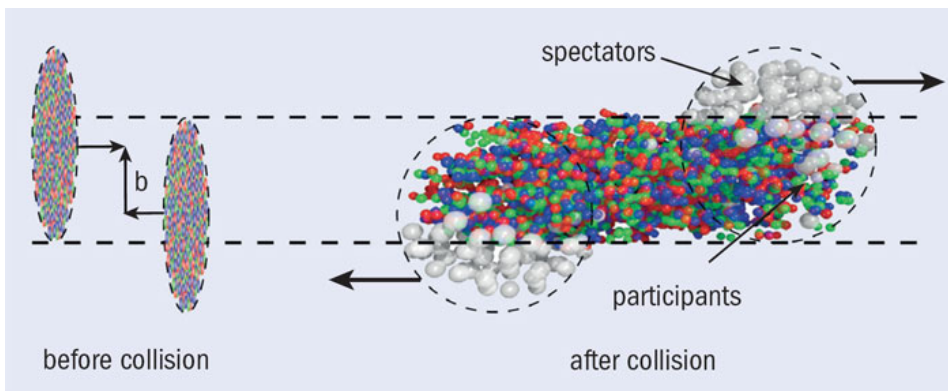


Figure 1.9: Illustration of two nucleus with impact parameter  $b$  before (left) and after (right) colliding. Figure taken from Ref. [31]

The formation of the QGP in nucleus-nucleus collisions depends on the number of colliding nucleons. To study the dynamics of the nuclear medium, the heavy-ion collisions are classified based on their centrality. The centrality  $c$  is defined as the fraction of the

total nucleus-nucleus inelastic cross section  $\sigma_{AB}^{inel}$  determined within the area defined by the impact parameter  $b$ , and it is expressed as  $c = \pi b^2 / \sigma_{AB}^{inel}$ .

The collision centrality can be related to the number of participants  $N_{part}$  and the number of binary NN collisions  $N_{coll}$  using a Glauber model. The Glauber model, developed in the 1950s by Roy Glauber, describes the collision between two nuclei as a superposition of NN interactions [41].

There are two ways of implementing the Glauber model, the optical and the Monte Carlo approach. In the optical approach, the physical observables are computed using the optical limit which assumes a continuous nucleon density distribution. On the other hand, in the Monte Carlo approach, the two nuclei are simulated by distributing the nucleons according to their nuclear density profile, and then the nucleus-nucleus collisions are modelled, at random impact parameters, by computing the individual NN collisions [41].

An example of a heavy-ion collision described by the optical Glauber model geometry is shown in Fig. 1.10. It represents the collision between a nucleus A with  $A$  nucleons and a nucleus B with  $B$  nucleons.

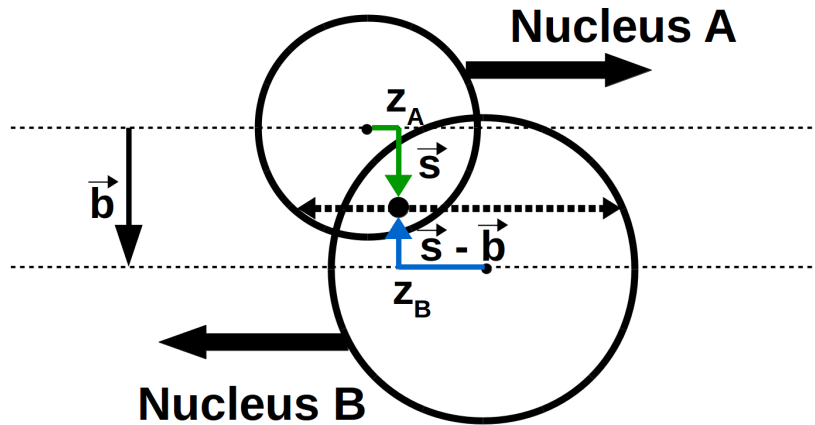


Figure 1.10: Schematic representation of the optical Glauber model geometry.

The tube located at a distance  $\vec{s}$  from the center of the nucleus A overlaps the tube located at a distance  $\vec{b} - \vec{s}$  from the center of the nucleus B. In this case, the nuclear overlap function  $T_{AB}(b)$  is defined as:

$$T_{AB}(b) = \int d^2 s T_A(\vec{s}) T_B(\vec{b} - \vec{s}) \quad (1.9)$$

where  $T_A$  and  $T_B$  are the nuclear thickness functions of the nucleus A and B, respectively.

The nuclear thickness function is given by  $T(\vec{r}) = \int \rho(\vec{r}, z) dz$ , where  $\rho$  is the nuclear density distribution of a given nucleus which is generally parameterized with a Wood-Saxon density profile:

$$\rho(r) = \rho_0 \frac{1 + w(r/r_0)}{1 + \exp\left(\frac{r-r_0}{a}\right)} \quad (1.10)$$

where  $r$  is the distance to the center of the nucleus,  $a$  represents the width of the edge region of the nucleus called the skin depth,  $w$  measures the deviation from a spherical shape, and  $\rho_0$  is a normalization factor such that the integral of the density is equal to the number of nucleons in the nucleus. Once the profile of the nucleus is parameterized, the average number of binary NN collisions  $\langle N_{coll} \rangle$  for a given impact parameter  $b$  is defined as:

$$\langle N_{coll}(b) \rangle = AB T_{AB}(b) \sigma_{nn}^{inel} \quad (1.11)$$

where  $\sigma_{nn}^{inel}$  is the inelastic NN cross section. Hence, the Glauber model provides a quantitative description of the geometry of the nuclear collision and can be used to estimate the variables ( $N_{part}$ ,  $N_{coll}$  and  $T_{AB}$ ) for a given centrality class.

Experimentally, the impact parameter of the collision can not be determined directly. However, the distribution of the number of soft particles scales with  $N_{part}$  while the number of particles with large momentum transfer scales with  $N_{coll}$ . As a result, one can estimate the centrality by fitting the distribution of charged particles produced in the collision using the functions of  $N_{part}$  and  $N_{coll}$  derived from the Glauber model. In addition, the collision centrality can be inferred from the number of spectators determined from the measurement of the transverse energy in the forward region.

### 1.2.3 Evolution of heavy-ion collisions

The evolution of a nucleus-nucleus collision undergoes several steps, starting from the collision of the nuclei to the final production of hadrons. Fig. 1.11 illustrates the different processes that occur during a heavy-ion collision associated to the production of the QGP.

1. Initial stage: At very high energies, the two nuclei are Lorentz contracted along the axis of motion while approaching each other at almost the speed of light. As a consequence, the nucleons of each nuclei are also contracted increasing the number of gluons until it reaches the gluon saturation scale. The dynamics of the nucleus can be described using the Glauber model or by an effective theory called the Color

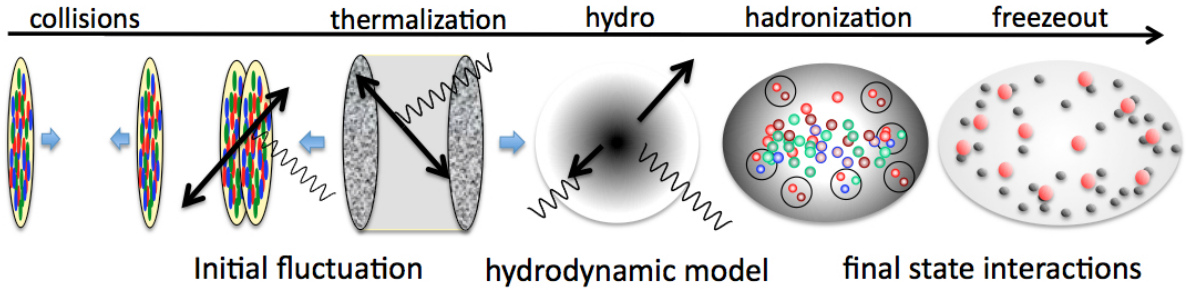


Figure 1.11: Schematic sketch of the evolution of a relativistic heavy ion collision. The wavy lines represent photons while the arrows correspond to jets. Figure taken from Ref. [31]

Glass Condensate (CGC). In addition, when the two nuclei collide, the partons inside the geometrical overlap region of the two nuclei undergo parton-parton interactions with large momentum transfers.

2. QGP formation and thermalization: The parton-parton interactions quickly start producing new particles increasing the density of the system until a phase transition is reached forming the QGP. After some time, the system reaches thermal equilibrium.
3. Hydrodynamical expansion: After reaching the thermal equilibrium, the system evolves as a perfect fluid. It first expands longitudinally along the beam direction and then it expands in all directions until the QGP reaches the critical temperature.
4. Hadronization: The medium undergoes a phase transition into a hadronic gas where the partons recombine into hadrons. In this phase, the system keeps expanding via hadron-hadron interactions until the average path length of the hadrons is as large as the size of the system.
5. Freeze-out: The hadron gas experience first a chemical freeze-out when the inelastic collisions between hadrons cease, fixing the composition of the particles. Subsequently, the system reaches the kinetic freeze-out when the elastic scattering

between the hadrons also stop, fixing the kinematic distributions of the particles. Subsequently, the particles escape the medium and are reconstructed in the detector.

### 1.2.4 Experimental probes of the QGP

The QGP can not be directly measured experimentally, since once it is created it only exists for a very short amount of time. Nonetheless, the QGP can be studied indirectly by measuring how the particles and the system produced in the collision is modified by the presence of the QGP. There are many experimental signatures that have been used to assess the different properties of the QGP, such as the enhancement of the strange quark production, suppression of the quarkonia yields, attenuation of the energy of jets, anisotropies in the azimuthal distribution of particles, among others. The production mechanism of each experimental probe depends on the momentum scale of the process. Signatures produced in processes involving large momentum transfer are called hard probes while those produced at low momentum scales are called soft probes.

The majority of the particles produced in heavy-ions collisions are soft and constitute the bulk of the system. Soft probes are used to study the thermal and hydrodynamical evolution of the medium. The production yields of soft particles scale with the number of nucleons that participate in the collision. The strange hadron yields and the elliptic flow are two examples of soft probes. On the other hand, hard probes are produced from the parton-parton hard scattering during the initial stage of the collision. Hard probes are ideal tools to study the structure of the system produced in the collision since they live through the full evolution of the medium, and their production cross section can be factorized into a partonic cross section described by pQCD and the nPDFs of the nuclei (see Eq. (1.6)). The number of hard particles produced in the medium scales with the number of binary NN collisions. Some important hard probes used to study the nuclear medium includes the electroweak bosons, quarkonium and jets. The following subsections present a brief description on some of the soft and hard probes of the QGP.

#### 1.2.4.1 Elliptic flow

When the QGP is formed, it undergoes a collective expansion due to the large pressure gradient produced by the multiple partonic interactions during the heavy-ion collision. This collective expansion is known as flow. The magnitude of the flow tends to grow with the number of parton-parton interactions and it depends on the initial conditions of the

collision. If the nucleus-nucleus collision is completely central ( $b = 0$ ) then the particles develop a radial flow, but if the collision is non-central ( $b \neq 0$ ) then the spacial anisotropy of the overlap region leads to an anisotropic flow as shown in Fig. 1.12.

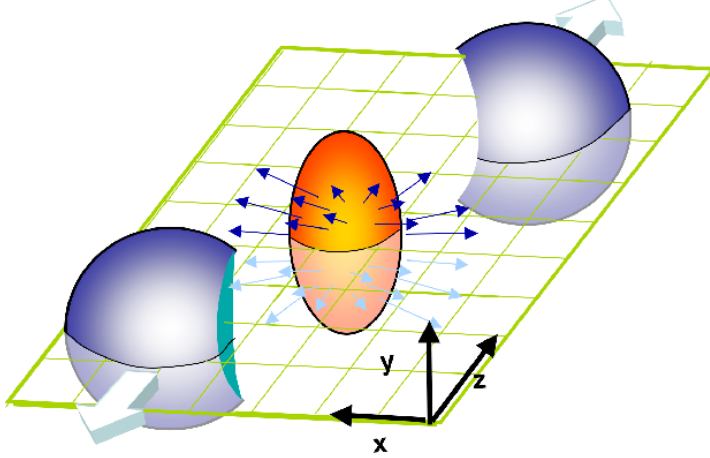


Figure 1.12: Sketch of the deformed medium and the elliptic flow produced in non-central heavy-ion collisions. Figure taken from Ref. [42]

Experimentally, the anisotropic flow can be determined from the Fourier decomposition of the particle azimuthal distribution with respect to the reaction plane  $\psi_{RP}$  [43]:

$$\frac{d^3N}{d^3\vec{p}} = \frac{1}{2\pi} \frac{d^2N}{dp_T dy} \left( 1 + 2 \sum_{n=1}^{\infty} v_n \cos[n(\phi - \psi_{RP})] \right) \quad (1.12)$$

where the Fourier coefficient  $v_2$  measures the strength of the elliptic flow and the reaction plane is derived from the direction of the beam ( $z$ -axis) and the impact parameter ( $x$ -axis) as presented in Fig. 1.12.

An alternative way to derive the flow coefficients is by computing the Fourier decomposition of the two-particle azimuthal distribution defined as [43]:

$$v_n \{2\}^2 = c_n \{2\} = \langle \cos[n(\phi_1 - \phi_2)] \rangle \quad (1.13)$$

where  $c_n \{2\}$  is called the two-particle cumulant and the brackets represent the average over all particles and events. The advantage of using particle correlations is that the Fourier coefficients do not depend on the reaction plane, but non-flow contributions (e.g. resonance decays) can affect the measurements. Higher orders of particle correlations, such as four-particle correlations, can reduce the impact of the non-flow effects.

The elliptic flow of the medium is sensitive to the equation of states of the QGP [43] and the bulk viscosity [44]. Furthermore, relativistic hydrodynamic calculations [45] predicts that the elliptic flow of hadrons can approximately be expressed as  $v_2 \propto (p_T - \beta m_T)$ , where  $\beta$  is the average flow velocity and  $m_T$  is the transverse mass of the hadron. As a consequence, the elliptic flow is expected to show a mass ordering where the more massive hadrons would have lower  $v_2$  values compared to the lighter hadrons.

The low  $p_T$ -dependence of the elliptic flow of strange hadrons measured at RHIC in Au-Au collisions at  $\sqrt{s_{NN}} = 200\text{ GeV}$  is presented in Fig. 1.13. The measurement of the elliptic flow of  $\pi^\pm$  mesons,  $K_s^0$  mesons, antiprotons and  $\Lambda$  baryons (with masses of 140, 495, 940 and 1,115 MeV, respectively), shows the expected mass ordering pattern as a function of the hadron  $p_T$ . Moreover, the good agreement between the RHIC results and the predictions using relativistic hydrodynamics assuming non-viscous flow supported the conclusion that the QGP behaves as an ideal fluid.

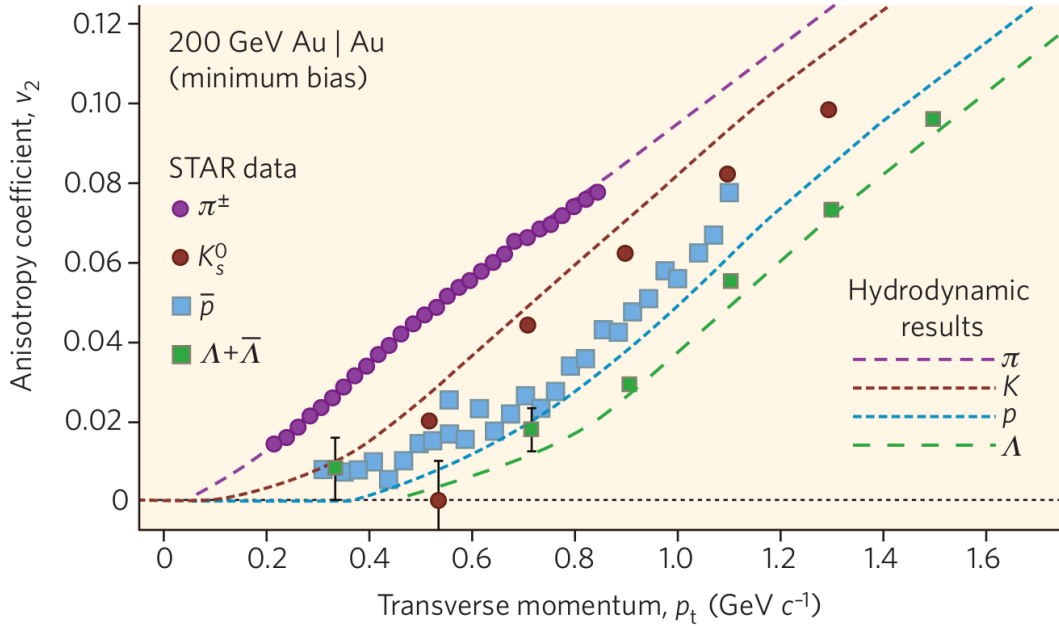


Figure 1.13: Elliptic flow distribution of as a function of transverse momemtum for  $\pi^\pm$  mesons,  $K_s^0$  mesons, antiprotons and  $\Lambda$  baryons measured by STAR collaboration in Au-Au collisions at  $\sqrt{s_{NN}} = 200\text{ GeV}$ . The results are compared with relativistic hydrodynamic calculations. Figure taken from Ref. [46]

### 1.2.4.2 Strangeness enhancement

Strange quarks belongs to the second generation of quarks and are roughly 20 (40) times more massive than the down (up) quarks. The number of strange quarks involved in a decay can be quantified through the quantum number called strangeness which can take values of +1, -1 and 0, for strange quarks, strange anti-quarks, and the other quarks, respectively. Strangeness is conserved in strong and electromagnetic interactions, while it is not conserved in weak decays. In hadronic collisions, strange quark-antiquark pairs ( $s\bar{s}$ ) are produced in parton-parton interactions via gluon fusion ( $gg \rightarrow s\bar{s}$ ) or quark annihilation ( $q\bar{q} \rightarrow s\bar{s}$ ), and through gluon splitting ( $g \rightarrow s\bar{s}$ ) during the evolution of the medium. The production of strange hadrons in proton-proton collisions is suppressed relative to hadrons made of light quarks (i.e. pions), due to the higher mass of the strange quark.

In heavy-ion collisions, where the QGP is formed, it was proposed by Johann Rafelski and Rolf Hagedorn [47] in 1980 that the enhancement of strangeness could serve as a signature of the QGP. Due to the large gluon density present in the hot medium, the gluon fusion becomes the dominant production mode of strange quark pairs in the QGP as shown in Fig. 1.14. When the temperature of the QGP decreases and the partons hadronize, the production of hadrons containing multi-strange (anti-)quarks is enhanced relative to the production of pions. Moreover, at high collision energies, the strange quarks can also bind to charm and bottom quarks during hadronization, producing many exotic hadrons (e.g. strange  $D_s$  or  $B_s$  mesons) that would otherwise be rarely seen without the presence of the QGP. As a consequence, one would expect an overall increase of strange quark pair production compared to pions, and also an enhancement of the production of multi-strange (anti-)hadrons in central heavy-ion collisions compared to proton-proton collisions [48]. The strangeness enhancement in the QGP can be described using a thermal model based on a grand canonical ensemble approach [49].

The enhancement of strange hadrons has been observed in SPS and RHIC [51]. Both experiments measured an increasing enhancement of the strangeness content of the hadrons. The ratios of the production yields at mid-rapidity of  $K^+/\pi^+$  and  $\Lambda/\pi^-$  mesons for central nuclues-nucleus collisions, shown in Fig. 1.15, reach a maximum relative strangeness enhancement at  $\sqrt{s_{NN}} \approx 8 \text{ GeV}$ , which has been interpreted as the energy during the transition to the QGP [51].

Recently, the ALICE collaboration published in [53] the observation of enhanced production of multi-strange hadrons in proton-proton collisions at  $\sqrt{s} = 7 \text{ TeV}$  with high charged-particle multiplicities. The results at LHC show that the enhancement of the

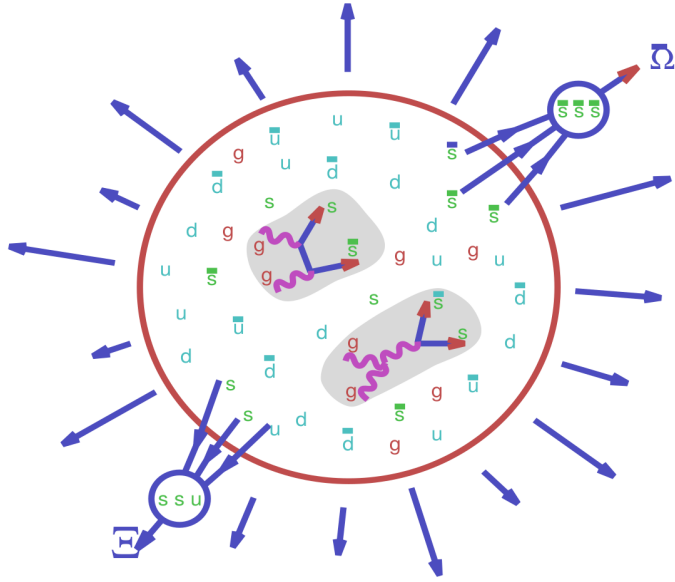


Figure 1.14: Sketch of the production of strange hadrons via gluon fusion in the QGP. Figure taken from Ref. [50]

strangeness production increases as a function of charged-particle multiplicity from high-multiplicity p-p to p-Pb to Pb-Pb collisions. Therefore, further studies of the mechanism of strangeness production at high multiplicities are necessary to understand the evolution of small systems.

#### 1.2.4.3 Jet quenching

Energetic partons are produced in the hard scattering at the beginning of the collision. The scattered partons fragment into other colour charged particles which then creates an ensemble of hadrons during the hadronization process. The baryons and mesons produced at the end of the collision tend to move along the same direction as the original fragmented parton, forming a localized spray of particles called jet. The jets can be reconstructed by clustering hadrons and other particles around a cone using a jet sequential recombination algorithm (e.g. anti- $k_t$  [54]).

In heavy-ion collisions, the hard partons lose energy when they traverse the hot medium either by multiple scattering with the medium constituents or by medium-induced gluon radiation, been the later the dominant mode of parton energy loss in the QGP. As a consequence, the energy of the jets is attenuated and the jets are considered quenched by the medium. The phenomenon of jet quenching in the QGP was first

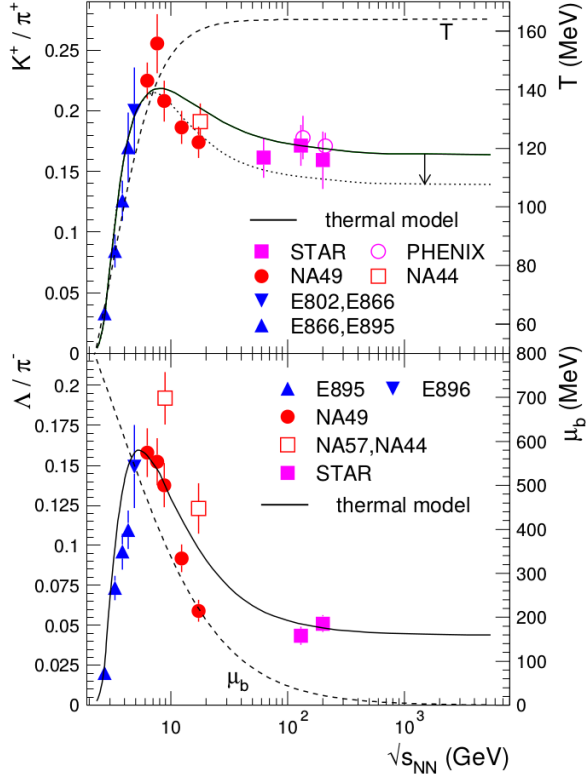


Figure 1.15: Energy distribution of the relative production ratios  $K^+/\pi^+$  and  $\Lambda/\pi^-$  at mid-rapidity measured at AGS (E802, E866, E895, E896) and SPS (NA44, NA49, NA57) in central Pb-Pb collisions, and at RHIC (STAR, PHENIX) in central Au-Au collisions. The solid line is the result of a statistical model calculation. The dotted line shows the  $K^+/\pi^+$  ratio including the additional effect of higher mass resonances. The dashed lines show the energy dependence of the temperature (upper panel) and baryonic density (lower panel). Figure taken from Ref. [52]

proposed in 1982 by James Bjorken. Bjorken suggested in [55] that the observation of events with two jets, where one of the jets escape the QGP without loosing energy while the other jet is fully quenched as shown in Fig. 1.16, could be used as a probe to determine the presence of the QGP.

The first direct observation of jet quenching was determined at the LHC after measuring an enhanced dijet asymmetry in Pb-Pb collisions compared to proton-proton collisions. The dijet asymmetry is quantified by measuring the jet energy imbalance between the two highest transverse energy jets with an azimuthal angle separation of  $\Delta\phi = |\phi_1 - \phi_2| > \pi/2$ . The jet energy imbalance  $A_J$  is derived as:

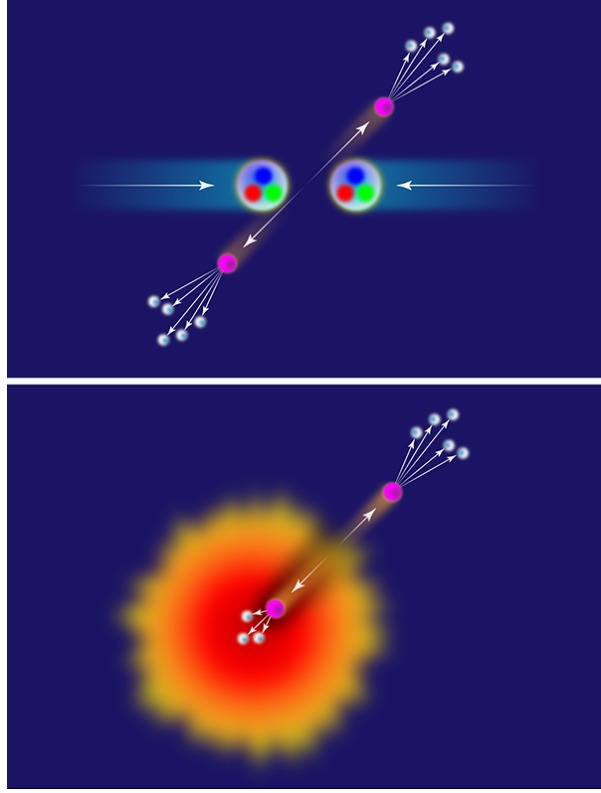


Figure 1.16: Sketch of the production mechanism of two jets in proton-proton (top) and heavy-ions (bottom) collisions. Figure taken from Ref. [56]

$$A_J = \frac{E_{T1} - E_{T2}}{E_{T1} + E_{T2}} \quad (1.14)$$

where  $E_{T1}$  is the transverse energy of the most energetic jet among the pair of jets. Fig. 1.17 presents the results, published by the ATLAS collaboration, of the dijet asymmetry distribution and the azimuthal angle between the two jets in different bins of centrality. The dijet asymmetry measured in Pb-Pb collisions at  $\sqrt{s_{\text{NN}}} = 2.76$  TeV are compared to the measurements from p-p collisions at  $\sqrt{s} = 7$  TeV and the simulated results derived using events from the Heavy Ion Jet INteraction Generator (HIJING) superimposed with PYTHIA events. The LHC results show a significant dijet energy imbalance in Pb-Pb collisions which increases with the centrality of the collision. This dijet asymmetry is not seen in p-p collisions evidencing the strong jet energy loss present in the QGP.

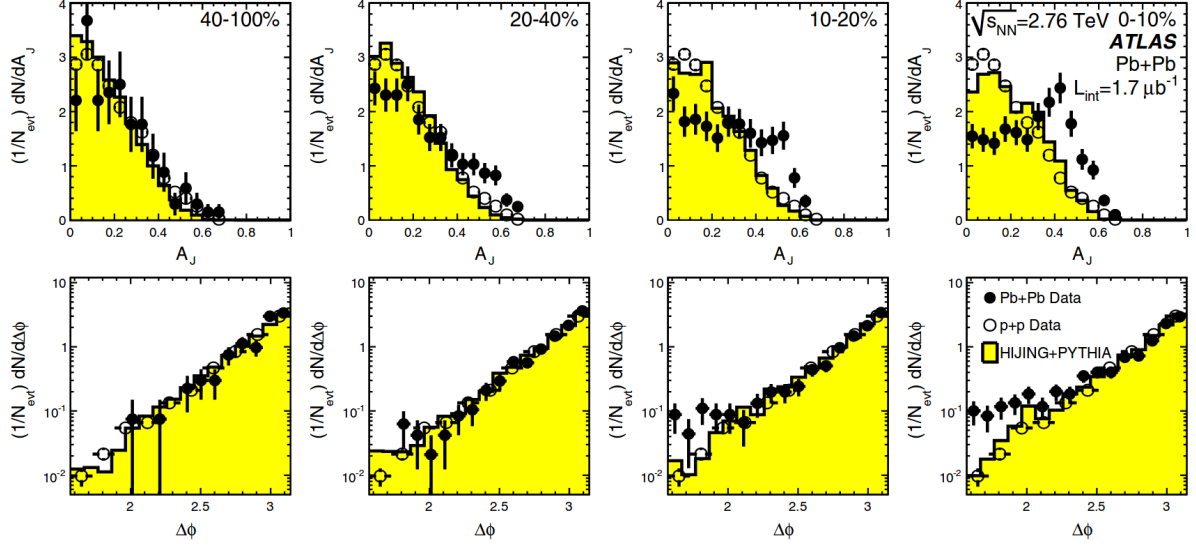


Figure 1.17: Dijet asymmetry measured by the ATLAS collaboration in lead-lead collisions at  $\sqrt{s_{NN}} = 2.76$  TeV (points) and proton-proton collisions at  $\sqrt{s} = 7$  TeV (open circles). The top panel shows the dijet asymmetry distributions and unquenched HIJING with superimposed PYTHIA dijets (solid yellow histograms), as a function of collision centrality. The bottom panel shows the distribution of the azimuthal angle between the two jets  $\Delta\phi$ , for data and HIJING+PYTHIA, also as a function of centrality. Figure taken from Ref. [57]

#### 1.2.4.4 Quarkonium production

Quarkonium ( $Q\bar{Q}$ ) is a meson composed of a heavy quark and its own anti-quark. Quarkonium can be classified as charmonium or bottomonium if it is made of charm quarks or bottom quarks, respectively. The ground state of charmonium is called  $J/\psi$  meson while the one for bottomonium is called  $\Upsilon(1S)$  meson. The properties of quarkonia are non-perturbative but since the mass of the heavy quarks is comparable to the mass of the quarkonia, the quarks move inside the quarkonia much slower than the speed of light. As a result, the properties of quarkonia can be computed using an effective non-relativistic model. For instance, one way to describe the binding of the quarks is by using a Cornell potential [58] given by:

$$V_{Q\bar{Q}}(r) = -\frac{a}{r} + br \quad (1.15)$$

where  $r$  is the binding radius of the quarkonium,  $a$  is the coulombic interaction coupling, and  $b$  is the string tension. The binding radius increases for higher excited

states of charmonium (e.g.  $\psi(2S)$ ) and bottomonium (e.g.  $\Upsilon(2S)$  and  $\Upsilon(3S)$ ) compared to their corresponding ground states (i.e.  $r_{\Upsilon(1S)} < r_{\Upsilon(2S)} < r_{\Upsilon(3S)}$ ).

One of the first signatures suggested to probe the QGP was the suppression of  $J/\psi$  meson production. In 1986, Tetsuo Matsui and Helmut Satz [59] proposed that the  $J/\psi$  meson binding potential gets screened in the QGP due to the interactions with the free colour charged constituents of the hot medium. The Debye colour screening potential increases with the temperature of the medium until the binding potential can no longer hold the quarks together, and the quarkonium "melts". The binding potential of quarkonium states gets weaker for larger binding radius. As a result, the higher excited states of quarkonium are expected to be more dissociated at a given temperature compared to the ground state, leading to a sequential suppression of quarkonia.

The sequential suppression of bottomonia states has been observed at the LHC. Fig. 1.18 shows the invariant mass distribution of dimuons measured by the CMS collaboration in Pb-Pb collisions at  $\sqrt{s_{NN}} = 5.02 \text{ TeV}$ . The result is compared to the invariant mass distribution obtained by adding the bottomonium mass peaks extracted from p-p collisions at  $\sqrt{s} = 5.02 \text{ TeV}$  on top of the Pb-Pb background and normalized to the  $\Upsilon(1S)$  mass peak in Pb-Pb. The comparison shows a clear suppression pattern where the  $\Upsilon(3S)$  is completely melted while part of the  $\Upsilon(2S)$  mass peak still survives.

The first evidence of  $J/\psi$  meson suppression was observed in Pb-Pb collisions at 158 GeV/nucleon by the NA50 collaboration at SPS [61]. The results at SPS showed that the  $J/\psi$  meson cross section measured in peripheral collisions was consistent with the expectations from nuclear absorption while in central collisions it was more suppressed [62]. However, the measurement of the  $J/\psi$  meson production in Au-Au collisions at  $\sqrt{s_{NN}} = 200 \text{ GeV}$  at RHIC showed a similar level of suppression compared to SPS, contrary to the higher expected suppression due to the higher beam energies.

To understand the measurements of  $J/\psi$  meson production at SPS and RHIC, it was proposed that the  $J/\psi$  meson production could also be enhanced at RHIC energies. According to [?], the  $J/\psi$  mesons could be regenerated in the most central collisions from the statistical hadronization of uncorrelated charm quark pairs produced in the hard scattering. The number of directly produced  $c\bar{c}$  pairs in central nucleus-nucleus collisions is expected to be small at SPS energies, but it can reach values of more than 10 and 100 charm quark pairs at RHIC and LHC energies, respectively [63]. The statistically regenerated  $J/\psi$  mesons are mainly produced at low  $p_T$  since the directly produced charm quarks reach thermal equilibrium before hadronizing [?].

In order to quantify how the hot nuclear medium modifies the production of quarkonia,

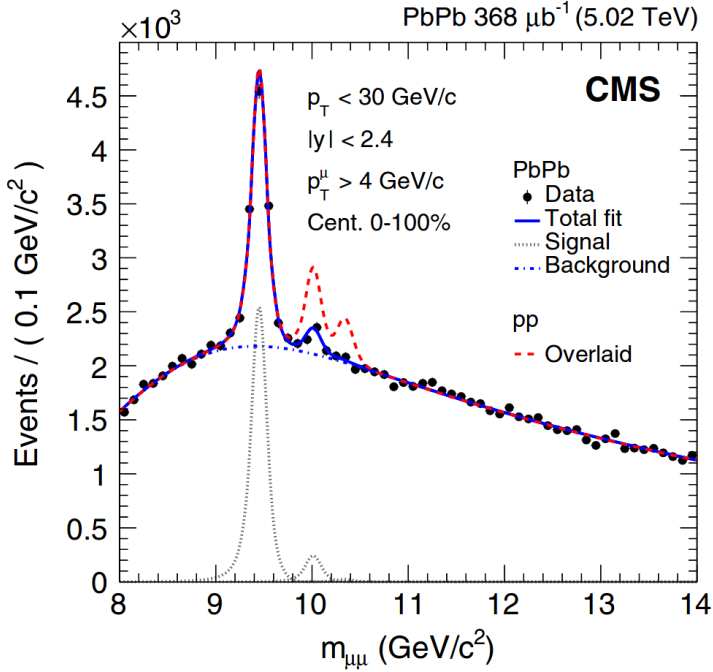


Figure 1.18: Dimuon invariant mass distribution measured by the CMS collaboration in Pb-Pb collisions at  $\sqrt{s_{\text{NN}}} = 5.02$  TeV. The total fit (solid blue line), the background component (dot-dashed blue line) and the individual  $\Upsilon(1S)$ ,  $\Upsilon(2S)$  and  $\Upsilon(3S)$  mass peaks (dotted gray lines) are shown. The dashed red line represents the p-p signal shapes added on top of the Pb-Pb background and normalized to the  $\Upsilon(1S)$  mass peak in Pb-Pb. Figure taken from Ref. [60]

one can measure the nuclear modification factor  $R_{AA}$  defined as:

$$R_{AA} = \frac{N^{AA}}{\langle N_{coll} \rangle N^{pp}} \quad (1.16)$$

where  $N^{AA}$  is the yield of particles measured in nucleus-nucleus collisions,  $N^{pp}$  is the same yield measured in proton-proton collisions, and  $\langle N_{coll} \rangle$  is the average number of binary nucleon-nucleon collisions. Proton-proton collisions are used as a reference since the average energy density of the medium is not enough to produce the QGP.

The measurements of the  $J/\psi$  meson production has also been performed at the LHC. The results of the  $J/\psi$  meson nuclear modification factor measured by the ALICE collaboration in the 0% – 20% most central Pb-Pb collisions at  $\sqrt{s_{\text{NN}}} = 2.76$  TeV are compared in Fig. 1.19 to the results measured by the PHENIX collaboration in the 0% – 20% most central Au-Au collisions at  $\sqrt{s_{\text{NN}}} = 200$  GeV. The  $J/\psi R_{AA}$  measured at the LHC is larger than the one measured at RHIC at low  $J/\psi$  meson  $p_T$ , consistent with

the trend predicted by the statistical regeneration model of charmonia.

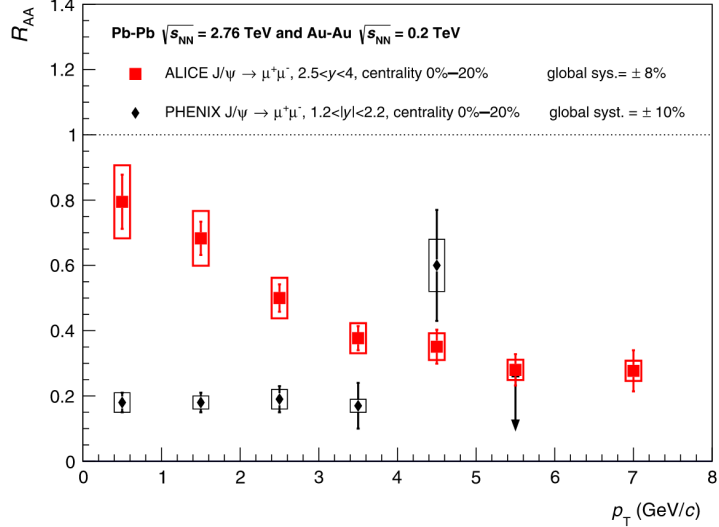


Figure 1.19: Nuclear modification factor of  $J/\psi$  meson as a function of transverse momentum measured by the ALICE collaboration in the 0% – 20% most central Pb-Pb collisions at  $\sqrt{s_{NN}} = 2.76$  TeV compared to results from the PHENIX collaboration measured in the 0% – 20% most central Au-Au collisions at  $\sqrt{s_{NN}} = 200$  GeV. Figure taken from Ref. [64]

#### 1.2.4.5 Electroweak boson production

Electroweak particles, such as W bosons and Z bosons, are produced in the parton-parton hard scattering and they do not interact strongly with the nuclear medium produced in the heavy-ion collisions. As a result, electroweak bosons are good probes of the initial stage of the proton-nucleus (p-A) and nucleus-nucleus (A-A) collisions. The dominant production mode of electroweak bosons in heavy-ion collisions is via the annihilation of a light quark and anti-quark. The large momentum scales involved in the production of weak bosons allows to derive precise calculations of their partonic cross sections using pQCD.

The production yields of electroweak bosons in proton-nucleus collisions are affected by the mix of protons and neutrons in the colliding nucleus (isospin effect), and the depletion (shadowing) or enhancement (antishadowing) of the PDFs in the nucleus. Thus, the measurement of the electroweak boson production in p-A can be used to set constraints to the global fits of the nuclear PDFs. In nucleus-nucleus collisions, the measurement of the nuclear modification factor of Z bosons at the LHC in Pb-Pb collisions

at  $\sqrt{s_{NN}} = 2.56$  TeV, presented in Fig. 1.20, shows that the production of weak bosons is not modified by the hot nuclear medium and only scales with  $N_{coll}$ , which could be used as an indirect way to determine the centrality of the collision.

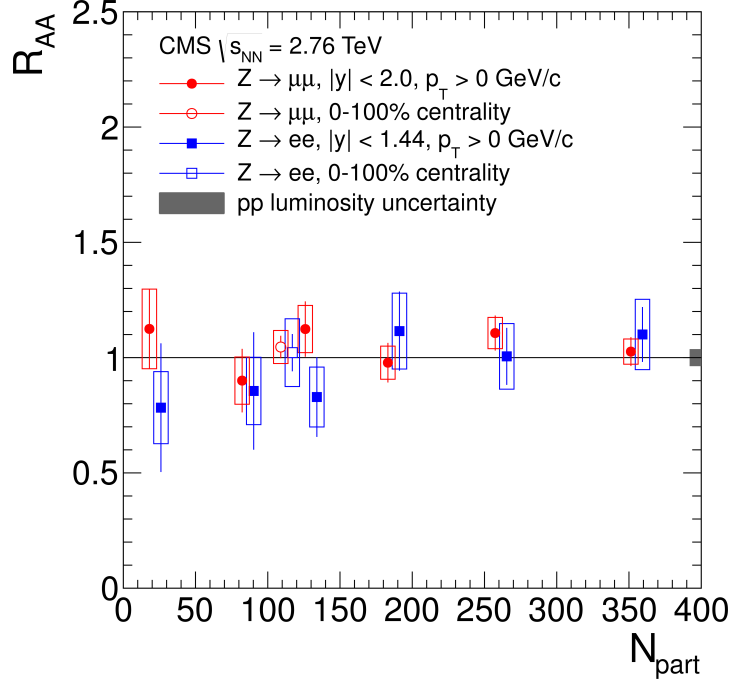


Figure 1.20: Nuclear modification factor  $R_{AA}$  of  $Z \rightarrow e^+e^-$  (blue squares) and  $Z \rightarrow \mu^+\mu^-$  (red circles) events as a function of the number of participants measured by the CMS collaboration in Pb-Pb collisions at  $\sqrt{s_{NN}} = 2.56$  TeV. The open points represent the centrality-integrated  $R_{AA}$  and the vertical lines (boxes) correspond to statistical (systematic) uncertainties. The grey bar at  $R_{AA} = 1$  represents the uncertainty of the luminosity determined in proton-proton collisions. Figure taken from Ref. [65]

## EXPERIMENTAL SETUP

This chapter provides a brief overview of the experimental setup employed to acquire the data used in this thesis. The data is derived from high energy collisions of protons and lead ions recorded by the CMS detector. The Large Hadron Collider and the settings of the particle collisions are described in Section 2.1. Moreover, the main features of the CMS detector and its components are detailed in Section 2.2.

### 2.1 The Large Hadron Collider

The Large Hadron Collider is currently the largest and highest-energy particle accelerator in the world. It is installed in an underground tunnel of 26.7 km in circumference, located 175 m beneath the border between France and Switzerland. The construction of the LHC was handled by CERN and took 10 years to complete. The LHC is designed to accelerate and collide beams of protons or heavy ions (e.g Pb nuclei). Before being injected into the LHC, particles are accelerated through a chain of accelerators housed at CERN. Each accelerator boosts the energy of the particles and transfers them to the next machine. There are two main injection chains for the LHC, one optimised for protons and the other for Pb nuclei ( $Pb^{82+}$ ). Fig. 2.1 shows a schematic diagram of the LHC injection chains for protons and Pb ions represented with red and blue arrows, respectively.

Protons are extracted from a gas of hydrogen atoms by stripping off their electrons in a Duoplasmatron, and are initially accelerated to an energy of 50 MeV with radiofrequency (RF) cavities in the linear accelerator Linac-2. Afterwards, they are sent to the Proton

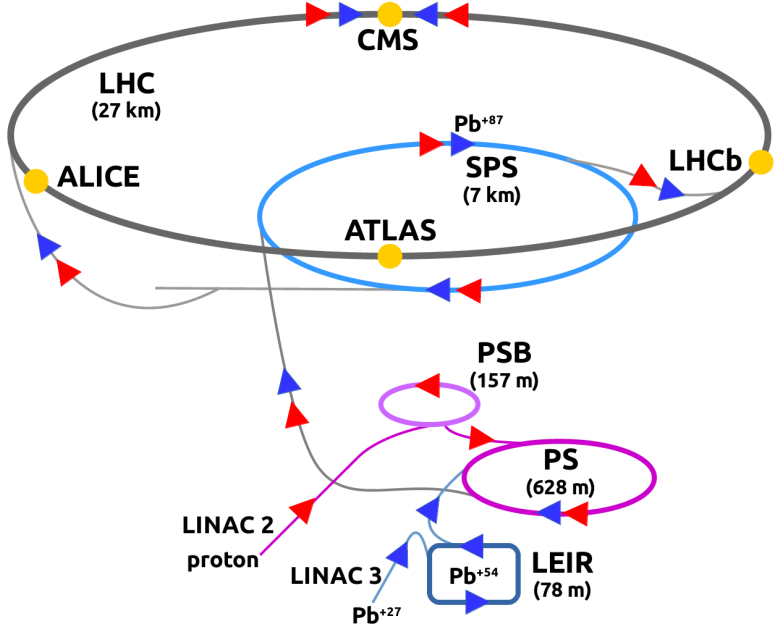


Figure 2.1: Schematic diagram of the LHC injection chain for protons and Pb nuclei. The proton and Pb ion trajectories are indicated with red and blue arrows, accordingly. The location of each LHC detector is also included.

Synchrotron Booster (PSB), which is composed of four superimposed synchrotron rings that groups the protons into bunches and accelerates them to 1.4 GeV. Six proton bunches from the PSB are sequentially fed into the Proton Synchrotron (PS), where they are accelerated to 25 GeV and further splitted into 72 bunches separated in time by 25 ns. The proton beam is further accelerated to 450 GeV in the Super Proton Synchrotron (SPS) and alternately injected in the two LHC beam pipes, one beam pipe in the clockwise direction and the other in the counter-clockwise direction. Conventional electromagnets are used to keep the particles circulating in the PSB, PS and SPS accelerators.

The heavy-ion accelerator chain was initially designed in the 1990s for the SPS fixed-target experiments and then upgraded in the 2000s for the LHC. The Electron Cyclotron Resonance Ion Source (ECRIS) is used to produce heavy ions. In the case of lead, a beam of  $Pb^{27+}$  ions with an energy of 2.5 keV/nucleon is extracted from the ECRIS every 200  $\mu$ s, and then accelerated to 250 keV/nucleon with a 100 MHz RF quadrupole (RFQ). The ion beam is sent afterwards to the linear accelerator Linac-3, which accelerates the Pb ions to 4.2 MeV/nucleon and transfers them to the Low Energy Ion Ring (LEIR). The  $Pb^{27+}$  ions are passed through a 0.3  $\mu$ m-thick carbon foil in the Linac-3–LEIR transfer line,

stripping them to  $\text{Pb}^{54+}$  ions. The LEIR accelerates the  $\text{Pb}^{54+}$  ions to 72 MeV/nucleon and packs them in bunches using electron cooling. Every 3.6 s, the LEIR feeds two bunches into the PS ring and up to 16 bunches are accumulated, forming a batch, before being transferred to the SPS. The PS batch is compressed to a time interval of 100 ns, and accelerated to 5.9 GeV/nucleon. When the  $\text{Pb}^{54+}$  ions are sent to the SPS, they are fully stripped ( $\text{Pb}^{82+}$  ions) through an aluminium foil. The SPS accelerates up to twelve  $\text{Pb}^{82+}$  ion batches from the PS to 176.4 GeV/nucleon and then injects them into the LHC.

The LHC consists of eight straight sections called insertion regions (IR), connected by eight arc sections as shown in Fig. 2.2. The size and trajectory of the particle beams are controlled, in each arc section of the LHC, with a series of superconducting magnets made of Niobium-Titanium and kept at a temperature of 1.9 K with superfluid Helium-4. Dipole magnets are used to bend the particles, while quadrupole magnets focus the beam. Moreover, each particle beam is accelerated in IR4 with eight RF superconducting cavities operated at 400 MHz. The LHC beam dumping system, employed to safely stop the particle beams, is located at IR6. In addition, to protect the LHC from beam losses and absorb the beam halo, a collimation system is installed at IR3 and IR7, dedicated for beam momentum and betatron cleaning, respectively. The other four insertion regions house each of the four main LHC detectors, where the beams are collided in their corresponding interaction point (IP). The four main experiments at LHC are:

- A Large Ion Collider Experiment (ALICE) [67]: Is a particle detector located at IP2, specialized on the measurement of the properties of nuclear matter at high densities. The main interest of the ALICE collaboration is the study of the QGP and the different aspects of heavy-ion physics. The ALICE detector is divided in three sets of subdetectors: the global event detectors are used to characterise the geometry of the collisions, the central barrel detectors can track charged particles down to low momentum and identify hadrons and electrons, and the muon spectrometer can reconstruct muons in the forward region.
- A Toroidal LHC ApparatuS (ATLAS) [68]: Is a general-purpose particle detector located at IP1, optimised for particle collisions at the highest rates and energies achieved in the LHC. It consists of a toroidal magnetic system, an inner tracker, an electromagnetic and hadronic calorimeter, and a muon spectrometer. It is able to measure the energy of electromagnetic particles and hadrons, determine the momentum of charged particles, reconstruct jets, and identify muons with high precision. The ATLAS collaboration is involved in different physical areas including

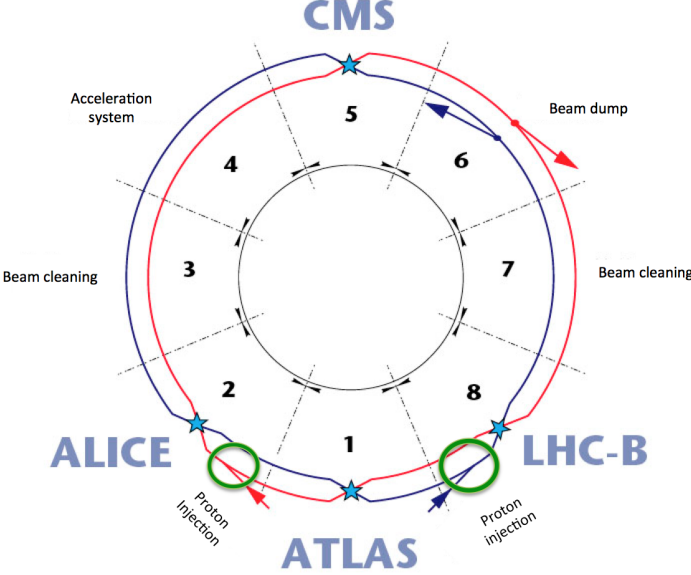


Figure 2.2: Schematic diagram of the LHC layout. Figure taken from Ref. [66].

the study of the Higgs boson, searches for physics beyond the SM, precision measurements of electroweak and top quark properties, and heavy-ion physics. The ATLAS detector is fully hermetic and covers the mid-rapidity range.

- Compact Muon Solenoid (CMS) [69]: Is a multi-purpose particle detector located at IP5. Its has a similar design as the ATLAS detector covering the same physics areas. The CMS detector and its inner components are detailed in Section 2.2.
- LHCb [70]: Is a single-arm forward spectrometer located at IP8, designed to precisely measure the decays of hadrons containing bottom quarks. It is able to distinguish between the interaction point and the B hadron decay vertex, perform particle identification, measure the energy of electrons, photons and hadrons, and reconstruct the trajectories of charged particles. The research programme of the LHCb experiment nowadays covers heavy-flavour, QCD, electroweak and heavy-ion physics. LHCb can also operate in fixed-target mode by injecting a small amount of a noble gas (e.g. helium) around its collision region inside the beam pipe.

The LHC started operations in 2008, and delivered collision data during its first running period (labelled as Run-1) until 2013, followed by a long shut-down (LS1) period

of 2 years dedicated to upgrade the machine. The second period of LHC operations (Run-2) started on 2015 and will conclude at the end of 2018. During Run-1, the LHC performed proton-proton (p-p) collisions at a center-of-mass energy of  $\sqrt{s} = 2.36 \text{ TeV}$  in 2009, and p-p collisions at  $\sqrt{s} = 7 \text{ TeV}$  and lead-lead (Pb-Pb) collisions at a NN center-of-mass energy of  $\sqrt{s_{\text{NN}}} = 2.56 \text{ TeV}$  between 2010 and 2011. In addition, the LHC collided protons at  $\sqrt{s} = 8 \text{ TeV}$  in 2012, and proton-lead (p-Pb) at  $\sqrt{s_{\text{NN}}} = 5.02 \text{ TeV}$  in 2013. Afterwards, the Run-2 period started with p-p collisions at  $\sqrt{s} = 13 \text{ TeV}$  and Pb-Pb collisions at  $\sqrt{s} = 5.02 \text{ TeV}$  in 2015, p-Pb collisions at  $\sqrt{s} = 8.16 \text{ TeV}$  in 2016, p-p collisions at  $\sqrt{s_{\text{NN}}} = 5.02 \text{ TeV}$  in 2017, Xenon-Xenon (Xe-Xe) collisions at  $\sqrt{s_{\text{NN}}} = 5.16 \text{ TeV}$ , and will finish with Pb-Pb collisions at  $\sqrt{s_{\text{NN}}} = 5.02 \text{ TeV}$  at the end of 2018.

The performance of the LHC can be characterised based on its delivered luminosity. The higher the luminosity of the collider, the more particle interactions occur when the beams are collided. The number of interactions per unit time  $dN/dt$  produced in a given reaction is proportional to the cross section  $\sigma_r$  of the corresponding process, as defined in:

$$\frac{dN}{dt} = L\sigma_r \quad (2.1)$$

where  $L$  represents the instantaneous luminosity of the particle collisions. In the case of circular beam profiles, the instantaneous luminosity can be derived via:

$$L = \frac{k_b N_{b,1} N_{b,2} f_{rev} \gamma}{4\pi \epsilon_n \beta^*} F \quad (2.2)$$

where  $k_b$  is the number of bunches collided,  $N_{b,1}$  and  $N_{b,2}$  are the number of particles per bunch in the two beams,  $f_{rev} = 11245 \text{ Hz}$  is the revolution frequency at the LHC,  $\epsilon_n$  is the normalized transverse beam emittance,  $\beta^*$  is the beta-function defined at the interaction point, and  $F$  is a geometric reduction factor due to the angle at which the two beams collide. The integrated luminosity is derived by integrating the instantaneous luminosity over a given period of time.

### 2.1.1 LHC heavy-ion schemes in 2015-2016

The LHC heavy-ion physics programme took place in 2015 [71] during four weeks between November and December. The first week was dedicated to p-p collisions at  $\sqrt{s} = 5.02 \text{ TeV}$  to create a reference sample for the Pb-Pb collision data. Each proton beam was accelerated to  $2.51 \text{ TeV}$ . The number of proton bunches were initially 44 and was sequentially increased during the week to a maximum of 1825 bunches. The

subsequent week, the LHC beam settings were modified to collide two beams of  $\text{Pb}^{82+}$  ions at  $\sqrt{s_{\text{NN}}} = 5.02 \text{ TeV}$ . The LHC started accelerating ten Pb bunches to 2.51 TeV/nucleon, and then progressively increased the number of Pb bunches until it reached 518 at the end of the Pb-Pb data taking. The Pb beam lifetime was shorter than for protons due to the large ultraperipheral electromagnetic interactions between Pb ions, requiring to refill the beams more often. All experiments took Pb-Pb collision data, including LHCb for the first time. The integrated luminosity of the Pb-Pb collision data is shown in the left plot of Fig. 2.3.

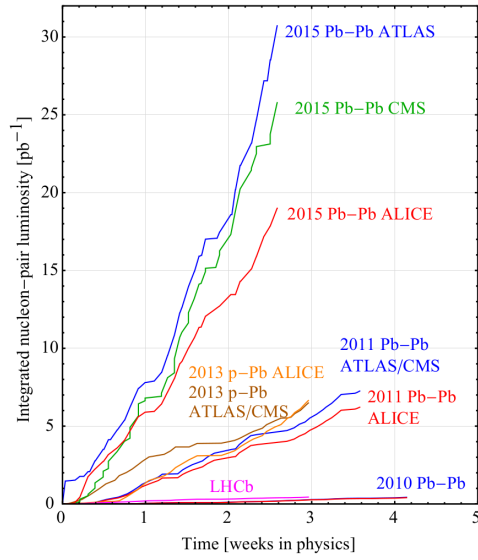


Figure 2.3: Integrated nucleon-pair luminosity delivered by the LHC to each experiment during Pb-Pb collisions at  $\sqrt{s_{\text{NN}}} = 5.02 \text{ TeV}$ . The integrated luminosity of p-Pb collisions at  $\sqrt{s_{\text{NN}}} = 5.02 \text{ TeV}$  and Pb-Pb collisions at  $\sqrt{s_{\text{NN}}} = 2.76 \text{ TeV}$  are included for comparison. Figure taken from Ref. [71]

The following year, asymmetric collisions of  $\text{Pb}^{82+}$  nuclei with protons were performed between November 7th and December 4th. Several beam configurations were implemented in 2016 to fulfill the interests of each experiment: ALICE requested p-Pb data at  $\sqrt{s_{\text{NN}}} = 5.02 \text{ TeV}$ , CMS and ATLAS asked for p-Pb data at  $\sqrt{s_{\text{NN}}} = 8.16 \text{ TeV}$  with an integrated luminosity of at least  $L = 100 \text{ nb}^{-1}$ , and LHCb requested p-Pb collisions at  $\sqrt{s_{\text{NN}}} = 8.16 \text{ TeV}$  complemented with a reversal of the beam direction. After careful planning, the first ten days were dedicated to p-Pb collisions at  $\sqrt{s_{\text{NN}}} = 5.02 \text{ TeV}$  optimised for ALICE. Afterwards, the LHC spent two weeks on p-Pb collisions at  $\sqrt{s_{\text{NN}}} = 8.16 \text{ TeV}$ . At the beginning of the p-Pb collisions at  $\sqrt{s_{\text{NN}}} = 8.16 \text{ TeV}$ , the proton beam was composed of 702 bunches at 6.5 TeV moving in the clockwise direction, while the Pb beam

was made of 548 bunches at 2.56 TeV/nucleon moving in the anti-clockwise direction, around the LHC rings. The LHC then proceeded to reverse the beam directions after the integrated luminosity accumulated in CMS and ATLAS reached half of the requested value ( $\sim 60 \text{ nb}^{-1}$ ), and kept colliding 540 Pb bunches with 684 proton bunches during the last nine days. At the end of the heavy-ion data taking period, the LHC managed to deliver a total integrated luminosity of  $L = 188 \text{ nb}^{-1}$  of p-Pb data to the CMS experiment as shown in Fig. 2.4. The beam settings used by LHC during the heavy-ion collision programme performed in 2015 and 2016 are summarized in Table 2.1.

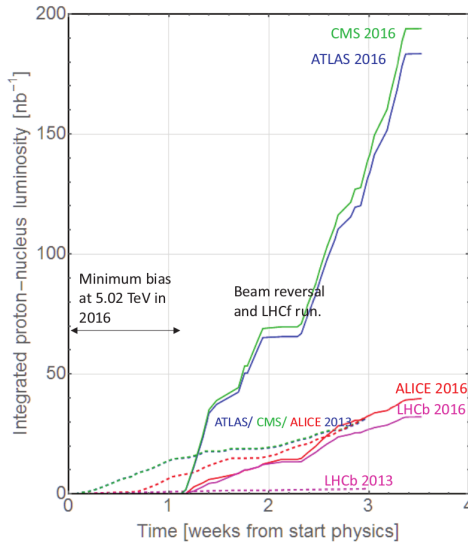


Figure 2.4: Integrated proton-nucleus luminosity delivered by the LHC to each experiment during p-Pb collisions at  $\sqrt{s_{\text{NN}}} = 8.16 \text{ TeV}$  (solid lines). The integrated luminosity of p-Pb collisions at  $\sqrt{s_{\text{NN}}} = 5.02 \text{ TeV}$  (dashed lines) is included for comparison. Figure taken from Ref. [72]

## 2.2 The Compact Muon Solenoid

The CMS [69] is a multi-purpose particle detector housed in an underground cavern at IP5 of the LHC. The CMS experiment is integrated, at the time of writing this thesis, by an international collaboration of over 5600 members from around 215 institutes from 46 countries. The CMS is composed of a central barrel in the mid-rapidity region closed by two endcap disks, one on each side of the IP, forming a hermetic cylindrical detector. The CMS detector consists of four different subdetector systems: the silicon tracker, the Electromagnetic CALorimeter (ECAL), the Hadronic CALorimeter (HCAL) and the muon

Variable	p-p 2015	Pb-Pb 2015	p-Pb 2016
Fill no.	4647	4720	5562
Collision energy $\sqrt{s_{\text{NN}}}$ [TeV]	5.02	5.02	8.16
Pb beam energy $E_{\text{Pb}}$ [TeV/nucleon]	-	2.51	2.56
Beam energy $E_p$ [TeV/proton]	2.56	6.37	6.5
Pb ions per bunch $N_b^{\text{Pb}}$ [ $10^8$ ]	-	2.0	2.1
Protons per bunch $N_b^p$ [ $10^{10}$ ]	10.1	-	2.7
No. of Pb bunches $k_b^{\text{Pb}}$	-	518	540
No. of proton bunches $k_b^p$	1825	-	684
No. of colliding bunches $k_c$	1813	491	513
$\beta^*$ [m]	4	0.8	0.6
Crossing angle [ $\mu\text{rad}$ ]	170	145	140
Pb beam emittance $\epsilon_n^{\text{Pb}}(x, y)$ [ $\mu\text{m}$ ]	-	2.1	1.6
Pb bunch length $\sigma_z^{\text{Pb}}$ [m]	-	0.09	0.9
CMS peak lumi. $L^{\text{peak}}$ [ $10^{27}\text{cm}^{-2}\text{s}^{-1}$ ]	$3.4 \times 10^5$	3	869
CMS integrated lumi. $L_{\text{int}}$ [ $\text{nb}^{-1}$ ]	28820	0.6	188

Table 2.1: LHC beam parameters during the highest luminosity physics fills. The luminosity values are averages for CMS. Information extracted from Ref. [73]

chambers. A superconducting solenoid magnet placed in the barrel section generates a magnetic field of 3.8 T. The tracking system, the ECAL and the HCAL, are located within the solenoid volume, while the muon system is placed between the layers of the flux-return yoke which confines the magnetic flux. A sectional view of the CMS detector in its 2016 configuration is shown in Fig. 2.5.

One of the main components of the CMS detector is its superconducting solenoid magnet of 6 m internal diameter and 12.5 m length. The magnet produce an uniform magnetic field of 3.8 T in the central region by supplying an electric current of 18.1 kA through a four-layer winding coil made of NbTi wire. To be able to sustain the large electric currents, the solenoid coil is thermally insulated within a vacuum volume and operated in superconducting mode at a temperature of 4.6 K with a thermal-siphon cooling system fed with liquid helium. The flux of the magnetic field outside the barrel is returned through a massive steel yoke of 10000 t divided in five barrel wheels and four endcap disks at each end. In case there is a major system fault or the magnet suffers a superconducting-to-resistive transition (quench), the electric power source is immediately disconnected and the stored magnetic energy is quickly discharged through a 30 mΩ dump resistor placed outdoors.

The coordinate system of the CMS detector is centred at the interaction point. It is

## 2.2. THE COMPACT MUON SOLENOID

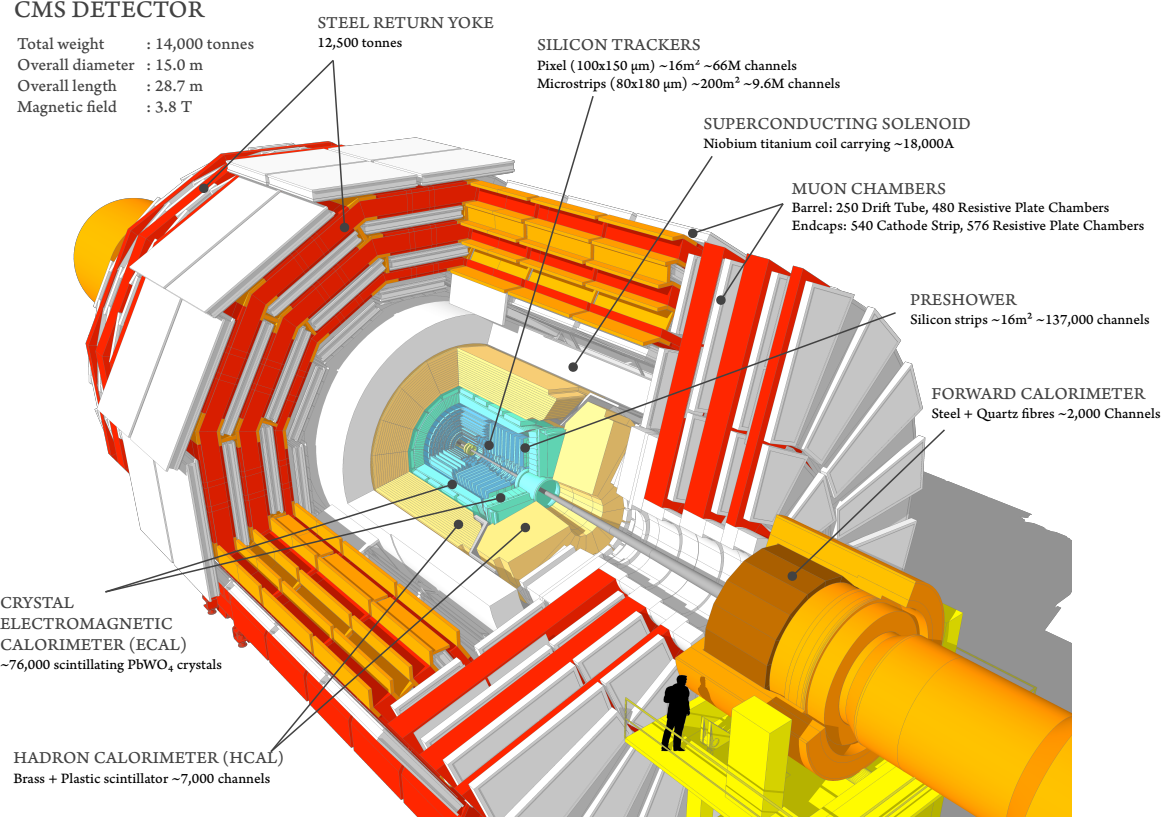


Figure 2.5: Cutaway view of the CMS detector in its configuration used during 2015 and 2016. The labels and basic details of each sub-detector are included. [74]

oriented in such a way that the x-axis points radially inward to the centre of the LHC ring while the y-axis points upward perpendicular to the LHC plane. The z-axis is defined parallel to the beam. By convention, the positive z-direction is defined in symmetric particle collisions (e.g. p-p or Pb-Pb) along the counter-clockwise beam direction, while for proton-nucleus collisions it is defined along the proton-going direction. Moreover, the trajectory of particles measured at CMS are described in spherical coordinates as displayed in Fig. 2.6. The polar angle  $\theta$  is measured from the z-axis in the y-z plane while the azimuthal angle  $\phi$  is measured from the x-axis in the x-y plane called the transverse plane. The radial coordinate  $r$  is also measured in the transverse plane. The polar angle is replaced by the pseudorapidity  $\eta$  which, for massless particles, is Lorentz invariant under longitudinal boost. The pseudorapidity is zero in the transverse plane and approaches infinity towards the z-axis according to:

$$\eta = -\ln \left[ \tan \left( \frac{\theta}{2} \right) \right] \quad (2.3)$$

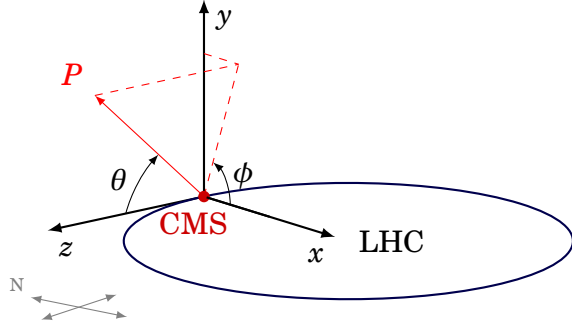


Figure 2.6: Schematic of the coordinate system used in the CMS experiment.

The details of the original configuration of the CMS detector can be found in Ref. [69]. After Run-1 was over, the CMS underwent several improvements as part of the planned upgrades for the LS1 shut-down period (2013-2014). The systems upgraded during LS1 include the muon endcap stations, the hadron calorimeter, and the L1 trigger. In the case of the muon system, an additional disk of CSC and RPC chambers was installed on the outermost part of each endcap section providing a fourth measurement in the forward region [75]. Moreover, the photosensors of the forward (outer-barrel) hadron calorimeter were replaced with multi-anode photomultiplier tubes (silicon photomultipliers), and the corresponding readout electronics were upgraded to handle the new sensors [76]. And finally, the framework and electronics of the L1 trigger system were completely changed to sustain the increasing interaction rate of the LHC beam collisions [77].

### 2.2.1 Subdetectors

The CMS detector [69] is composed of several subdetectors which provide a precise measurement of the trajectory and energy of the particles emitted from the LHC collisions. The superconducting solenoid volume contains the inner tracker close to the beam line followed radially outwards by the ECAL and the HCAL. The muon chambers are installed outside of the solenoid, interspersed with layers of the flux-return yoke. An electromagnetic preshower is installed in the endcaps complementing the ECAL and improving the identification of photons and electrons.

### 2.2.1.1 Tracker

The CMS tracking system is designed to measure the trajectory of charged particles and reconstruct the 3D vertex position of the primary interaction and the secondary decays. It is completely surrounded by the volume of the solenoid magnet in the barrel region, and has a diameter of 2.5 m and a length of 5.8 m, covering the interaction point. The CMS tracker is made of a pixel detector and a silicon strip tracker. A schematic cross section of the CMS inner tracker is presented in Fig. 2.7.

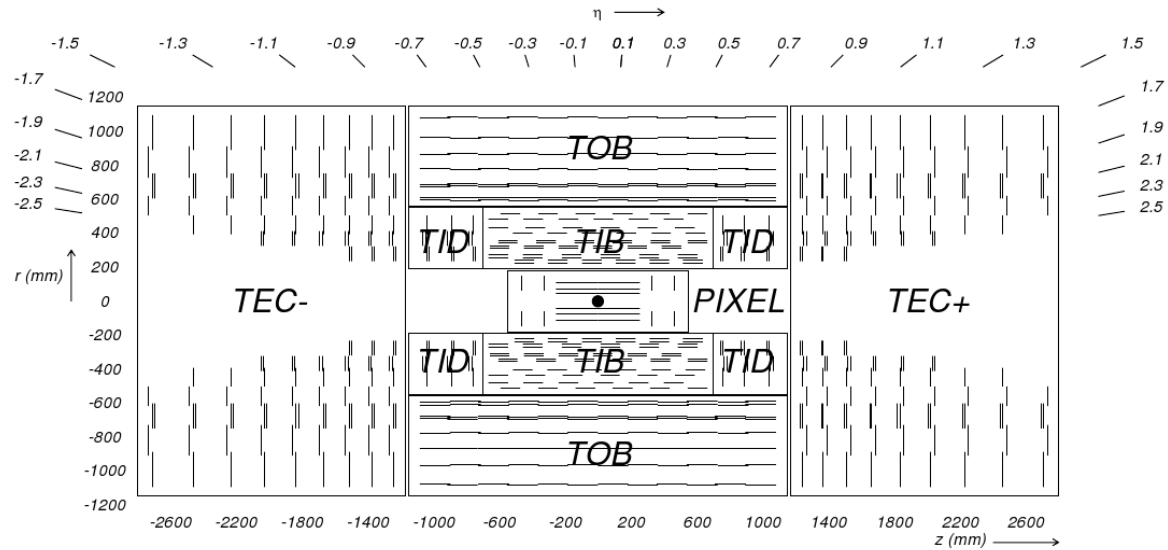


Figure 2.7: View of the CMS tracker in the  $rz$ -plane. Each line represents a detector module. Figure taken from Ref. [69].

The pixel detector is made of 1440 pixel modules installed in the tracker section closest to the interaction region. It covers the pseudorapidity range  $|\eta| < 2.5$  with three Barrel Pixel (BPix) layers and two Forward Pixel (FPix) disks. The BPix layers are placed at a radii of 4.4 cm, 7.3 cm and 10.2 cm from the beam axis, while the FPix disks are located, on each side of the IP, at a longitudinal distance of  $z = \pm 34.5$  cm and  $z = \pm 46.5$  cm. The BPix (FPix) detectors contain 48 (18) million silicon pixels, each with a cell size of  $100 \times 150 \mu\text{m}^2$ . The arrangement of the pixel detector modules provides three tracking hits over the full tracker coverage, and a spatial resolution of  $15\text{-}20 \mu\text{m}$  ( $15 \mu\text{m}$ ) in the barrel (forward) region.

The silicon-strip tracker contains 9.3 million strips divided in 24244 silicon sensors, covering the region between the pixel detector and the ECAL. In the barrel region, the strip tracker is composed of the Tracker Inner Barrel (TIB) made of four concentric

cylinders placed at a radius between 25.5 cm and 49.8 cm, and the Tracker Outer Barrel (TOB) which consists of a wheel-like structure, containing six cylinders, with an inner (outer) radius of 55.5 cm (116 cm). The pseudorapidity coverage of the strip tracker is extended up to  $|\eta| = 2.5$  with three Tracker Inner Disks (TID) and nine Tracker EndCap (TEC) disks, installed on each endcap section along  $80\text{ cm} < |z| < 90\text{ cm}$  and  $124\text{ cm} < |z| < 282\text{ cm}$ , accordingly. The strip detector modules used in the TIB, TID and inner four TEC rings are made of one 320  $\mu\text{m}$ -thick sensor, while those used in the TOB and outer five TEC rings are made of two 500  $\mu\text{m}$ -thick sensors. The strip pitch varies between 80  $\mu\text{m}$ -120  $\mu\text{m}$ , 100  $\mu\text{m}$ -141  $\mu\text{m}$ , 122  $\mu\text{m}$ -183  $\mu\text{m}$ , and 97  $\mu\text{m}$ -184  $\mu\text{m}$ , in the TIB, TID, TOB and TEC, respectively. The strip tracker can achieve a single point resolution of 230  $\mu\text{m}$  (530  $\mu\text{m}$ ) and a longitudinal resolution of 35  $\mu\text{m}$  (50  $\mu\text{m}$ ) in the TIB (TOB).

### 2.2.1.2 Electromagnetic calorimeter

The ECAL of the CMS is a hermetic homogeneous calorimeter composed of 75848 lead-tungstate ( $\text{PbWO}_4$ ) crystals. The ECAL is designed to fully absorb and measure the energy of electrons and photons. Each crystal has a small Molière radius (2.2 cm), a short radiation length (0.89 cm), and a high density ( $8.28\text{ g cm}^{-3}$ ). When a high-energy electron or photon interacts with the nuclei of the ECAL crystals, it generates a cascade of electromagnetic particles ( $e^-$ ,  $e^+$  and  $\gamma$ ) and induces the emission of blue-scintillation light ( $\lambda \approx 420\text{ nm}$ ), which is then measured in photodetectors. The total amount of scintillation light produced is proportional to the energy deposited in the crystals by the electrons and photons. In order to cope with the running conditions of the LHC, the crystals are designed to have a fast response (25 ns), and be optically transparent and radiation-hard.

The ECAL is installed between the silicon-strip tracker and the HCAL. It is divided in a cylindrical-barrel section (EB) and two endcap rings (EE), one on each side of the IP. The EB is made of 61200 crystals of 23 cm long, covering the pseudorapidity range  $|\eta| < 1.48$  with a granularity of 170-fold in  $\eta$  and 360-fold in  $\phi$ . The crystals are grouped in modules of either 400 or 500 units, and four modules are assembled in so-called supermodules. The EB has a total of 36 supermodules, each covering  $20^\circ$  in  $\phi$  with 1700 crystals. The scintillation light is measured in the EB with Avalanche PhotoDiodes (APD), mounted in pairs on the back of each crystal. Each APD is operated, with a high-voltage power supply system, at gain 50 and a voltage between 340 V-430 V. The schematic layout and geometric view of the ECAL are shown in Fig. 2.8.

The EE rings are installed at  $z = \pm 3.15\text{ m}$ , extending the coverage of the ECAL up

## 2.2. THE COMPACT MUON SOLENOID

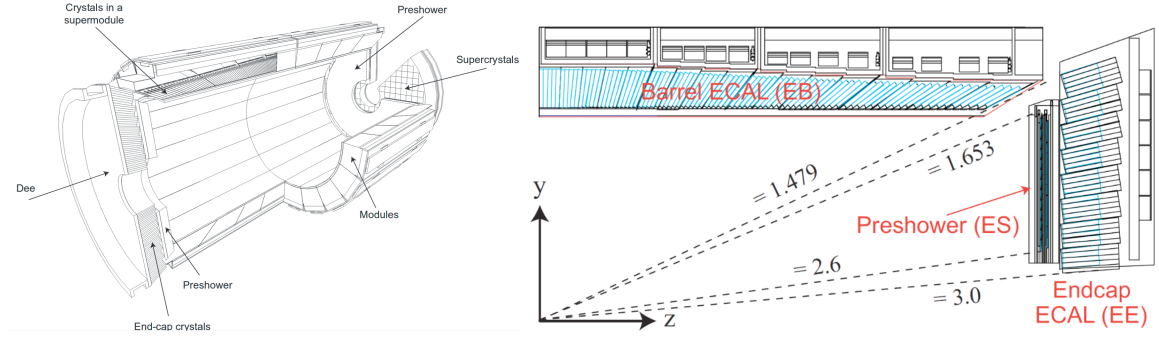


Figure 2.8: Schematic layout [69] (right) of the CMS electromagnetic calorimeter, and its corresponding one-quarter geometric view [78] (left).

to  $|\eta| = 3.0$ . The EE consists of 14648 crystals of 22 cm long, assembled in units of  $5 \times 5$  crystals known as SuperCrystals (SC). Each EE ring is divided in two halves, each containing 156 SCs. A single-stage photomultiplier called Vacuum PhotoTriodes (VPT) attached to the back of each EE crystal is used to measure the scintillation photons. The VPT has a diameter of 25 mm, a quantum efficiency of 22% at a wavelength of 430 nm, and a gain of 10.2 at zero magnetic field.

An additional calorimeter called the Preshower detector is installed in the endcap rings between the tracker and the EE. The Preshower is an electromagnetic sampling calorimeter of 20 cm thick, optimised to identify photons from neutral pion decays. It is composed of two layers of lead absorbers interleaved with 4300 silicon sensors organized in 32 strips. Each silicon sensor has a thickness of 320  $\mu\text{m}$  and an active area of  $63 \times 63 \text{ mm}^2$ . Incoming photons and electrons initiate an electromagnetic shower when they interact with the lead absorbers. The energy deposited in the absorbers and the transverse profile of the shower are measured in the silicon strips.

The response of the crystals and the signal amplification of the APDs depend on the operating temperature. As a result, a water flow cooling system is installed to keep the crystals and sensors at a stable temperature of  $18.0(5)^\circ\text{C}$ . Moreover, the transparency of the crystals to scintillation light is affected by the radiation dose due to the formation of colour centers which absorbs part of the light. The variation of the crystal transparency is monitored using laser pulses introduced onto the crystals at a frequency of 80 Hz. The laser monitoring system uses two blue lasers ( $\lambda \approx 440 \text{ nm}$ ) to track the radiation-induced transparency variations, which are then corrected by recalibrating the detector.

The energy resolution of the ECAL can be affected by several sources, such as the fluctuations in the shower, crystal non-uniformities, calibration errors, and noise in

the photodetectors. The relative energy resolution of the ECAL is parameterized as a function of the measured energy  $E$  via:

$$\left(\frac{\sigma_E}{E}\right)^2 = \left(\frac{2.8\%}{\sqrt{E/\text{GeV}}}\right)^2 + \left(\frac{12\%}{E/\text{GeV}}\right)^2 + (0.3\%) \quad (2.4)$$

### 2.2.1.3 Hadronic calorimeter

The HCAL is a hermetic sampling calorimeter made of 70000 plastic-scintillator tiles interleaved with absorber plates. The goal of the HCAL is to completely absorb and measure the energy of hadrons. When a hadron hits an absorber plate, it induces a shower of particles through the successive absorber layers. The secondary particles produced in the cascade pass through the plastic tiles, located in between the absorbers, leading to the emission of scintillator light at a peak wavelength of  $\sim 440\text{ nm}$ . Photons generated on each tile are collected with WaveLength-Shifting (WLS) fibres fabricated in a double-clad configuration with a diameter of 0.94 mm. The WLS fibres shifts the scintillator light to the green spectrum (515 nm) and pass it to fibre-optic waveguides which then transfers the light to a phototransducer. The scintillator tiles are grouped in trays of  $5^\circ$  wide in  $\phi$ . A geometric view of the CMS, showing the different components of the HCAL, is presented in Fig. 2.9.

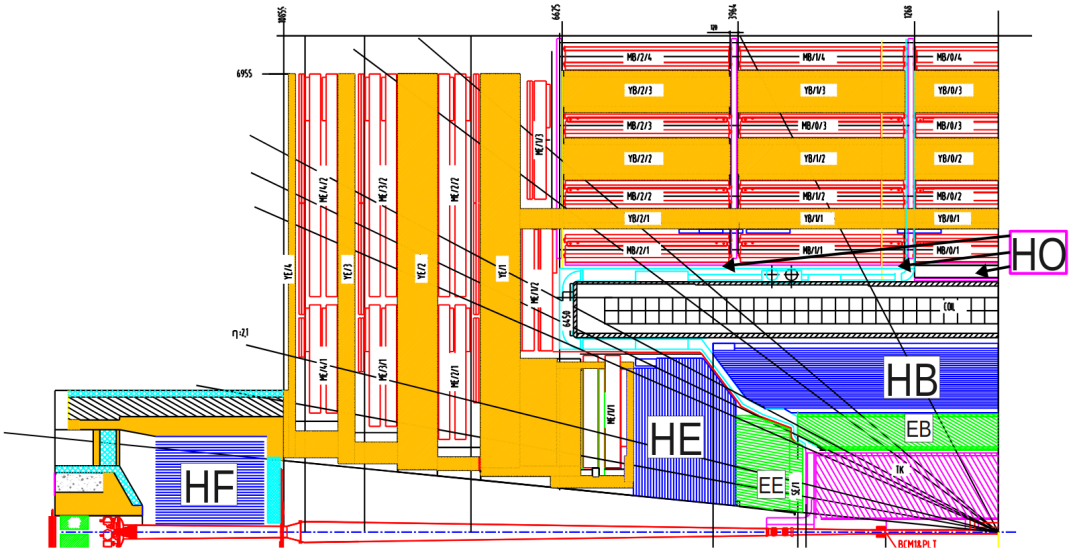


Figure 2.9: Geometric view of one quarter of the CMS detector, displaying the subdetectors of the hadron calorimeter. Figure taken from Ref. [76].

The central region of the HCAL is composed of the Hadron-Barrel (HB) calorimeter installed between the ECAL and the magnet coil, and the Hadron-Outer (HO) calorimeter placed outside of the solenoid volume. The HB covers the pseudorapidity range  $|\eta| < 1.3$ , and it is divided in two half-barrel sections. The absorber consists of 36 wedges of brass and steel plates aligned parallel to the z-axis. Each HB wedge is splitted in four azimuthal sections. The HB scintillator tiles are divided in 16  $\eta$ -parts providing a segmentation of  $0.087 \times 0.087$  in  $\eta - \phi$ . The HB photosensors consist of Hybrid PhotoDiode (HPD) transducers. The HPD contains 19 pixels of  $20 \text{ mm}^2$  in size and has an approximate gain of 2000.

The HO is used to measure the energy of the tail of the particle shower deposited after the HB. The HO is divided in five disks corresponding to each of the five barrel wheels of the flux-return yoke. Each HO ring is divided into twelve  $\phi$  sectors, each separated in six trays. The HO has 2730 scintillator tiles of 10 mm thick organized in 422 trays, offering the same granularity in  $\eta - \phi$  as the HB. The HO uses a multipixel Geiger-mode APD, known as Silicon PhotoMultiplier (SiPM), to detect photons.

The coverage of the HCAL is extended in the forward region to  $|\eta| = 3$  with the Hadron-Endcap (HE) calorimeter and up to  $|\eta| = 5.2$  with the Hadron-Forward (HF) calorimeter. The HE is located in the endcap rings and its absorber is made of two 79 mm-thick plates of cartridge brass separated by 9 mm. The HE contains 20916 plastic tiles and has a  $\eta - \phi$  granularity of  $0.17 \times 0.17$ . The HE also uses HPDs to measure the scintillor light.

The HF is divided in 36 wedges of  $20^\circ$  wide in  $\phi$  and its front face is located at  $z = \pm 11.2 \text{ m}$ , on each side of the IP. Since the HF experience the largest energy deposits from the beam collisions, its design has been optimised to handle high levels of radiation. The HF absorber consists of a 1.7 m-depth cylindrical structure made of 5 mm-thick steel-grooved plates, while the HF active medium is composed of quartz fibres of polymer hard-cladding and fused-silica core. The signal consists of Cherenkov light generated when energetic charged particles from the shower traverse the quartz fibres. The Cherenkov light is measured by multi-anode PhotoMultiplier Tubes (PMT) shielded behind 40 cm of steel. The HF fibres are inserted in the absorber grooves along the beam line in two longitudinal segments. Long fibres are inserted over the full absorber depth while short fibres starts at a depth of 22 cm from the front face covering the back of the absorber. Since most of the energy of electrons and photons is deposited in the first 22 cm while hadrons are able to penetrate more in the HF absorber, the difference in energy measured in the long and short fibres is used to determine the electromagnetic and

hadronic components of the shower.

#### 2.2.1.4 Muon detectors

The CMS muon tracking system measures the momentum and charge of muons in the fiducial region  $|\eta| < 2.4$ . It is divided in four stations corresponding to four concentric cylinders in the barrel region and to four disks on each endcap section. Fig. 2.10 shows a geometric view of one quadrant of the CMS muon system. The dense material of the calorimeters and the solenoid magnet absorbs most of the hadrons, electrons and photons, while energetic muons are able to reach the muon stations loosing only a small fraction of their energy. Muons are detected in CMS using three type of gaseous technologies: Drift Tubes (DT), Cathode Strip Chambers (CSC) and Resistive Plate Chambers (RPC).

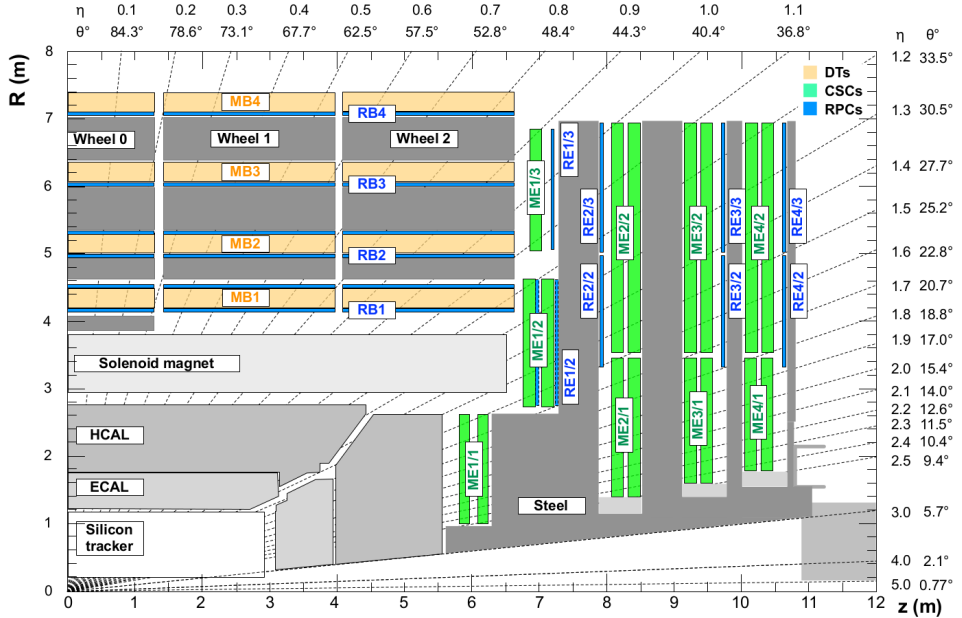


Figure 2.10: Geometric view of one quadrant the CMS detector in the  $rz$ -plane. Each chamber of the muon system is shown. Figure taken from Ref. [79].

The DT detectors are used in the barrel region of the muon system ( $|\eta| < 1.2$ ). A DT consists of a  $50\text{ }\mu\text{m}$ -diameter anode wire placed inside a rectangular tube connected to two cathode strips and filled with a gas mixture of 85% of Ar and 15% of  $\text{CO}_2$ . The layout of a DT cell is displayed on the left of Fig. 2.11. When a charged particle passes through a DT, it ionizes the gas releasing electrons that are then detected in the anode wire. The DT system is composed of 172000 anode wires of 2.4 m length. There are four DT

chambers in each of the five barrel wheels and twelve azimuthal sectors of the yoke. In total, the fourth station contain 70 DT chambers and the first three stations contain 60 DT chambers each. Four layers, each containing up to 60 DTs, are grouped in units called SuperLayers (SL). The DT chambers of the three inner stations (outermost station) are made of three (two) SLs. The first and third SL, as shown on the right of Fig. 2.11, have their anode wires installed parallel to the z-axis to measure the bending in the  $r\text{-}\phi$  plane, while the anode wires of the second SL are placed orthogonal to the beam line to measure the position along the z-axis. The SLs of the fourth station only have anode wires parallel to the z-axis. The SLs measure the position and angle of the track segments with a precision of 1.5 mm and 20 mrad, respectively.

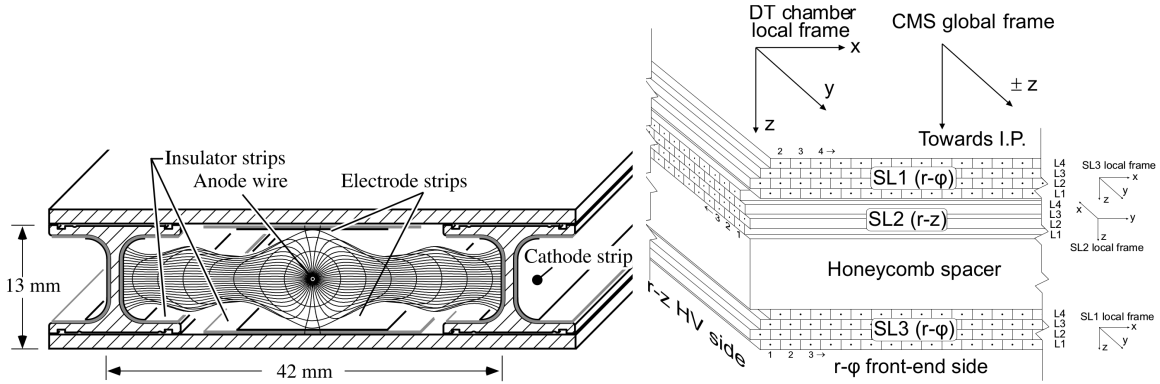


Figure 2.11: Schematic layout of a DT cell (left) and a DT chamber (right). Figures taken from [80].

The two endcap sections use 540 CSCs covering a pseudorapidity range  $0.9 < |\eta| < 2.4$ . The CSC system is designed to cope with the higher rate of particles and the large non-uniform magnetic field present in the forward region. A CSC is made of six anode wire planes crossed with seven cooper cathode strips within a gas mixture of 40% Ar, 50% CO<sub>2</sub>, and 10% CF<sub>4</sub>, forming a multiwire proportional chamber. The CSCs are operated at 3.6 kV with a gas gain of  $7 \times 10^4$ , and are organized in chambers installed perpendicular to the beam pipe. The CSC chambers are trapezoidal and cover either 10° or 20° in  $\phi$ , and they overlap providing contiguous coverage in  $\phi$ . The cathode strips are milled in panels along constant  $\Delta\phi$ -width and provide measurements in the  $r\text{-}\phi$  plane, while the anode wires are placed azimuthally and measure the beam-crossing time and pseudorapidity of muons. The CSC system has a total of 266112 cathode-strip and 210816 anode-wire read-out channels. A schematic layout of a CSC is shown in Fig. 2.12.

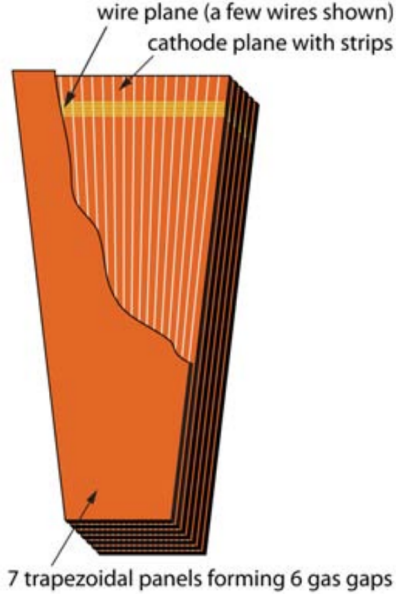


Figure 2.12: Schematic layout of a CSC. Figure taken from [69].

To improve the measurement of the timing between muon hits, the barrel and endcap regions are complemented with RPC detectors. A RPC module consists of an anode plate parallel to a cathode plate, as shown in Fig. 2.13. The RPC plates are separated by a gap filled with a gas mixture of 96.2%  $\text{C}_2\text{H}_2\text{F}_4$ , 3.5%  $i\text{C}_4\text{H}_{10}$  and 0.3%  $\text{SF}_6$ , and operated in avalanche mode with read-out strips in between. There are 480 (576) RPC chambers in the barrel (endcap) region. Each RPC chamber consists of two or three modules of up to 96 strips each. Each RPC strip covers  $0.31^\circ$  in  $\phi$ . The RPC chambers are organized in six coaxial cylinders in the barrel region and four rings in the endcaps, covering the pseudorapidity region up to  $|\eta| = 1.9$ . The innermost ring span  $20^\circ$  in  $\phi$  while the other rings span  $10^\circ$ . The RPC modules are optimised for fast muon triggering by detecting ionising events faster than the time interval between two bunch crossings (25 ns). They provide a good timing resolution but with a coarser spatial granularity compared to DTs and CSCs. The RPCs also allow to resolve ambiguities between tracks made from multiple hits in the muon chambers.

### 2.2.2 Trigger system

At LHC design conditions, the two beams crosses each IP every 25 ns, equivalent to a frequency of 40 MHz. Once a collision is recorded by CMS, all detector channels are readout and the data is sent to the CERN main computing farm, known as the Tier-0, to

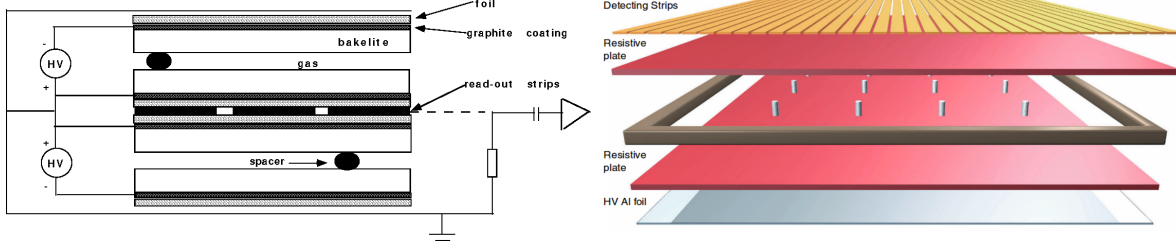


Figure 2.13: Cross section view (left) [81] and exploded view (right) [82] of a RPC module.

be further processed with the CMS SoftWare (CMSSW). However, the Tier-0 processing rate is limited by its CPU performance and storage capacity. As a result, the input rate of data transferred to the Tier-0 has to be kept below 1 kHz to avoid overflowing the computing centre.

To reach this goal, CMS has implemented a two-level trigger system designed to select events of interest for physics analysis. The first level, known as the Level-1 (L1) trigger, lowers the collision rate to an output rate of 100 kHz by filtering events using custom hardware. The next trigger level, called the High Level Trigger (HLT), is performed in a cluster of computers located in the CMS experimental cavern. The HLT software algorithms further reduce the data rate down the limit required by the Tier-0.

### 2.2.2.1 Level-1 trigger

The L1 trigger system [83] is designed to handle the large collision rate of the LHC. To accomplish this goal, the L1 trigger is made of custom hardware modules optimised to process the events with a latency of less than 4  $\mu$ s. The L1 trigger is divided in two parts: the L1 calorimeter and the L1 muon trigger.

The data from each subdetector is organized in units called Trigger Primitives (TP). The calorimeter TP are derived from the Trigger Towers (TT), each corresponding to a region of  $0.087 \times 0.087$  in  $\eta - \phi$  (represents  $5 \times 5$  crystals in the ECAL). In the case of muons, a TP corresponds to a segment in either the DT or CSC systems. The information of the inner tracker is not used in the L1 trigger since the tracker data can not be currently readout within a bunch crossing time of 25 ns. As a result, the L1 calorimeter trigger does not discriminate between electrons and photons. The output of the L1 muon and calorimeter triggers is combined in the L1 Global Trigger (GT), which then takes the final decision to either reject or accept the event.

The L1 trigger decision is determined according to a set of user-defined L1 trigger

conditions. The L1 criteria are organized in a menu made of different algorithms which are programmed by the users and hard-coded in the firmware of a Field-Programmable Gate Array (FPGA). Some typical conditions used to define the L1 algorithms include setting a minimum  $p_T$  threshold or  $\eta$  range on the L1 objects, or requiring events to have a given amount of L1 candidates. If an event passes the conditions of at least one of the L1 algorithms, the whole CMS detector is readout and the data is then sent to the HLT computers. The L1 menu was updated several times during the period of data taking, to adapt to the changes in the LHC beam conditions and physics requirements.

In order to reduce the contribution from cosmic muons and also suppresses pre-firing from the calorimeters caused by particles interacting in the photomultipliers, the events processed by the L1 trigger are required to be associated to a bunch crossing. The Beam Pick-up Timing eXperiment (BPTX) detectors, installed at a distance of  $z = \pm 175$  m on each side of the IP, are used to select valid bunch crossings by checking for a coincidence of the signals on each side.

The L1 system underwent, between 2014 and 2015, an extensive upgrade that included a complete replacement of the electronics and the data acquisition system. The previous L1 trigger, used during LHC Run-1 and 2015, is referred in this manuscript as the legacy L1 trigger, while the upgraded L1 trigger, deployed before the pPb collision run in 2016, is called Stage-2 L1 trigger.

**Legacy L1 trigger.** The legacy L1 trigger [83] was used in CMS until the end of 2015, covering the entire LHC Run-1 and beginning of Run-2 data taking periods. The events from p-p and Pb-Pb collisions at  $\sqrt{s_{\text{NN}}} = 5.02$  TeV were selected using the legacy L1 trigger. Fig. 2.14 shows a diagram of the legacy L1 trigger system.

In the legacy L1 trigger, the transverse energy  $E_T$  values are readout from each ECAL, HF and HCAL TT, and then sent to the Regional Calorimeter Trigger (RCT). The RCT processes the raw data and produces 72 electron-photon ( $e/\gamma$ ) candidates (identified as energy clusters mainly deposited in the ECAL), computes the  $E_T$  in the HF region and derives 396  $E_T$  sums of  $4 \times 4$  TT regions. The Global Calorimeter Trigger (GCT) then receives the objects from the RCT and reconstructs jets and hadronic tau decays based on the regional  $E_T$  sums, sorts the  $e/\gamma$  candidates according to their  $E_T$ , and computes global quantities such as the missing or total  $E_T$ . Eight  $e/\gamma$  candidates, eight jets, four tau candidates, the HF  $E_T$ , and the global quantities are then sent to the GT.

The legacy L1 muon trigger follows a detector-based design. The DT and CSC hit measurements are used by the front-end trigger electronics to reconstruct track segments

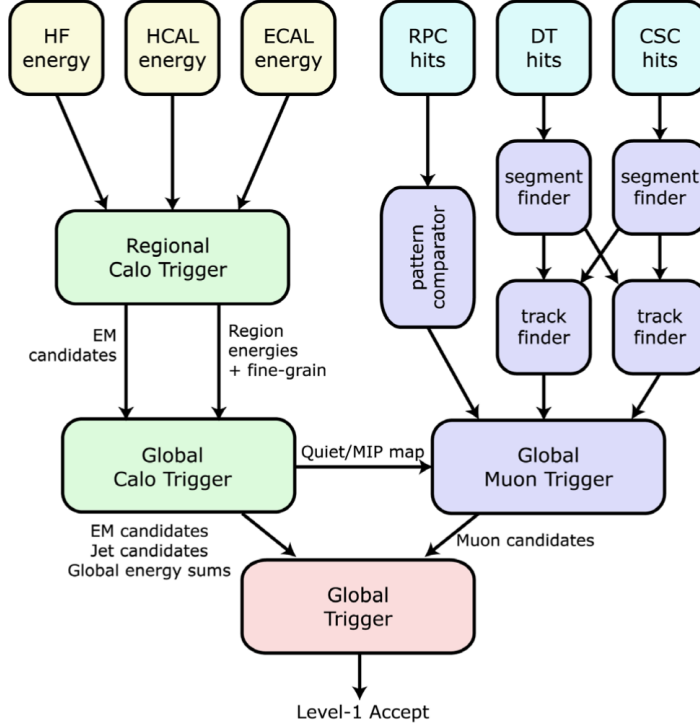


Figure 2.14: Diagram of the legacy L1 trigger of CMS. Figure taken from Ref. [84]

in each muon station. Regional track finders (TF), one for each muon subsystem, sort the track segments and identify muons using pattern recognition algorithms. The hardware modules of the DT (CSC) TFs consists of 72 (12) Versa Module Eurocard (VME) boards. The muon momentum is estimated based on the bending of the track along the magnetic field. The position of each muon detector hit is converted to  $\eta - \phi$  coordinates using lookup tables derived from simulation. To cover the overlap region between the CSC and DT muon systems, the information of their TFs is combined. The RPC hits are directly sent to a pattern comparator trigger (PACT), which find muon candidates by comparing the RPC measurements to predefined patterns. Each muon TF determines the position in  $\eta - \phi$  and the  $p_T$  of the muon candidates, and also assigns a quality value based on the position and number of muon stations used to form the muon track.

On every bunch crossing, the CSC and DT TFs transfer, each one, four muon candidates to the Global Muon Trigger (GMT), while the RPC trigger sends eight muon candidates. The GMT then proceeds to merge the muon tracks if they have been identified by several muon subsystems, and assigns a three-bit quality code to the muon tracks depending on the information provided by each TF. All muon candidates are ranked in

the GMT based on their  $p_T$  and quality code, and the four highest ranked candidates are then transferred to the GT. The quality bits assigned to the L1 muon candidates are:

- **Bits 0 to 1:** Represent empty or halo muons. Not used for physics.
- **Bits 2 to 4:** Assigned to very low quality muon tracks. Kept only in the open L1 muon algorithms.
- **Bit 5:** Muon candidate found by the DT or CSC TFs, but not confirmed by the RPC PACT.
- **Bit 6:** Muon candidate found by the RPC PACT, but not confirmed by the DT or CSC TFs.
- **Bit 7:** Muon candidate detected by the DT or CSC TFs, and also by the RPC PACT.

The legacy GT takes the final L1 decision based on the information provided by the GMT and the GCT. It is able to evaluate up to 128 L1 algorithms.

**Stage-2 L1 trigger.** The Stage-2 L1 trigger system [77] was deployed in CMS at the beginning of 2016 and was used during the data taking period of p-Pb collisions at  $\sqrt{s_{NN}} = 8.16 \text{ TeV}$ . A diagram of the upgraded L1 trigger system is shown in Fig. 2.15.

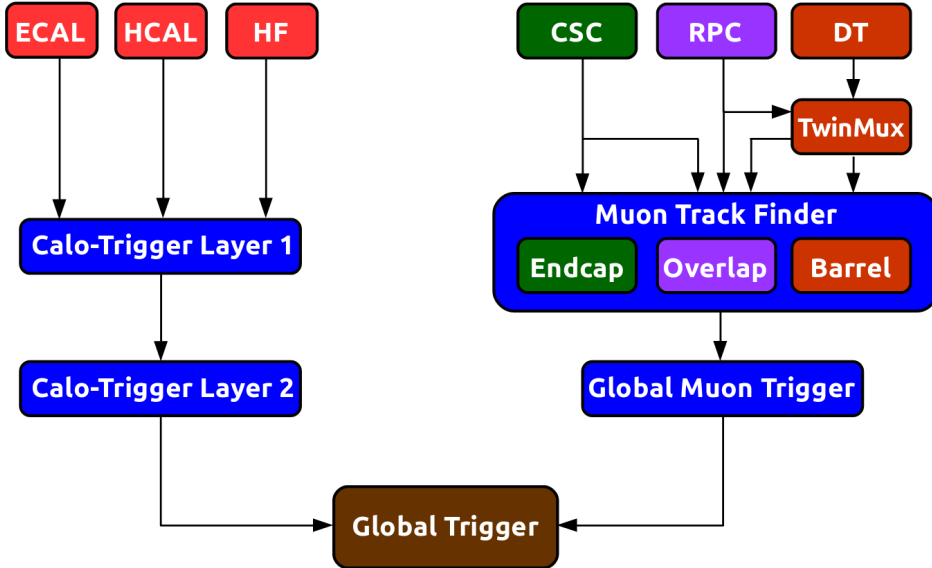


Figure 2.15: Diagram of the CMS L1 trigger used in 2016.

The electronic system of the Stage-2 L1 trigger consists of Xilinx Virtex-7 FPGAs mounted on Advanced Mezzanine Cards (AMC), designed according to the micro Telecommunications Computing Architecture ( $\mu$ TCA) standard. Compared to the VME standard

employed in its predecessor, the  $\mu$ TCA standard provides higher scalability, flexibility and bandwidth. The communication links between the L1 boards were upgraded from copper serial links (limited to  $1.2 \text{ Gbs}^{-1}$  in the legacy L1 trigger) to high speed optical serial links capable of handling a bandwidth of up to  $10 \text{ Gbs}^{-1}$ .

The Stage-2 L1 calorimeter [85] trigger is divided in two separate processing layers and its architecture follows a time-multiplexed trigger design (the data is splitted in bunch-crossing intervals instead of detector regions). The first layer (Layer-1) collects data from the calorimeter TTs with 36 trigger processor cards and then distributes all data for a given bunch crossing to one of the nine multipurpose FPGAs of the second layer (Layer-2). The Layer-2 use the TT data to reconstruct  $e/\gamma$  candidates, jets, and taus (decaying to hadrons), and compute global energy quantities. Lookup tables are used to perform the shape pattern recognition and the energy calibration.

In the case of the L1 muon trigger [86], its architecture is upgraded following a regional based approach. The data from the different muon subsystems is combined at an earlier stage than in the legacy L1 trigger and L1 muon tracks are reconstructed in three regions: barrel ( $|\eta| < 0.8$ ), overlap ( $0.8 < |\eta| < 1.25$ ), and endcap ( $1.25 < |\eta| < 2.4$ ). The Endcap-Muon TF (EMTF) is designed to process the information from the CSC and RPC modules, however it only received data from the CSC system during 2016 since the RPC concentrator card was still been commissioning. The Barrel-Muon TF (BMTF) builds muon candidates using RPC hits and DT segments reconstructed in the central region. The transition area ( $|\eta| \approx 1.04$ ) between the endcap and barrel sections is covered with the Overlap-Muon TF (OMTF), which takes into account the data from the three muon subsystems. The DT and RPC segments from the barrel region are collected by an intermediate layer called the TwinMux system, which concentrates data and distributes it to the BMTF and OMTF.

The upgraded GMT, referred as  $\mu$ GMT, receives up to 36 L1 muon candidates from each L1 muon TF. The  $\mu$ GMT sorts the muon tracks, removes duplicate muons found by different TFs and ranks the muon candidates by their  $p_T$  and track quality. The eight highest ranked L1 muon candidates are then sent to the GT. The information from the  $\mu$ GMT and the Layer-2 is used by the upgraded GT to evaluate up to 512 L1 algorithms and determine the final L1 decision.

### 2.2.2.2 High level trigger

The HLT is executed on a single processor farm composed of an array of multi-core computers running a Linux-based operating system known as Scientific Linux. During

2016, approximately 20000 cores were employed to run the HLT [87]. The HLT software is organized in readout, builder and filter units. The readout unit extracts the information from all CMS subsystems once an event passes the L1 trigger. The builder unit assembles the raw data provided by the readout unit to build detector segments, hits and clusters. The assembled data is subsequently sent to the filter unit which performs the reconstruction of physics objects and selects events for data analysis. The logic of the HLT reconstruction framework is similar to what is used in offline reconstruction but optimised to handle high input data rates ( $\leq 100\text{kHz}$ ).

The structure of the HLT algorithms is organized in a set of processing steps, called HLT path, that runs the reconstruction and selection of events. Each HLT path consists of a sequence of processing units that runs in a predefined order and selects events based on user-defined conditions, such as requiring the presence of muons with  $p_T$  larger than a given threshold. Once an event has been accepted by the HLT, the CMS data is kept temporarily on disk and eventually sent to the Tier-0 computing facility for further offline processing. The HLT output rate is constrained by the size of the event data and the Tier-0 processing power. The average data size of an event in p-p collisions is around 500 kb, while in central Pb-Pb collisions can reach values as large as 3 Mb due to the higher particle multiplicity.

For the analyses presented in this manuscript, the data was triggered requiring the presence of identified muons. The reconstruction of muon candidates in the HLT is performed in two steps. The first one, referred as the Level-2 (L2), reconstructs muon tracks using data from the muon system only, while the next step, known as the Level-3 (L3), combines the information from both the inner tracker and the muon stations.

**HLT L2 muon reconstruction.** The L2 muon algorithm starts by performing a local reconstruction of the muon detectors to determine the hits on each muon chamber. The CSC and DT hits are then combined to form segments, which are only kept if found near a L1 muon candidate. The muon segments are then recursively fitted with a Kalman Filter (KF) technique [88] to build the L2 muon tracks. Duplicate tracks are filtered by removing L2 muon tracks that share hits. The KF fit is constrained to the position of the IP to improved the  $p_T$  resolution of L2 muon candidates.

**HLT L3 muon reconstruction.** The L3 muon reconstruction improves the momentum resolution by combining the measurements from the inner tracker and the muon chambers. The reconstruction of all tracks in the inner tracker (hereafter called tracker

tracks) is not done at HLT due to timing constraints. Instead, a regional tracking is performed by only reconstructing tracker tracks close to the L2 muon candidates using three different seeding algorithms. In the first case, the seeds are defined by extrapolating the parameters (position and  $p_T$ ) of the L2 muon tracks to the outer surface of the inner tracker. The second seeding procedure takes the extrapolated L2 muon tracks and updates their parameters with the hit information from the outermost layers of the silicon-strip tracker. And the third seeding algorithm uses segments from two pixel hits measured in consecutive layers found in a narrow  $\eta - \phi$  region around each L2 muon track. Each seed is then used to build the tracker tracks with a KF fit. The reconstructed tracker and L2 muon tracks are propagated to a common surface, and then matched by comparing their goodness-of-fit  $\chi^2$ . If a L2 muon track and a tracker track is matched, the hits of both tracks are then combined and refitted to form the L3 muon track.

### 2.2.3 Reconstruction

The aim of the CMS event reconstruction algorithms is to build and identify the physics objects generated during the collision by processing the raw data recorded by the CMS detector. The reconstruction algorithms are implemented in CMSSW framework. Once an event is selected by the HLT, the detector information is then transferred to the Tier-0 computing centre and processed with CMSSW. The reconstruction software starts by building the hits, segments and clusters, measured in each of the CMS subdetectors. Afterwards, it processes the detector information to form physics objects such as charged-particle tracks, muons, electrons, photons and jets. Global event quantities, like the missing transverse energy (MET), are computed by combining the information from the different reconstructed objects. The reconstruction of muons and the MET is described in Section 2.2.3.1 and Section 2.2.3.2, respectively.

#### 2.2.3.1 Muon reconstruction

Muon candidates are reconstructed in CMS [89] using the information from the inner tracker and the muon system. Tracks formed in the muon system only are called standalone-muon tracks, while those built in the inner tracker and matched to a hit in the muon system are referred to as tracker-muon tracks. Global-muon tracks are reconstructed by matching a tracker track with a standalone-muon track. The three different types of muon tracks used in CMS are displayed in Fig. 2.16.

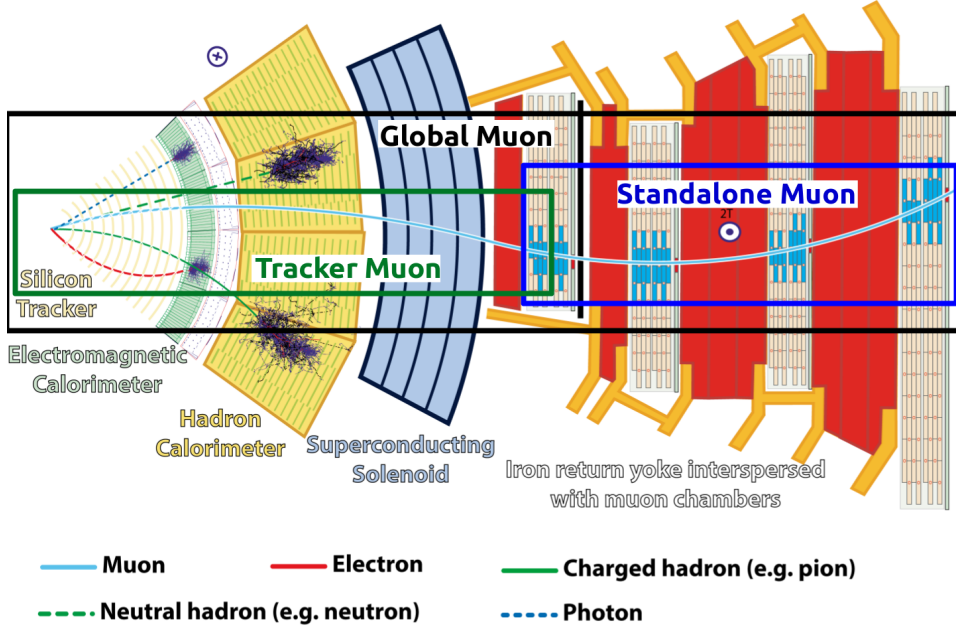


Figure 2.16: Cross section view of the CMS detector showing how particles interact in the CMS. The different types of muon tracks are indicated in boxes. Figure taken from Ref. [90].

**Standalone muons.** The standalone muon reconstruction starts with the formation of segments made from a linear interpolation of the position of hits measured in the DT or CSC layers. Each track segment has an associated state vector representing its position, direction and  $p_T$ . The state vector of the segments built in the innermost muon station is used to seed the muon track fit.

In the barrel region, tracks are built by fitting the DT segments with a KF algorithm [88], starting from the innermost muon chamber. Moreover, since the magnetic field in the endcap sections is not uniform, the hits of the CSC segments are used directly to perform the KF fit. The RPC hits are also included in the KF. In the case that no hits are found between muon layers, the state vector of the muon track is propagated to the next layer taking into account the magnetic field and the interaction of muons with the CMS detector material.

The track building procedure is iterated while progressing towards the outer muon chambers. The  $\chi^2$  value between the detector hits and the position of the track projected onto the muon chambers is computed in each step. The hits with large  $\chi^2$  values are excluded from the KF fit and the parameters of the track are updated accordingly. The

track fit algorithm stops when it reaches the last muon station. Subsequently, the KF algorithm is performed backwards working from the outermost to the innermost muon chambers, completing the standalone-muon track. Finally, the standalone-muon tracks are extrapolated to the closest approach to the beam line and their position is required to be close to the IP.

**Global muons.** The global muon reconstruction improves the identification of muons by including the information from the inner tracker. The global muon tracking begins by propagating the standalone-muon tracks to the outer surface of the silicon-strip tracker. A tracker layer consistent with the position of the propagated standalone muon defines a common surface. Hits found in the inner tracker around the common surface are used to reconstruct tracker tracks.

Tracker-track segments are built from pairs (triplets), made of two (three), hits reconstructed in adjacent inner-tracker layers. These segments are then employed to seed an iterative KF combinatorial track finder. The standard tracking procedure runs ten different iterations. The first three iterations reconstruct low- $p_T$ , high- $p_T$  and displaced (within a radial distance  $R < 5\text{ cm}$ ) tracks seeded with pixel-hit triplets. The next iteration is meant to recover tracks with one or two missing hits by seeding with pixel-hit pairs instead. The fifth iteration build displaced tracks ( $R < 7\text{ cm}$ ) seeded by triplets from pixel and strip hits. The following two iterations reconstruct very displaced tracks ( $R < 60\text{ cm}$ ) seeded by strip-hit triplets. The eighth iteration aims to find tracks within the core of high- $p_T$  jets seeded by pairs of pixel and strip hits. And the last two iterations build tracks seeded with hits and segments from the muon chambers, to improve the muon reconstruction efficiency. The hits associated to tracks formed in a given iteration are excluded in the subsequent iterations to avoid duplicating tracks. The rate of misreconstructed tracks is kept low in each step by applying a set of quality criteria on the goodness-of-fit  $\chi^2$  and the number of hits used, and by requiring the tracks to be consistent with a charged-particle trajectory originating from the primary vertex.

The tracker track and the propagated standalone-muon track are then matched according to their  $p_T$ , and the hits from both tracks are refitted to derive the global-muon candidate. If multiple global-muon tracks are found, the track with the best  $\chi^2$  fit value is kept.

**Tracker muons.** The tracker-muon candidates are built by propagating all tracker tracks with  $p_T > 0.5\text{ GeV}/c$  and total momemtum  $p > 2.5\text{ GeV}/c$ , to the innermost muon

station. The propagated track is then considered a tracker-muon track if it matches, along the transverse plane, at least one hit reconstructed in the inner muon chambers.

**Tracking in Pb-Pb collisions.** A modified version of the tracker track reconstruction was employed during Pb-Pb collisions at  $\sqrt{s_{\text{NN}}} = 5.02 \text{ TeV}$ , to cope with the large number of charged particles produced in central heavy-ion collisions. The tracking algorithm used to build the tracker tracks consists of seven iterations and is called ReGional Iterative Tracking (ReGIT). Instead of using all pixel hits reconstructed in the inner tracker, ReGIT performs a regional track reconstruction using only those hits found in a  $\eta - \phi$  area around each standalone-muon track. The ReGIT iterations follow the same logic as the standard tracking, excluding the three iterations corresponding to low- $p_T$ , very displaced, and high- $p_T$  jet tracks. In each iteration, tracks made with ReGIT are required to have a  $p_T > 0.8 \text{ GeV}/c$  and at least eight hits, which is a tighter criteria compared to the standard track reconstruction.

### 2.2.3.2 Missing transverse momentum reconstruction

Since the CMS detector is not able to detect neutrinos, their presence is characterized by a particle momentum imbalance in the transverse plane, known as missing transverse energy ( $E_T$ ). The MET is defined as the negative vector sum of the transverse momemtum of all particles identified by CMS, as described in Eq. (2.5).

$$E_T = - \sum_{\text{particles}} \vec{p}_T \quad (2.5)$$

The Particle-Flow (PF) algorithm [91] is used to identify the particles produced in a given event. The PF algorithm is optimised to reconstruct stable particles by taking into account the information from all CMS subdetectors. The algorithm determines the momemtum of the reconstructed objects and classify them in five categories: electron, muon, photon, charged hadron and neutral hadron. The transverse momentum of all PF particles is used to compute the  $E_T$ . The performance of the MET reconstruction in p-p collision data has been documented in [92, 93].

Ideally, in an event where no neutrinos are produced, the  $E_T$  should be equal to zero. But since the momentum of particles is not measured with perfect precision, the sum of the reconstructed particles  $\vec{p}_T$  does not cancel completely due to the resolution of the detector. In order to correct for the differences in the MET resolution between simulation

## 2.2. THE COMPACT MUON SOLENOID

---

and data, the resolution of the hadronic recoil component is smeared in the simulation to match the level observed in data.



C H A P T E R



## CHARMONIA

This chapter  
BlaBla

### 3.1 Theory

### 3.2 Analysis

### 3.3 Results



1

2

3

## W BOSON PRODUCTION IN PROTON-LEAD COLLISIONS

This chapter describes the measurement of the production of W bosons in proton-lead (pPb) collisions at a nucleon-nucleon center-of-mass energy  $\sqrt{s_{\text{NN}}} = 8.16 \text{ TeV}$  with the CMS detector. As mentioned in Section ??, the primary processes that contribute at LHC energies to the production of W bosons are  $u\bar{d} \rightarrow W^+$  and  $d\bar{u} \rightarrow W^-$ . Once produced, W bosons can decay weakly to either leptons or quarks. The semi-muonic decay ( $W \rightarrow \mu\nu_\mu$ ) is of particular interest, since muons lose negligible energy in the medium and the surrounding background is small.

The individual  $W^+$  and  $W^-$  production rates are expected to be modified relative to proton-proton (pp) collisions, due to the different content of up and down quarks in the proton compared to the lead nuclei. The distribution of partons inside the nuclei can also be modified by parton shadowing (or depletion), which can alter the W boson yields at the LHC. Precise measurements of W production in pPb collisions can therefore provide strong constraints to the nuclear parton distribution functions (nPDF).

The analysis is currently been reviewed. Previous results have been published by the CMS collaboration on pPb data at  $\sqrt{s_{\text{NN}}} = 5.02 \text{ TeV}$  collected in 2013 [94]. A similar study has been performed by the ALICE [95] and the ATLAS [96] collaborations at pPb collision energies of 5.02 TeV.

The datasets and simulated samples are described in Section ?? . In Section ?? , the event selection is presented. The relevant backgrounds are introduced in Section ?? . Finally, the systematic uncertainties are discussed in Section ?? and the results are

<sup>24</sup> detailed in Section 4.2.

## <sup>25</sup> 4.1 Theory

### <sup>26</sup> 4.1.1 History of weak theory

<sup>27</sup> In the early 20th century, quantum mechanics was the standard framework of atomic  
<sup>28</sup> physics but certain processes such as the  $\beta$  decay, discovered by Ernest Rutherford in  
<sup>29</sup> 1899 [97], were not fully understood yet. At the time, the  $\beta$  decay was characterized  
<sup>30</sup> by the process  $A_i \rightarrow A_f + e^-$ , where an initial nucleus  $A_i$  decays into another nucleus  
<sup>31</sup>  $A_f$  emitting an electron during the process. In order to conserve energy, the electron  
<sup>32</sup> is required to have a fixed kinetic energy, but James Chadwick observed in 1914 that  
<sup>33</sup> the  $\beta$  rays produced a continuous energy spectrum [98, 99] in disagreement with what  
<sup>34</sup> was expected. As a way to solve the problem of the continuous  $\beta$  decay spectrum, Wolfgang  
<sup>35</sup> Pauli proposed in 1930 the existence of a new particle [100, 101]. Pauli named his particle  
<sup>36</sup> initially the neutron but later renamed it to the neutrino after the discovery of a new  
<sup>37</sup> electrically neutral particle inside the  $^{14}_7\text{Ni}$  nucleus by Chadwick in 1932 [102]. Pauli  
<sup>38</sup> described the neutrino as a neutral fermion with mass close to zero and spin 1/2 capable  
<sup>39</sup> of penetrating matter deeper than photons [100].

<sup>40</sup> Enrico Fermi, after attending the 7th Solvay conference where the discovery of the  
<sup>41</sup> neutron as well as Pauli's neutrino were presented, proposed a new theory to explain  
<sup>42</sup> the  $\beta$  decay [103]. Fermi's theory defined the  $\beta$  decay as a process in which the neutron  
<sup>43</sup> decays to a proton, emitting an electron and a neutrino. Fermi formulated his theory  
<sup>44</sup> using an analogous approach as in Quantum Electrodynamics (QED) by proposing the  
<sup>45</sup> following lagrangian for  $\beta$  decay [104]:

$$L_\beta = G_F (\bar{u}_p \gamma_\mu u_n) (\bar{u}_e \gamma^\mu u_\nu) \quad (4.1)$$

<sup>46</sup> where  $u$  is the Dirac spinor of each particle,  $\gamma_\mu$  is the Dirac matrix and  $G_F$  is the Fermi  
<sup>47</sup> coupling constant. Fermi's theory of weak interactions assumed the same conservation  
<sup>48</sup> rules as QED, including the symmetry under reflection in space [104]. A system that is  
<sup>49</sup> invariant under reflections conserve a quantity called parity which includes an intrinsic  
<sup>50</sup> component called spin and a spatial component depending on the angular momentum of  
<sup>51</sup> the particle.

<sup>52</sup> In the upcoming years, the physicists Tsung Dao Lee and Chen Ning Yang started to  
<sup>53</sup> doubt the conservation of weak parity after not finding any experimental evidence so

54 far [105]. In an attempt to test the conservation of parity in weak interactions, Lee and  
55 Yang proposed in 1956 to study the  $\beta$  decays of Cobalt ( $^{60}\text{Co}$ ) and measure the projection  
56 of the momemtum of electrons along the spin axis of the Cobalt nucleus [105]. If the  
57 decay process conserves parity then electrons would be produced in all directions. The  
58 experiment to test the conservation of weak parity was realized by Chien-Shiung Wu in  
59 1957. The results of Wu's research showed that electrons were preferentially produced  
60 in the opposite direction to the Cobalt spin [106], which meant that parity was not  
61 conserved in weak interactions.

62 Apart from parity, one can also associate a helicity to particles. The particle's helicity  
63 is considered right-handed if the direction of the particle's momemtum and spin are the  
64 same, and left-handed otherwise. In 1958, Goldhaber, Grodzins and Sunyar measured  
65 the neutrino helicity at Brookhaven National Laboratory (BNL) and discovered that  
66 neutrinos were always left-handed and antineutrinos were right-handed [107]. As a  
67 consequence of the discovery of parity violation and the neutrino helicity, Robert Marshak  
68 and George Sudarshan modified Fermi's weak theory and introduced an axial vector  
69 term, giving rise to the V-A (vector-axial) theory of weak interactions [108]. Even though  
70 parity (P) and charge conjugation (C) (transforms particles into their antiparticles) were  
71 violated separately, it was assumed that the combined CP operation was still conserved  
72 by the weak force.

73 The assumption of the conservation of CP did not last long. An experiment performed  
74 at BNL by James Christenson, James Cronin, Val Fitch and Rene Turlay [109] in  
75 1964 concluded that the long-lived  $K_L$  meson (CP=-1) was able to decay to two pions  
76 (CP=+1) violating CP in the process. To explain the CP violation in weak theory, Makoto  
77 Kobayashi and Toshihide Maskawa [110] extended the formulation of the Cabibbo matrix  
78 to include three generation of quarks and a CP-violating phase term. The Cabibbo matrix  
79 was originally computed by Nicola Cabibbo [111] including four quarks to explain the  
80 different amplitudes observed between the up, down and strange quark transitions. The  
81 development of the Cabibbo, Kobayashi and Maskawa (CKM) matrix led to the prediction  
82 of the bottom and top quarks, discovered later in 1977 [112] and 1995 [113], respectively.

83 Following Paul Dirac's formulation of QED [114], Sheldon Glashow [115], Steven  
84 Weinberg [116] and Abdus Salam [117] managed in 1968 to build a gauge-invariant  
85 unified theory of the electromagnetic and weak interactions, for which they were awarded  
86 the Nobel Prize in Physics in 1979 [118]. In order to make the electroweak theory  
87 symmetric under local phase transformations, it required the presence of four spin-1  
88 massless bosons: two electricaly charged particles called  $W^\pm$  bosons and two neutral

89 particles corresponding to the Z boson and photon. But since weak interactions are short  
90 range, the weak force has to be mediated by massive bosons. The addition of mass to the  
91 bosons was realized after introducing the spontaneous local breaking of the underlying  
92 SU(2) symmetry through the Higgs mechanism [8, 9]. In the following years, Gerardus't  
93 Hooft and Martinus Veltman managed to renormalize the electroweak theory [119, 120],  
94 allowing to calculate more precisely the theoretical masses of the weak bosons.

95 The experimental study of weak bosons would require the development of new  
96 particle acceleration technologies. In 1976, Carlo Rubbia, Peter McIntyre and David  
97 Cline suggested to transform CERN's circular proton accelerator called Super Proton  
98 Synchrotron (SPS) into a proton-antiproton collider (Sp̄S) [121]. The upgrade to Sp̄S  
99 was made possible thanks to the stochastic cooling technology invented by Simon Van  
100 der Meer [122] in 1972, which allowed to cool down and collect antiprotons. Several  
101 experiments, named Underground Area (UA), were built to study the proton-antiproton  
102 collisions at the Sp̄S. The UA1 and UA2 collaborations discovered the W boson [123, 124]  
103 in 1983 after reporting the observation of electrons with large transverse energy and  
104 the presence of missing energy in p̄p collisions at  $\sqrt{s} = 540 \text{ GeV}$ . And few months later,  
105 both collaborations also reported the discovery of the Z boson in the dilepton decay  
106 channel [125, 126]. These outstanding discoveries convinced the Swedish Academy of  
107 Science to award in 1984 the Nobel Prize in Physics to Rubbia and Van der Meer for  
108 their contributions to the Sp̄S program [127].

109 After the major success of the Sp̄S project, CERN constructed in 1983 a new lep-  
110 ton circular collider called the Large Electron-Positron (LEP) collider [128]. LEP was  
111 designed to accelerate electrons and positrons to an energy of half the Z boson mass  
112 (45 GeV) in order to perform precision measurements of the Z boson lineshape. Fur-  
113 thermore, a precise measurements of the W mass [129] was later performed by the  
114 experiments in the Fermi National Accelerator Laboratory (FNAL). The FNAL analyzed  
115 data collected between 1983 and 2011 from the Tevatron [130], a proton-antiproton  
116 synchrotron collider that operated at energies up to 1 TeV.

117 The successful programs of LEP and Tevatron produced the most precise measure-  
118 ments of the properties of the electroweak theory, but there was still a missing piece  
119 to complete the picture, the Higgs boson. The discovery of the Higgs boson was finally  
120 achieved in 2012 by the CMS [10] and ATLAS [11] collaborations at the Large Hadron  
121 Collider (LHC).

---

### 122 4.1.2 Electroweak theory

123 The interactions between elementary particles mediated by the weak and electromagnetic  
 124 forces are described in the Standard Model using the electroweak theory developed by  
 125 Glashow, Weinberg and Salam [115–117]. The unification of these two fundamental  
 126 forces of nature is accomplished mathematically using a non-abelian  $SU(2) \times U(1)_Y$   
 127 gauge theory. The electroweak theory requires four massless gauge bosons: three bosons  
 128 with weak isospin (called  $W_1$ ,  $W_2$  and  $W_3$ ) from  $SU(2)$  and one boson (named  $B$ ) with  
 129 weak hypercharge from  $U(1)_Y$ .

130 Since weak bosons have mass, a full description of the electroweak interactions  
 131 requires the inclusion of massive vector bosons. The problem is that one can not naively  
 132 add a mass term of the form  $m^2 W^\mu W_\mu$  into the electroweak lagrangian since this would  
 133 break gauge invariance making the theory divergent. Thus, this issue is instead solved  
 134 by spontaneously breaking the  $SU(2) \times U(1)_Y$  electroweak symmetry into a  $U(1)_{EM}$   
 135 symmetry using the Higgs mechanism [8, 9]. The overall idea is that the electroweak  
 136 gauge bosons couple to a scalar field called the Higgs field which is present in all space.  
 137 When the Higgs field induces a spontaneous breaking of the gauge symmetry, the Higgs  
 138 field is splitted into one dynamic part corresponding to the Higgs boson, and another  
 139 constant part called the vacuum expectation value (VEV). The symmetry breaking of  
 140  $SU(2) \times U(1)_Y$  to  $U(1)_{em}$  generates three massless Goldstone bosons. The goldstone  
 141 bosons are then absorbed by the electroweak gauge bosons producing the  $W^+$ ,  $W^-$  and  $Z$   
 142 bosons with masses proportional to the VEV, while the photon remains massless. The  $W^\pm$ ,  
 143  $Z$  and  $\gamma$  bosons are correlated with the  $W_1$ ,  $W_2$ ,  $W_3$  and  $B$  gauge bosons in the following  
 144 way:

$$W^\pm = \frac{1}{\sqrt{2}}(W_1 \pm W_2) \\ \begin{pmatrix} Z \\ \gamma \end{pmatrix} = \begin{pmatrix} \cos\theta_W & \sin\theta_W \\ -\sin\theta_W & \cos\theta_W \end{pmatrix} \begin{pmatrix} B \\ W_3 \end{pmatrix} \quad (4.2)$$

145 where  $\theta_W$  represents the weak mixing angle. In addition, the quarks acquire mass  
 146 through the Yukawa interaction with the Higgs field. Since the quark weak eigenstates  
 147 are not the same as their mass eigenstates, weak interactions can induce a transition  
 148 from a up-like quark ( $u, c, t$ ) to a down-like quark ( $d, s, b$ ). The strength of the quark  
 149 flavour mixing in weak deacays is parameterized by the CKM matrix  $V_{CKM}$  via:

$$\begin{pmatrix} d' \\ s' \\ b' \end{pmatrix} = \begin{pmatrix} V_{ud} & V_{us} & V_{ub} \\ V_{cd} & V_{cs} & V_{cb} \\ V_{td} & V_{ts} & V_{tb} \end{pmatrix} \begin{pmatrix} d \\ s \\ b \end{pmatrix} \quad (4.3)$$

150 where  $(d', s', b')$  are the down-like quark weak eigenstates and  $(d, s, b)$  are the  
 151 corresponding mass eigenstates. The latest values of the CKM matrix elements are [12]:

$$V^{\text{CKM}} = \begin{pmatrix} 0.97417 & 0.2248 & 0.00409 \\ 0.220 & 0.995 & 0.0405 \\ 0.0082 & 0.04 & 1.009 \end{pmatrix} \quad (4.4)$$

152 The lagrangian of the electroweak theory includes several components that describes  
 153 the interactions between the fermions, electroweak bosons and the Higgs boson. In the  
 154 case of the Z boson, the term of the lagrangian that represents the interactions between  
 155 fermions and neutral charged electroweak bosons is:

$$L_{NC} = \alpha_{em} \theta_W \sum_{\text{fermions}} \bar{f} \gamma^\mu A_\mu f + \frac{g}{\cos \theta_W} \sum_{\text{fermions}} \bar{f} \gamma^\mu \frac{(g_v^f - g_a^f \gamma^5)}{2} Z_\mu f \quad (4.5)$$

156 where  $g$  is the coupling constant of  $SU(2)_L$ ,  $f$  is the Dirac spinors of fermions,  $A_\mu$   
 157 is the electromagnetic field, and  $g_v^f$  ( $g_a^f$ ) is the fermion vector (axial) weak coupling  
 158 constants. Eq. (4.5) specify that the Z bosons and photons conserve flavour always  
 159 decaying into a fermion and its corresponding antifermion. Even though photons do  
 160 not distinguish the helicity of particles, the Z boson couplings are different for left- and  
 161 right-handed fermions.

162 Furthermore, the component of the lagrangian that represents the interaction be-  
 163 tween the W bosons and the fermions is given by:

$$L_{CC} = \frac{g}{2\sqrt{2}} \left( (\bar{u}, \bar{c}, \bar{t})_R W_\mu^+ \gamma^\mu V^{\text{CKM}} \begin{pmatrix} d_L \\ s_L \\ b_L \end{pmatrix} + (\bar{\nu}_e, \bar{\nu}_\mu, \bar{\nu}_\tau)_R W_\mu^+ \gamma^\mu \begin{pmatrix} e_L^- \\ \mu_L^- \\ \tau_L^- \end{pmatrix} \right) \quad (4.6)$$

164 where  $f_L$  correspond to left-handed fermions and  $\bar{f}_R$  represents right-handed an-  
 165 tifermions. Thus, W bosons only couple to right-handed antifermions and left-handed  
 166 fermions organized in pairs of lepton-neutrino or quark-antiquark, where the electric  
 167 charge of the of particles differ by one unit. Since the top quark mass (178 GeV) is larger  
 168 than the W boson mass (80 GeV), the W boson can not decay to a top quark. Fig. 4.1

169 shows the possible decays of W bosons to fermions. The measured values of the mass,  
 170 width and couplings of weak vector bosons are summarized in Table 4.1.2.

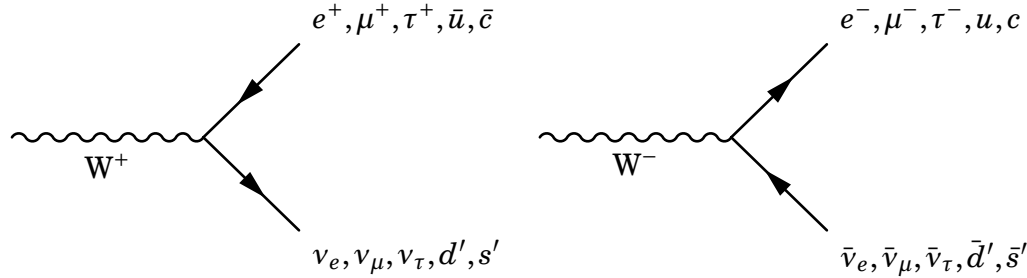


Figure 4.1: Feynman diagram of the decay modes of  $W^+$  (left) and  $W^-$  (right) bosons to fermions.

Variable	Description	Value
$M_W$	W boson mass	80.385(15) GeV
$\Gamma_W$	W boson width	2.085(42) GeV
$BR(W \rightarrow \ell\nu)$	Branching fraction of W boson semileptonic decays	$(10.86 \pm 0.09)\%$
$BR(W \rightarrow q\bar{q}')$	Branching fraction of W boson hadronic decays	$(67.41 \pm 0.27)\%$
$M_Z$	Z boson mass	91.1876(21) GeV
$\Gamma_Z$	Z boson width	2.4952(23) GeV
$BR(Z \rightarrow \ell^+\ell^-)$	Branching fraction of Z boson charged-lepton decays	$(3.3658 \pm 0.0023)\%$
$BR(Z \rightarrow \nu\bar{\nu})$	Branching fraction of Z boson neutrino decays	$(20.00 \pm 0.06)\%$
$BR(Z \rightarrow q\bar{q})$	Branching fraction of Z boson hadronic decays	$(69.91 \pm 0.06)\%$

Table 4.1: Experimental values of the mass, width and branching fractions of weak bosons extracted from the PDG [12].

### 171 4.1.3 Nuclear PDF

172 Beams of Pb ions composed of 82 protons and 126 neutrons are used at the LHC. In  
 173 proton-lead collisions, the PDF of the nucleons (i.e. neutrons and protons) is modified  
 174 by the presence of the nuclear environment of the Pb ion. The neutron PDF can be  
 175 derived from the proton PDF using isospin symmetry (i.e. by exchanging the up and  
 176 down quark PDFs), while assuming the same gluon PDF as in the proton. If no nuclear  
 177 modifications are expected, protons and neutrons should then behave as free particles  
 178 inside the nucleus, and one could simply sum the PDFs of the protons and neutrons  
 179 scaled accordingly. In this case, the ratio of the PDF of protons bounded in the nucleus  
 180 (nuclear PDF) over the free-proton PDF should be one.

181 To determine the nuclear modifications, the heavy ion measurements were first com-  
182 pared to results using deuterium. The European Muon Collaboration (EMC) measured  
183 the structure function of DIS in iron and deuterium targets between 1977 and 1988,  
184 and observed a depletion of the iron PDFs relative to the deuterium PDFs at  $x > 0.2$   
185 (EMC region) [131] and at  $x < 0.01$  (shadowing region) [132]. Subsequent results found  
186 an enhancement at the intermediate region  $0.01 < x < 0.2$  (antishadowing region) [133].  
187 Since current heavy ion data is more limited than data from proton collisions, the global  
188 fits of the nuclear PDFs are less accurate than the proton PDFs.

189 **4.1.4 PDF global fits**

190 The parton distribution functions can not be currently determined from first principles  
191 due to the nonperturbative behaviour of the strong interactions. Nevertheless, their  
192 dependence on  $x$  can be derived by fitting observables (e.g. structure functions or asym-  
193 metries) to experimental data from different processes since PDFs do not depend on the  
194 initial hard scattering. The  $Q^2$  dependence of the PDFs is determined using the DGLAP  
195 evolution equations. The most common processes used to constrain the PDFs correspond  
196 to Drell-Yan, DIS, vector boson and jet production, which have been measured by various  
197 experiments including data from HERA, SLAC and LHC.

198 There are several proton PDFs currently available. One of the most commonly used  
199 proton PDF in high energy physics nowadays is the one provided by the Collaboration  
200 of Theorists and Experimentalist (CTEQ). The most recent CTEQ PDF corresponds to  
201 CT14 published in 2016 [134]. The global fits of CT14 PDFs include data of vector bosons  
202 and jets from LHC pp collisions at 7 TeV and 8 TeV, charm quark DIS production from  
203 HERA, and electron charge asymmetry from Tevatron. The  $x$ -dependence of the CT14  
204 PDF is parameterized at low  $Q^2$  scale by [134]:

$$xf_a(x, Q^2) = x^{c_1}(1-x)^{c_2} P_a(x) \quad (4.7)$$

205 where  $P_a$  is a polynomial with different parameters for each parton. In the case of  
206 the up and down valence quarks,  $P_a$  is expressed as a Bernstein polynomial of fourth-  
207 order in  $\sqrt{x}$ . The  $P_a$  distribution of gluon and the light sea quark PDFs is given instead  
208 by a Bernstein polynomial in  $y = (2\sqrt{x} - x)$  of second-order and fourth-order, respectively.  
209 There is not enough data to constrain the strange quark and antiquark PDFs so they  
210 are assumed to be equal. In total, the CT14 PDFs are described by 26 fitting parameters

211 including: 8 parameters for the valence quarks, 5 parameters for the gluon and 13  
 212 parameters for the sea quarks [134].

213 The first global fit to describe leading-order nuclear effects was the EKS98 nPDF [135].  
 214 The pion data collected by RHIC was later included in EPS08 [136], EPS09 [137],  
 215 DSSZ [138] and nCTEQ15 [139] nPDFs which provided constraints to the gluon nPDF.  
 216 We will focus on the latest nuclear PDF calculations which are the EPPS16 [140] and  
 217 the nCTEQ15 [139] NLO nPDFs.

218 The EPPS16 nPDFs [140] are derived from a global analysis of nuclear data sets  
 219 published in 2017 by the group of Eskola, Paakkinen, Paukkunen and Salgado (EPPS).  
 220 The EPPS16 nPDF calculations update their previous EPS09 [137] global fits. EPPS16  
 221 includes five additional parameters compared to EPS09 to account for possible flavour  
 222 dependence of the quark nuclear modifications. The EPPS16 global fits includes the  
 223 same data sets as EPS09 (charged-lepton-nucleus DIS data from SLAC, DY dilepton  
 224 production from EMC proton-nucleus collisions and inclusive pion production from RHIC  
 225 deuteron-nucleus collisions), as well as the CHORUS neutrino-nucleus DIS data, low-  
 226 mass DY production from RHIC pion-nucleus collisions, and the results using dijet and  
 227 electroweak boson production in LHC pPb collisions at  $\sqrt{s_{\text{NN}}} = 5.02 \text{ TeV}$ . The addition  
 228 of the new LHC, RHIC and CHORUS data into the global fit is not in tension with  
 229 the previous EPS09 data sets, reassuring the validity of the universality of the nPDFs.  
 230 Moreover, the inclusion of the CMS measurements of dijet production in pPb collisions  
 231 at  $\sqrt{s_{\text{NN}}} = 5.02 \text{ TeV}$  highly constrained the gluon nPDF. On the other hand, the LHC  
 232 measurements of the electroweak boson production in pPb data was not able to further  
 233 constrain the quark nPDF due to the limited statistical precision. The nuclear PDFs are  
 234 parameterized in EPPS16 as:

$$f_i^{p/A}(x, Q^2) = R_i^A(x, Q^2) f_i^p(x, Q^2) \quad (4.8)$$

235 where  $f_i^{p/A}$  represents the PDF of a proton bounded in a nucleus A,  $f_i^p$  is the free  
 236 proton PDF and  $R_i^A$  is the corresponding nuclear modification. The EPPS16 nuclear  
 237 modifications are derived using the NLO CT14 PDF as the free proton baseline. The  
 238 parameters of  $R_i^A$  are determined in three regions: the shadowing region  $x \rightarrow 0$ , the  
 239 antishadowing maximum point  $x_a$  and the EMC minimum point  $x_e$ . The dependence on  
 240 the atomic mass A is parameterized along the three x regions in the following way:

$$R_i^A(x, Q_0^2) = R_i^{A_{\text{ref}}}(x, Q_0^2) \left( \frac{A}{A_{\text{ref}}} \right)^{\gamma_i [R_i^{A_{\text{ref}}}(x, Q_0^2) - 1]} \quad (4.9)$$

where  $Q_0$  is the parameterization scale fixed at the charm pole mass (1.3 GeV),  $\gamma_i$  is a positive parameter and  $A_{\text{ref}} = 12$ . The  $Q^2$  dependence above  $Q_0^2$  is determined by solving the DGLAP parton evolution equations. The strong coupling constant evaluated at the Z boson mass is set to  $\alpha_s(M_Z) = 0.118$ . The EPPS16 nuclear modifications are parameterized in total by 20 parameters.

The nCTEQ15 nuclear PDF published by Kovarik et al. in 2016 was derived using the CTEQ framework at next-to-leading order. The nCTEQ15 nPDF global fits make use of charged-lepton DIS data, DY dilepton production and RHIC inclusive pion production. In contrast with EPPS16 where the nuclear modification factor  $R_i^{p/A}$  is fitted, the nCTEQ15 global analysis parametrizes the nuclear PDF  $f_i^{p/A}$  directly (i.e. no free proton PDF is used as baseline). The nCTEQ nPDFs are parameterized as:

$$\begin{aligned}
 xf_i^{p/A}(x, Q_0) &= c_0 x^{c_1} (1-x)^{c_2} e^{c_3 x} (1+e^{x_4 x})^{c_5} \\
 \frac{\bar{d}(x, Q_0)}{\bar{u}(x, Q_0)} &= c_0 x^{c_1} (1-x)^{c_2} + (1+c_3 x)(1-x)^{c_4} \\
 s^{p/A}(x, Q_0) &= \bar{s}^{p/A}(x, Q_0) = \frac{\kappa(A)}{2} (\bar{u}^{p/A}(x, Q_0) + \bar{d}^{p/A}(x, Q_0))
 \end{aligned} \tag{4.10}$$

where  $f_i^{p/A}$  is defined for  $i = (u_v, d_v, g, \bar{u} + \bar{d}, s + \bar{s}, s - \bar{s})$ ,  $\kappa(A) = \left( c_{0,0}^{s+\bar{s}} + c_{0,1}^{s+\bar{s}} (1-A^{-c_{0,2}}) \right)$  and the parameterization scale  $Q_0 = 1.3$  GeV. The A-dependence of the nCTEQ15 nPDF is parameterized directly in the coefficients using  $c_k(A) = c_{k,0} + c_{k,1}(1-A^{-c_{k,2}})$ , where  $k = 1, \dots, 5$ .

The nCTEQ15 global fits to the data sets are performed by minimizing the  $\chi^2$ . The nCTEQ15 fits are performed using 16 free parameters separated in: 7 gluon, 4 up valence quark, 3 down valence quark and 2 ( $d+u$ ) antiquark parameters. Also, nCTEQ15 treat the light valence quark densities independently but it assume no flavour dependence of the light antiquark nuclear modifications. The nCTEQ15 calculations avoid fitting the low  $Q^2$  and high  $x$  region  $x > 0.7$  since this region is very difficult to model theoretically due to the presence of target mass corrections, large  $x$  resummation, nuclear off-shell effects and Fermi motion effects which steeply rise the parton densities when approaching  $x = 1$ .

The PDF uncertainties are determined using the Hessian matrix approach. The main idea of the Hessian method is that the distribution of the  $\chi^2(\{a_i\})$  around its minimum  $\chi^2(\{a_i^0\})$  can be approximately parameterized by a quadratic function of the  $n$  fitting parameters  $\{a_i\}$  as  $\chi^2(\{a_i\}) \approx \chi^2(\{a_i^0\}) \sum_{i,j} y_i H_{i,j} y_j$  where  $y_i = a_i - a_i^0$  and  $H_{i,j} = (1/2) (d^2 \chi^2 / dy_i dy_j)_{a_i=a_i^0}$  is the Hessian matrix that encodes the impact of variations around each parameter. Since  $H_{i,j}$  is a symmetric matrix, it has  $n$  orthogonal eigenvectors. The eigenvectors of  $H_{i,j}$  are used to define a new basis  $\{z_k\}$  which transform  $H$  into a

271 diagonal matrix. In order to compute the PDF uncertainties, the EPPS16 and nCTEQ15  
 272 calculations provide the PDF central set  $S_0$  and the PDF error sets  $S_k^\pm$  defined in the  $\{z_k\}$   
 273 coordinates. Each  $S_k^\pm$  is determined by evaluating the PDF on  $\{z_k^\pm\}$  defined by varying  
 274 upward/downward the parameter  $\{z_k\}$  along the k-th eigenvector direction as:

$$S_k^\pm = f \left( z_k^0 \pm \sqrt{\frac{\Delta\chi^2}{\lambda_k}} \right) \quad (4.11)$$

275 where  $\lambda_k$  is the k-th eigenvalue of  $H$  and  $\Delta\chi^2$  is the tolerance criterion defined at  
 276 90% confidence limit. In nCTEQ15 the tolerance is set to  $\Delta\chi^2 = 35$  while in EPPS16 it is  
 277 set to  $\Delta\chi^2 = ??$ . Using the PDF error sets, the PDF uncertainties can then be defined as:

$$\Delta O = \sqrt{\sum_i^{\max} [\min \{O(S_i^+) - O(S_i^0), O(S_i^-) - O(S_i^0), 0\}]^2} \quad (4.12)$$

278 To derive the correlation between two observables  $X$  and  $Y$ , one can use the cosine of  
 279 the correlation angle define as:

$$\cos\phi[X, Y] = \frac{\sum_{i_{\text{PDF}}} (X_{i_{\text{PDF}}}^+ - X_{i_{\text{PDF}}}^-)}{(Y_{i_{\text{PDF}}}^+ - Y_{i_{\text{PDF}}}^-)} \sqrt{\sum_{j_{\text{PDF}}} (X_{j_{\text{PDF}}}^+ - X_{j_{\text{PDF}}}^-)^2} \sqrt{\sum_{k_{\text{PDF}}} (Y_{k_{\text{PDF}}}^+ - Y_{k_{\text{PDF}}}^-)^2} \quad (4.13)$$

280 where the observables are calculated over the upward/downward PDF error sets in  
 281 each eigenvector direction (16 for nCTEQ15 and 20 for EPPS16). The main differences  
 282 between the EPS09, EPPS16 and nCTEQ15 nuclear PDFs are summarized in Table 4.1.4.

### 283 4.1.5 Production of W bosons at LHC

284 The production of W bosons in hadronic collisions is accomplished through the process of  
 285 quark-antiquark annihilation. The measurement of W boson production in pPb collisions  
 286 at  $\sqrt{s_{\text{NN}}} = 8.16 \text{ TeV}$  is performed in the semimuonic decay channel. At leading order (LO),  
 287 the W boson hadroproduction to final state leptons is described by the Feynman diagram  
 288 shown in Fig. 4.2.

289 In this thesis, the cross section of the W boson production is measured in pPb  
 290 collisions as a function of muon pseudorapidity ( $\eta$ ) considering muons with  $p_T$  larger  
 291 than 25 GeV/c. The theoretical cross section can be derived using electroweak theory and  
 292 the factorization theorem shown in Eq. (1.6). The W boson hadroproduction cross section  
 293 has been calculated in Ref. [141], and the corresponding pPb LO differential cross section  
 294 as a function of muon  $\eta$ , considering  $\Gamma_W \ll M_W$ , is:

nPDF	EPS09	EPPS16	nCTEQ15
Order	NLO	NLO	NLO
Fit	nuclear modification	nuclear modification	nuclear PDF
Baseline PDF	CT14	CTEQ6	
Free parameters	15	20	17
Data points	929	1811	708
EMC DY dileptons in p-A	Yes	Yes	Yes
RHIC pions in d-A	Yes	Yes	Yes
SLAC $l^\pm$ -A DIS	Yes	Yes	Yes
CHORUS $\nu$ -A DIS	No	Yes	No
RHIC DY in $\pi$ -A	No	Yes	No
LHC dijets in pPb	No	Yes	No
LHC weak bosons in pPb	No	Yes	No

Table 4.2: Summary of the information of EPS09, EPPS16 and nCTEQ15 nuclear PDFs.

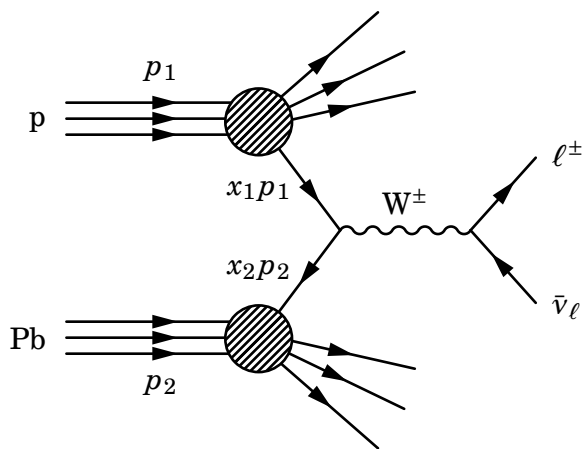


Figure 4.2: Feynman diagram of LO W boson production to final state leptons in pPb collisions

$$\begin{aligned}
 \frac{d\sigma^{W^\pm}}{d\eta}(s_{NN}) \approx & \frac{\pi^2}{6M_W^5\Gamma_W} \left( \frac{\alpha_{em}}{\sin^2(\theta_W)} \right)^2 \int_{25}^{\inf} dp_T \frac{p_T^3}{\sqrt{1-4p_T^2/M_W^2}} \sum_{i,j} \delta(e_{q_i} + e_{\bar{q}_j}, \pm 1) |V_{ij}^{\text{CKM}}|^2 \\
 & \left\{ x_p^\pm q_i^p(x_p^+, Q^2) \cdot x_{\text{Pb}}^\mp \bar{q}_j^{\text{Pb}}(x_{\text{Pb}}^+, Q^2) + x_p^\pm \bar{q}_i^p(x_p^-, Q^2) \cdot x_{\text{Pb}}^\mp q_j^{\text{Pb}}(x_{\text{Pb}}^-, Q^2) + \right. \\
 & \left. x_p^\mp q_i^p(x_p^-, Q^2) \cdot x_{\text{Pb}}^\pm \bar{q}_j^{\text{Pb}}(x_{\text{Pb}}^-, Q^2) + x_p^\mp \bar{q}_i^p(x_p^+, Q^2) \cdot x_{\text{Pb}}^\pm q_j^{\text{Pb}}(x_{\text{Pb}}^+, Q^2) \right\}
 \end{aligned} \tag{4.14}$$

where  $\alpha_{em}$  is the fine-structure constant,  $q^p$  is the free-proton quark PDF,  $q_i^{\text{Pb}}$  is the Pb nuclear quark PDF, and  $Q \approx M_W$  is the momentum scale. The sum in Eq. (4.14) is performed over all quark flavours and the parton momemtum fraction variables  $x_p$  and  $x_{\text{Pb}}$  are defined as [141]:

$$\begin{aligned}
 x_p^\pm &= \frac{M_W}{\sqrt{s_{NN}}} e^\eta \left[ \frac{1 \mp \sqrt{1-4p_T^2/M_W^2}}{2p_T/M_W} \right] \\
 x_{\text{Pb}}^\pm &= \frac{M_W}{\sqrt{s_{NN}}} e^{-\eta} \left[ \frac{1 \pm \sqrt{1-4p_T^2/M_W^2}}{2p_T/M_W} \right]
 \end{aligned} \tag{4.15}$$

The cross sections of negative and positive charged leptons, shown in Eq. (4.14), are different due to parity violation and helicity conservation of weak decays. Since  $W^+$  bosons couple to right-handed leptons while  $W^-$  couples to left-handed leptons, leptons are produced in the same direction as the  $W$  boson while antileptons are generated in the opposite direction. This is reflected in Eq. (4.15) where  $\mu^-$  production is sensitive to slightly higher  $x$  than  $\mu^+$  production.

Multiple proton-proton and proton-neutron hard scatterings takes place during pPb collisions. In this case, the  $W$  bosons are mainly produced from interactions between the valence quarks and sea antiquarks of the nucleons. The dominant production modes of  $W^+$  bosons correspond to up quark and down antiquark annihilation while for  $W^-$  bosons correspond to down quark and up antiquark annihilation. The annihilation between light quarks and heavier antiquarks is also possible but highly suppressed according to the CKM matrix elements. Therefore, the inclusive  $W$  boson cross section measured in pPb data is mostly sensitive to the proton and Pb-nucleus PDFs of light quarks and antiquarks.

In addition, the  $W$  boson cross sections can be compared between different beam energies. According to Arleo, Chapon and Paukkunen [141], at small enough  $x$  values, the

316 W boson cross section follows a power-like scaling as a function of  $s_{\text{NN}}$ , where Eq. (4.14)  
 317 can be approximately reduced to:

$$\frac{d\sigma^{W^\pm}}{d\eta}(s_{\text{NN}}, \xi_p) \approx (s_{\text{NN}})^\alpha \times F_{p,\text{Pb}}^\pm(\xi_p, p_T), \quad \eta \gg 0, \quad (4.16)$$

$$\frac{d\sigma^{W^\pm}}{d\eta}(s_{\text{NN}}, \xi_{\text{Pb}}) \approx (s_{\text{NN}})^\alpha \times G_{p,\text{Pb}}^\pm(\xi_{\text{Pb}}, p_T), \quad \eta \ll 0$$

318 where  $\alpha$  is the scaling parameter, and  $\xi_p = (M_W / \sqrt{s_{\text{NN}}}) e^{-\eta}$  and  $\xi_{\text{Pb}} = (M_W / \sqrt{s_{\text{NN}}}) e^\eta$   
 319 are the x values at  $p_T = M_W/2$  in the proton and Pb ion, respectively. Moreover, the  
 320 functions  $F_{p,\text{Pb}}^\pm$  and  $G_{p,\text{Pb}}^\pm$  do not depend explicitly on  $s$  or  $\eta$ .

321 Furthermore, since the scaling parameter does not depend on the lepton pseudorapidity  
 322 or the charge of the W boson, the dependence on  $s_{\text{NN}}$  cancels in ratios of W boson  
 323 cross sections. We can then measure asymmetries to improve the sensitivity to different  
 324 aspects of the W boson production. Two of the most commonly used are the lepton charge  
 325 asymmetry defined in Eq. (4.18) and the forward-backward ratio presented in Eq. (4.20).  
 326 Thus, according to Eq. (4.16), the W boson asymmetries only depends on  $\xi_p$  and  $\xi_{\text{Pb}}$  for  
 327  $|\eta| \gg 0.5 \ln(s_{\text{NN}}/M_W^2)$ .

328 **4.2 W boson production in pPb collisions at**

329  $\sqrt{s_{\text{NN}}} = 8.16 \text{ TeV}$

330 This section presents the results of the analysis of the production of W bosons in pPb  
 331 collisions at  $\sqrt{s_{\text{NN}}} = 8.16 \text{ TeV}$  performed in the semi-muonic decay channel, using a  
 332 data sample with integrated luminosity of  $173.4 \pm 5.9 \text{ nb}^{-1}$  [142]. The W boson yields  
 333 are extracted in the muon kinematic region defined by  $p_T^\mu > 25 \text{ GeV}/c$  and  $|\eta_{\text{lab}}^\mu| < 2.4$ .  
 334 The W boson differential cross sections, the muon charge asymmetry, and the muon  
 335 forward-backward ratios are measured as a function of muon  $\eta_{\text{CM}}$ . The measurements  
 336 are compared to PDF calculations both without and with including nuclear modifications,  
 337 and also to results from other LHC experiments.

338 **4.2.1 Observables**

339 **4.2.1.1 W boson cross sections**

340 The differential  $W \rightarrow \mu\nu_\mu$  cross sections are calculated by dividing the efficiency-corrected  
 341  $W \rightarrow \mu\nu_\mu$  yields ( $N_{\text{corr}}$ ) over the recorded integrated luminosity (L) times the bin width  
 342 ( $\Delta\eta_{\text{CM}}$ ), as described below:

$$\frac{d\sigma^\pm}{d\eta_{\text{CM}}}(\eta_{\text{CM}}) = \frac{N_{\text{corr}}^\pm(\eta_{\text{CM}})}{\Delta\eta_{\text{CM}} L} \quad (4.17)$$

343 The results of the production cross sections for  $W^+ \rightarrow \mu^+\nu_\mu$  and  $W^- \rightarrow \mu^-\bar{\nu}_\mu$ , as  
 344 a function muon  $\eta_{\text{CM}}$ , are shown in Fig. 4.3. The vertical error bars represent the  
 345 statistical uncertainties from the measured  $W \rightarrow \mu\nu_\mu$  yields, while the brackets show  
 346 the statistical and total systematic uncertainties summed in quadrature. The global  
 347 integrated luminosity uncertainty of  $\pm 3.4\%$  [142] is not shown.

348 The opposite trend seen between the  $W^+$  and  $W^-$  boson differential cross sections is  
 349 expected from parity violation of the electroweak interaction. The  $W^+$  bosons decay to a  
 350 right-handed antimuon boosted in the opposite direction, while the  $W^-$  bosons decay to a  
 351 left-handed muon along the direction of the  $W^-$  boson. As a consequence, the  $\mu^+$  and  $\mu^-$   
 352 yields differ as a function of the muon  $\eta_{\text{CM}}$ .

353 **4.2.1.2 Muon charge asymmetry**

354 The muon charge asymmetry ( $C_\mu$ ) between  $W^- \rightarrow \mu^-\bar{\nu}_\mu$  and  $W^+ \rightarrow \mu^+\nu_\mu$  processes and  
 355 its corresponding uncertainty are defined in Eq. (4.18) and Eq. (4.19), respectively.

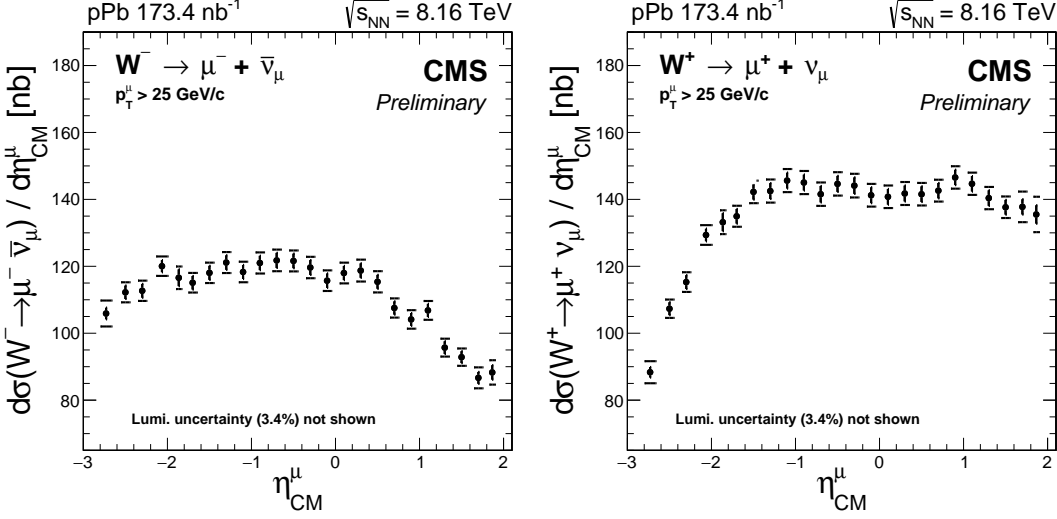


Figure 4.3: Production cross sections for  $W^+ \rightarrow \mu^+ \nu_\mu$  (left) and  $W^- \rightarrow \mu^- \bar{\nu}_\mu$  (right), as a function of the muon pseudorapidity in the center-of-mass frame. The brackets represent the statistical and systematic uncertainties summed in quadrature, while the error bars show the statistical uncertainties only. The global luminosity uncertainty of  $\pm 3.4\%$  [142] is not shown.

$$C_\mu(\eta_{CM}) = \frac{N_{corr}^+(\eta_{CM}) - N_{corr}^-(\eta_{CM})}{N_{corr}^+(\eta_{CM}) + N_{corr}^-(\eta_{CM})} \quad (4.18)$$

$$\delta C_\mu(\eta_{CM}) = \left( \frac{2 \times N_{corr}^+(\eta_{CM}) \times N_{corr}^-(\eta_{CM})}{(N_{corr}^+(\eta_{CM}) + N_{corr}^-(\eta_{CM}))^2} \right) \times \sqrt{\left( \frac{\delta N_{corr}^+(\eta_{CM})}{N_{corr}^+(\eta_{CM})} \right)^2 + \left( \frac{\delta N_{corr}^-(\eta_{CM})}{N_{corr}^-(\eta_{CM})} \right)^2} \quad (4.19)$$

356     The uncertainties correlated in muon charge, such as the integrated luminosity  
 357     uncertainty of 3.4% and the systematic components of the tag-and-probe correction  
 358     uncertainties (<2.8%), cancel in the measurement of the muon charge asymmetry. The  
 359     measured muon charge asymmetry is shown in Fig. 4.4 as a function muon  $\eta_{CM}$ .

360     **4.2.1.3 Muon forward-backward ratios**

361     The muon forward-backward ratio ( $R_{FB}$ ) is defined as the ratio of the  $W \rightarrow \mu \nu_\mu$  yields  
 362     extracted in the forward  $\eta_{CM}$  bin divided by its backward counterpart. By convention,  
 363     the forward region corresponds to the proton-going direction while the backward region  
 364     corresponds to the Pb-going direction. The muon forward-backward ratio is measured  
 365     for each muon charge separately, and also considering all muons. The  $R_{FB}$  is defined in  
 366     Eq. (4.20) and its uncertainty is computed using Eq. (4.21).

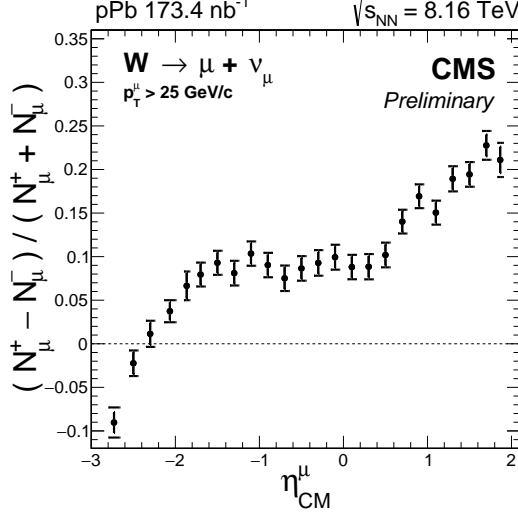


Figure 4.4: Muon charge asymmetry as a function of the muon pseudorapidity in the center-of-mass frame. The brackets represent the statistical and systematic uncertainties summed in quadrature, while the error bars show the statistical uncertainties only.

$$R_{FB}(\eta) = \frac{N_{corr}(+\eta_{CM})}{N_{corr}(-\eta_{CM})} \quad (4.20)$$

$$\delta R_{FB}(\eta_{CM}) = R_{FB}(\eta_{CM}) \times \sqrt{\left( \frac{\delta N_{corr}(+\eta_{CM})}{N_{corr}(+\eta_{CM})} \right)^2 + \left( \frac{\delta N_{corr}(-\eta_{CM})}{N_{corr}(-\eta_{CM})} \right)^2} \quad (4.21)$$

367 The results of the forward-backward ratio of all muons and the ratio for  $W^- \rightarrow$   
 368  $\mu^- \bar{\nu}_\mu$  and  $W^+ \rightarrow \mu^+ \nu_\mu$  decays, are shown in Fig. 4.5. The uncertainties correlated in  
 369 muon pseudorapidity, such as the integrated luminosity uncertainty of 3.4%, the event  
 370 activity reweighing uncertainty and the systematic uncertainties due to the electroweak  
 371 backgrounds, are strongly reduced.

### 372 4.2.2 Comparison with theoretical models

373 The measurements of the W boson production in pPb collisions at  $\sqrt{s_{NN}} = 8.16 \text{ TeV}$   
 374 are compared to three NLO PDF calculations, one assuming no nuclear effects (CT14  
 375 PDF [134]) and two including nuclear modifications (CT14+EPPS16 nPDF [140] and  
 376 CT14+nCTEQ15 nPDF [139]). The NLO PDF calculations are produced using the parton-  
 377 level Monte Carlo program MCFM [143]. The comparison between the PDF calculations  
 378 and the data are shown in Fig. 4.6 for the W differential cross sections, in Fig. 4.7 for the  
 379 muon charge asymmetry and in Fig. 4.8 for the muon forward backward ratios. In all

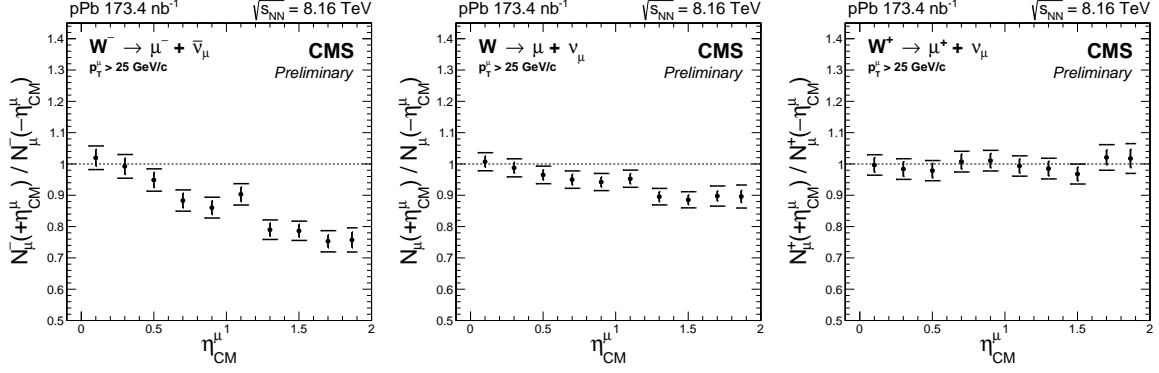


Figure 4.5: Forward-backward ratios, for the positive (left), all (middle) and negative (right) charged muons. The brackets represent the statistical and systematic uncertainties summed in quadrature, while the error bars show the statistical uncertainties only.

cases, the PDF calculations with (without) including nuclear modifications are displayed using dashed (continuous) lines and the corresponding PDF uncertainties are shown using hatched (filled) boxes.

As can be seen in Fig. 4.6, the W cross section measurements at forward rapidity favor the PDF calculations including nuclear modifications, while at backward rapidity all three PDF calculations are in good agreement with the data. Moreover, in the case of the muon charge asymmetry shown in Fig. 4.7, the results of the theory calculations derived using CT14 PDF only, and those including nuclear modifications described by EPPS16 nPDF, are in good agreement with the measurements while the CT14+nCTEQ15 nPDF calculations expect a slightly larger muon charge asymmetry in the most backward  $\eta_{CM}$  bins. Finally, from the ratios of muon yields at forward over backward  $\eta_{CM}$  displayed in Fig. 4.8, the nuclear PDF calculations describe much better the data compared to the free-nucleon PDF calculation. Considering the smaller size of the uncertainties compared to the theory uncertainties, the measurements have the potential to constrain the CT14+EPPS16 and the CT14+nCTEQ15 nPDF models.

In order to quantify the level of agreement between each PDF calculation and the measurements of the W boson production in pPb, a  $\chi^2$  test is performed. The  $\chi^2$  test is derived as described below:

$$\chi^2 = \sum_i \sum_j \left[ (t(i) - d(i)) (cov_{data} + cov_{theory})^{-1} [i, j] (t(j) - d(j)) \right] \quad (4.22)$$

where  $t(i)$  is the value of the observable predicted from the PDF calculation in bin i,

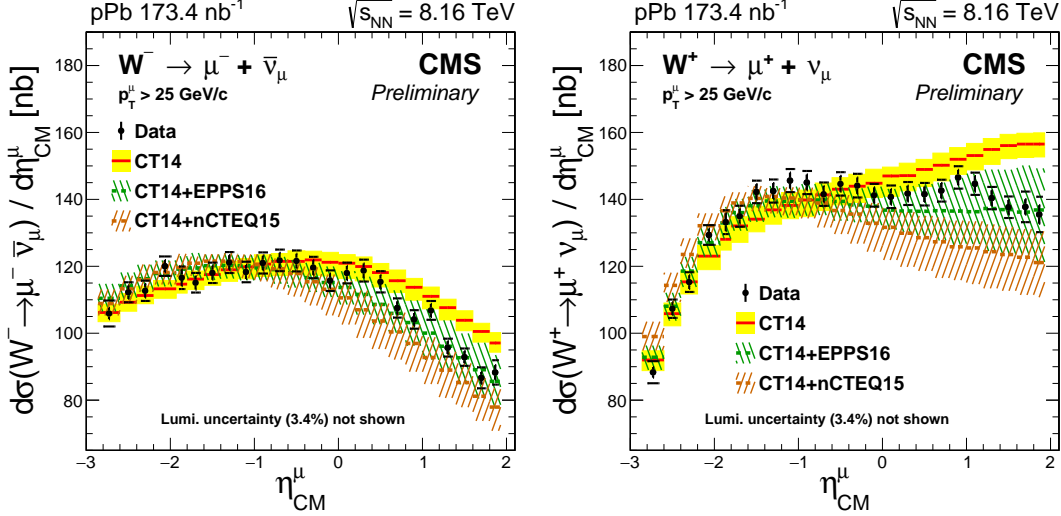


Figure 4.6: Differential cross sections for  $W^+ \rightarrow \mu^+ \nu_\mu$  (left) and  $W^- \rightarrow \mu^- \bar{\nu}_\mu$  (right), as a function of the muon pseudorapidity in the center-of-mass frame. Errors bars represent the statistical uncertainties, while the brackets represent the statistical and systematic uncertainties summed in quadrature. The global luminosity uncertainty of  $\pm 3.4\%$  is not displayed. Theoretical predictions with (CT14+EPPS16 shown in dashed green line and CT14+nCTEQ15 shown in dashed brown line) and without (CT14, solid red line) PDF nuclear modifications are also shown, with the uncertainty bands. All theory uncertainty bands include PDF uncertainties.

399  $d(i)$  is the value of the observable measured in data in bin  $i$ , and  $(cov_{data} + cov_{theory})^{-1}$   
 400 is the inverse of the sum of the covariance matrices extracted from the data and the  
 401 model. This approach takes into account the bin-to-bin correlations in both muon charge  
 402 and pseudorapidity. The outcome of the  $\chi^2$  statistical test derived using the CT14 PDF,  
 403 the CT14+EPPS16 nPDF and the CT14+nCTEQ15 nPDF calculations are summarized  
 404 in Table 4.3.

405 **4.2.3 Comparison with other LHC experiments**

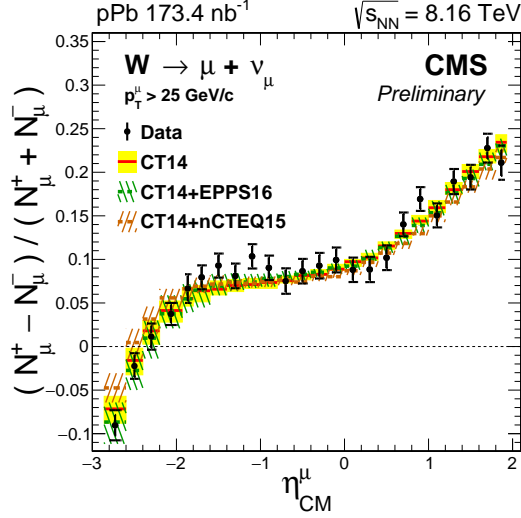


Figure 4.7: Muon charge asymmetry of  $W \rightarrow \mu\nu_\mu$ , given for each muon  $\eta_{CM}$  bin. Errors bars represent the statistical uncertainties, while the brackets represent the statistical and systematic uncertainties summed in quadrature. Theoretical predictions with (CT14+EPPS16 shown in dashed green line and CT14+nCTEQ15 shown in dashed brown line) and without (CT14, solid red line) PDF nuclear modifications are also shown, with the uncertainty bands. All theory uncertainty bands include PDF uncertainties.

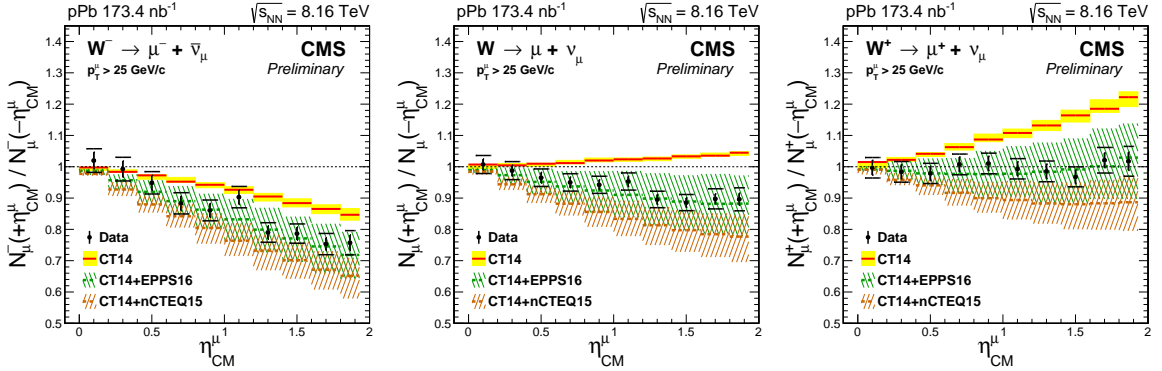


Figure 4.8: Forward-backward ratio of  $W \rightarrow \mu\nu_\mu$ , given for each muon  $\eta_{CM}$  bin separated in negative (left), all (middle) and positive (right) charged muons. Errors bars represent the statistical uncertainties, while the brackets represent the statistical and systematic uncertainties summed in quadrature. Theoretical predictions with (CT14+EPPS16 shown in dashed green line and CT14+nCTEQ15 shown in dashed brown line) and without (CT14, solid red line) PDF nuclear modifications are also shown, with the uncertainty bands. All theory uncertainty bands include PDF uncertainties.

---

 4.2. W BOSON PRODUCTION IN PPB COLLISIONS AT  $\sqrt{s_{\text{NN}}} = 8.16 \text{ TeV}$ 


---

Observable	CT14			CT14+EPPS16			CT14+nCTEQ15		
	$\chi^2$	ndf	Prob.(%)	$\chi^2$	ndf	Prob.(%)	$\chi^2$	ndf	Prob.(%)
$d\sigma(W \rightarrow \mu\nu_\mu)/d\eta_{CM}^\mu$	136	48	0	32	48	96	40	48	79
$(N_\mu^+ - N_\mu^-)/(N_\mu^+ + N_\mu^-)$	23	24	54	18	24	80	29	24	23
$N_\mu^\pm(+\eta_{CM}^\mu)/N_\mu^\pm(-\eta_{CM}^\mu)$	98	20	0	11	20	95	14	20	83
$N_\mu(+\eta_{CM}^\mu)/N_\mu(-\eta_{CM}^\mu)$	87	10	0	3	10	99	5	10	90

Table 4.3: Results of the  $\chi^2$  statistical test between the measurements and the theory calculations from the CT14 PDF, CT14+EPPS16 nPDF and CT14+nCTEQ15 nPDF models. The value of the  $\chi^2$ , the number of degrees of freedom (ndf) and the  $\chi^2$  probability (Prob.), are presented for the W differential cross sections, the muon charge asymmetry, the charged muon forward-backward ratios, and the forward-backward ratio of all muons, respectively.



C H A P T E R



## CONCLUSION



## BIBLIOGRAPHY

- [1] E. Fermi, “Sulla quantizzazione del gas perfetto monoatomico”, *Rendiconti Lincei* **3** (1926) 145. [[Cited on page 3.](#)]
- [2] P. A. M. Dirac, “On the theory of quantum mechanics”, *Proceedings of the Royal Society of London A: Mathematical, Physical and Engineering Sciences* **112** (1926) 661,  
<http://rspa.royalsocietypublishing.org/content/112/762/661.full.pdf>.  
[[Cited on page 3.](#)]
- [3] W. Pauli, “Über den Zusammenhang des Abschlusses der Elektronengruppen im Atom mit der Komplexstruktur der Spektren”, *Zeitschrift für Physik* **31** (1925) 765. [[Cited on page 3.](#)]
- [4] S. N. Bose, “Plancks Gesetz und Lichtquantenhypothese”, *Zeitschrift für Physik* **26** (1924) 178. [[Cited on page 4.](#)]
- [5] A. Einstein, “Quantentheorie des einatomigen idealen Gases”, *Sitzungber. Kgl. Akad. Wiss.*, 1924 261. [[Cited on page 4.](#)]
- [6] **Belle** Collaboration, A. Bondar *et al.*, “Observation of two charged bottomonium-like resonances in Y(5S) decays”, *Phys. Rev. Lett.* **108** (2012) 122001, arXiv:1110.2251. [[Cited on page 4.](#)]
- [7] **LHCb** Collaboration, R. Aaij *et al.*, “Observation of  $J/\psi p$  Resonances Consistent with Pentaquark States in  $\Lambda_b^0 \rightarrow J/\psi K^- p$  Decays”, *Phys. Rev. Lett.* **115** (2015) 072001, arXiv:1507.03414. [[Cited on page 4.](#)]
- [8] P. W. Higgs, “Broken Symmetries and the Masses of Gauge Bosons”, *Phys. Rev. Lett.* **13** (1964) 367. [[Cited on pages 5, 68, and 69.](#)]
- [9] F. Englert and R. Brout, “Broken Symmetry and the Mass of Gauge Vector Mesons”, *Phys. Rev. Lett.* **13** (1964) 321. [[Cited on pages 5, 68, and 69.](#)]

## BIBLIOGRAPHY

---

- [10] **CMS** Collaboration, S. Chatrchyan *et al.*, “Observation of a new boson at a mass of 125 GeV with the CMS experiment at the LHC”, *Phys. Lett. B* **716** (2012) 30, arXiv:1207.7235. [[Cited on pages 5 and 68.](#)]
- [11] **ATLAS** Collaboration, G. Aad *et al.*, “Observation of a new particle in the search for the Standard Model Higgs boson with the ATLAS detector at the LHC”, *Phys. Lett. B* **716** (2012) 1, arXiv:1207.7214. [[Cited on pages 5 and 68.](#)]
- [12] **Particle Data Group** Collaboration, C. Patrignani *et al.*, “Review of Particle Physics”, *Chin. Phys. C* **40** (2016), no. 10, 100001. [[Cited on pages 5, 7, 8, 70, 71, 103, and 105.](#)]
- [13] M. Gell-Mann, “The Eightfold Way: A Theory of strong interaction symmetry”, 1961. [[Cited on page 5.](#)]
- [14] Y. Ne’eman, “Derivation of strong interactions from a gauge invariance”, *Nucl. Phys.* **26** (1961) 222, [,34(1961)]. [[Cited on page 5.](#)]
- [15] M. Gell-Mann, “A Schematic Model of Baryons and Mesons”, *Phys. Lett.* **8** (1964) 214. [[Cited on page 6.](#)]
- [16] G. Zweig, “An SU(3) model for strong interaction symmetry and its breaking. Version 2”, in “DEVELOPMENTS IN THE QUARK THEORY OF HADRONS. VOL. 1. 1964 - 1978”, D. Lichtenberg and S. P. Rosen, eds., p. 22. 1964. [[Cited on page 6.](#)]
- [17] O. W. Greenberg, “Spin and Unitary Spin Independence in a Paraquark Model of Baryons and Mesons”, *Phys. Rev. Lett.* **13** (1964) 598. [[Cited on page 6.](#)]
- [18] H. Fritzsch, M. Gell-Mann, and H. Leutwyler, “Advantages of the Color Octet Gluon Picture”, *Phys. Lett. B* **47** (1973) 365. [[Cited on page 6.](#)]
- [19] G. ’t Hooft and M. J. G. Veltman, “Regularization and Renormalization of Gauge Fields”, *Nucl. Phys. B* **44** (1972) 189. [[Cited on page 7.](#)]
- [20] D. J. Gross and F. Wilczek, “Ultraviolet Behavior of Nonabelian Gauge Theories”, *Phys. Rev. Lett.* **30** (1973) 1343, [,271(1973)]. [[Cited on page 8.](#)]
- [21] H. D. Politzer, “Reliable Perturbative Results for Strong Interactions?”, *Phys. Rev. Lett.* **30** (1973) 1346, [,274(1973)]. [[Cited on page 8.](#)]

- [22] L. V. P. R. de Broglie, “Recherches sur la théorie des quanta”, *Annals Phys.* **2** (1925) 22. [[Cited on page 9.](#)]
- [23] M. N. Chernodub, “Background magnetic field stabilizes QCD string against breaking”, arXiv:1001.0570. [[Cited on pages 10 and 105.](#)]
- [24] J. D. Bjorken, “CURRENT ALGEBRA AT SMALL DISTANCES”, *Conf. Proc.* **670717** (1967) 55–81. [[Cited on page 10.](#)]
- [25] G. Altarelli and G. Parisi, “Asymptotic Freedom in Parton Language”, *Nucl. Phys. B* **126** (1977) 298–318. [[Cited on page 11.](#)]
- [26] Y. L. Dokshitzer, “Calculation of the Structure Functions for Deep Inelastic Scattering and e+ e- Annihilation by Perturbation Theory in Quantum Chromodynamics.”, *Sov. Phys. JETP* **46** (1977) 641–653, [Zh. Eksp. Teor. Fiz. 73, 1216(1977)]. [[Not cited.](#)]
- [27] V. N. Gribov and L. N. Lipatov, “Deep inelastic e p scattering in perturbation theory”, *Sov. J. Nucl. Phys.* **15** (1972) 438, [Yad. Fiz. 15, 781(1972)]. [[Cited on page 11.](#)]
- [28] ZEUS Collaboration, S. Chekanov *et al.*, “A ZEUS next-to-leading-order QCD analysis of data on deep inelastic scattering”, *Phys. Rev. D* **67** (2003) 012007, arXiv:hep-ex/0208023. [[Cited on pages 11, 12, and 105.](#)]
- [29] R. Hagedorn, “Statistical thermodynamics of strong interactions at high energies”, *Nuovo Cimento, Suppl.* **3** (1965) 147. [[Cited on page 13.](#)]
- [30] J. L. Kneur and A. Neveu, “ $\Lambda_{\text{MS}}^{\text{QCD}}$  from Renormalization Group Optimized Perturbation”, *Phys. Rev. D* **85** (2012) 014005, arXiv:1108.3501. [[Cited on page 14.](#)]
- [31] N. R. Council, “Nuclear physics: Exploring the heart of matter”, The National Academies Press, Washington, DC, 2013. [[Cited on pages 14, 17, 20, and 105.](#)]
- [32] M. G. Alford, A. Schmitt, K. Rajagopal, and T. Schäfer, “Color superconductivity in dense quark matter”, *Rev. Mod. Phys.* **80** (2008) 1455, arXiv:0709.4635. [[Cited on page 14.](#)]
- [33] H.-T. Ding, “Recent lattice QCD results and phase diagram of strongly interacting matter”, *Nucl. Phys. A* **931** (2014) 52, arXiv:1408.5236. [[Cited on page 15.](#)]

## BIBLIOGRAPHY

---

- [34] A. Bazavov *et al.*, “Equation of state and QCD transition at finite temperature”, *Phys. Rev. D* **80** (2009) 014504, arXiv:0903.4379. [[Cited on page 15.](#)]
- [35] W. Scheid, H. Muller, and W. Greiner, “Nuclear Shock Waves in Heavy-Ion Collisions”, *Phys. Rev. Lett.* **32** (1974) 741. [[Cited on page 15.](#)]
- [36] E. Lofgren, “ACCELERATOR DIVISION ANNUAL REPORTS, 1 JULY 1972 12/31/1974”, Tech. Rep. LBL-3835, Lawrence Berkeley Laboratory, United States, 1975. [[Cited on page 15.](#)]
- [37] V. R. Pandharipande, D. Pines, and R. A. Smith, “Neutron star structure: theory, observation, and speculation.”, *Astrophys. J.* **208** (1976) 550. [[Cited on page 15.](#)]
- [38] T. L. Ainsworth, E. Baron, G. E. Brown, J. Cooperstein, and M. Prakash, “Equation of State of Dense Nuclear Matter”, *Nucl. Phys. A* **464** (1987) 740. [[Cited on page 15.](#)]
- [39] CERN, “New State of Matter created at CERN”, 2000. [Online; accessed June 11, 2018]. [[Cited on page 16.](#)]
- [40] **PHENIX, PHOBOS, STAR, BRAHMS** Collaboration, T. Ludlam and S. Aronson, “Hunting the quark gluon plasma”, 2005. [[Cited on page 16.](#)]
- [41] M. L. Miller, K. Reygers, S. J. Sanders, and P. Steinberg, “Glauber modeling in high energy nuclear collisions”, *Ann. Rev. Nucl. Part. Sci.* **57** (2007) 205, arXiv:nucl-ex/0701025. [[Cited on page 18.](#)]
- [42] U. W. Heinz, “The Strongly coupled quark-gluon plasma created at RHIC”, *J. Phys. A* **42** (2009) 214003, arXiv:0810.5529. [[Cited on pages 22 and 105.](#)]
- [43] R. Snellings, “Elliptic Flow: A Brief Review”, *New J. Phys.* **13** (2011) 055008, arXiv:1102.3010. [[Cited on pages 22 and 23.](#)]
- [44] P. Kovtun, D. T. Son, and A. O. Starinets, “Viscosity in strongly interacting quantum field theories from black hole physics”, *Phys. Rev. Lett.* **94** (2005) 111601, arXiv:hep-th/0405231. [[Cited on page 23.](#)]
- [45] J.-Y. Ollitrault, “Relativistic hydrodynamics for heavy-ion collisions”, *Eur. J. Phys.* **29** (2008) 275, arXiv:0708.2433. [[Cited on page 23.](#)]

- [46] P. Braun-Munzinger and J. Stachel, “The quest for the quark-gluon plasma”, *Nature* **448** (2007) 302. [[Cited on pages 23 and 106.](#)]
- [47] J. Rafelski and R. Hagedorn, “From Hadron Gas to Quark Matter. 2.”, in “International Symposium on Statistical Mechanics of Quarks and Hadrons Bielefeld, Germany, August 24-31, 1980”, pp. 253–272. 1980. [[Cited on page 24.](#)]
- [48] A. Capella, “Strangeness enhancement in heavy ion collisions”, *Phys. Lett. B* **364** (1995) 175, arXiv:hep-ph/9501331. [[Cited on page 24.](#)]
- [49] F. Becattini and G. Pettini, “Strange quark production in a statistical effective model”, *Phys. Rev. C* **67** (2003) 015205, arXiv:hep-ph/0204340. [[Cited on page 24.](#)]
- [50] J. Rafelski, “Strangeness as a signature of quark gluon plasma, CERN-Alice Summer Student Lecture”, 2011. [Online; accessed June 13, 2018]. [[Cited on pages 25 and 106.](#)]
- [51] C. Blume and C. Markert, “Strange hadron production in heavy ion collisions from SPS to RHIC”, *Prog. Part. Nucl. Phys.* **66** (2011) 834, arXiv:1105.2798. [[Cited on page 24.](#)]
- [52] A. Andronic, P. Braun-Munzinger, and J. Stachel, “Thermal hadron production in relativistic nuclear collisions: The Hadron mass spectrum, the horn, and the QCD phase transition”, *Phys. Lett. B* **673** (2009) 142, arXiv:0812.1186, [Erratum: *Phys. Lett.B*678,516(2009)]. [[Cited on pages 26 and 106.](#)]
- [53] **ALICE** Collaboration, J. Adam *et al.*, “Enhanced production of multi-strange hadrons in high-multiplicity proton-proton collisions”, *Nature Phys.* **13** (2017) 535, arXiv:1606.07424. [[Cited on page 24.](#)]
- [54] M. Cacciari, G. P. Salam, and G. Soyez, “The Anti-k(t) jet clustering algorithm”, *JHEP* **04** (2008) 063, arXiv:0802.1189. [[Cited on page 25.](#)]
- [55] J. D. Bjorken, “Energy Loss of Energetic Partons in Quark - Gluon Plasma: Possible Extinction of High p(t) Jets in Hadron - Hadron Collisions”, 1982. [[Cited on page 26.](#)]
- [56] A. P. S. . A. Stonebraker, “Sketch of jet production in proton-proton and heavy-ion collisions”, 2014. [Online; accessed June 8, 2018]. [[Cited on pages 27 and 106.](#)]

## BIBLIOGRAPHY

---

- [57] **ATLAS** Collaboration, G. Aad *et al.*, “Observation of a Centrality-Dependent Dijet Asymmetry in Lead-Lead Collisions at  $\sqrt{s_{NN}} = 2.77$  TeV with the ATLAS Detector at the LHC”, *Phys. Rev. Lett.* **105** (2010) 252303, arXiv:1011.6182. [[Cited on pages 28 and 106.](#)]
- [58] H. S. Chung, J. Lee, and D. Kang, “Cornell Potential Parameters for S-wave Heavy Quarkonia”, *J. Korean Phys. Soc.* **52** (2008) 1151, arXiv:0803.3116. [[Cited on page 28.](#)]
- [59] T. Matsui and H. Satz, “ $J/\psi$  Suppression by Quark-Gluon Plasma Formation”, *Phys. Lett. B* **178** (1986) 416. [[Cited on page 29.](#)]
- [60] **CMS** Collaboration, A. M. Sirunyan *et al.*, “Suppression of Excited  $\Upsilon$  States Relative to the Ground State in Pb-Pb Collisions at  $\sqrt{s_{NN}}=5.02\text{TeV}$ ”, *Phys. Rev. Lett.* **120** (2018), no. 14, 142301, arXiv:1706.05984. [[Cited on pages 30 and 106.](#)]
- [61] **NA50** Collaboration, M. C. Abreu *et al.*, “Anomalous  $J/\psi$  suppression in Pb-Pb interactions at 158 GeV/c per nucleon”, *Phys. Lett. B* **410** (1997) 337. [[Cited on page 29.](#)]
- [62] **NA50** Collaboration, B. Alessandro *et al.*, “A New measurement of  $J/\psi$  suppression in Pb-Pb collisions at 158-GeV per nucleon”, *Eur. Phys. J. C* **39** (2005) 335, arXiv:hep-ex/0412036. [[Cited on page 29.](#)]
- [63] L. Yan, P. Zhuang, and N. Xu, “Competition between  $J/\psi$  suppression and regeneration in quark-gluon plasma”, *Phys. Rev. Lett.* **97** (2006) 232301, arXiv:nucl-th/0608010. [[Cited on page 29.](#)]
- [64] **ALICE** Collaboration, B. B. Abelev *et al.*, “Centrality, rapidity and transverse momentum dependence of  $J/\psi$  suppression in Pb-Pb collisions at  $\sqrt{s_{NN}}=2.76$  TeV”, *Phys. Lett. B* **734** (2014) 314–327, arXiv:1311.0214. [[Cited on pages 31 and 106.](#)]
- [65] **CMS** Collaboration, S. Chatrchyan *et al.*, “Study of Z production in PbPb and pp collisions at  $\sqrt{s_{NN}} = 2.76$  TeV in the dimuon and dielectron decay channels”, *JHEP* **03** (2015) 022, arXiv:1410.4825. [[Cited on pages 32 and 107.](#)]
- [66] A. D. Rosso, “Particle kickers. Aiguiller les particules”, Jun 2014. [[Cited on pages 36 and 107.](#)]
- [67] **ALICE** Collaboration, K. Aamodt *et al.*, “The ALICE experiment at the CERN LHC”, *JINST* **3** (2008) S08002. [[Cited on page 35.](#)]

- [68] **ATLAS** Collaboration, G. Aad *et al.*, “The ATLAS Experiment at the CERN Large Hadron Collider”, *JINST* **3** (2008) S08003. [[Cited on page 35.](#)]
- [69] **CMS** Collaboration, S. Chatrchyan *et al.*, “The CMS Experiment at the CERN LHC”, *JINST* **3** (2008) S08004. [[Cited on pages 36, 39, 42, 43, 45, 50, and 107.](#)]
- [70] **LHCb** Collaboration, A. A. Alves, Jr. *et al.*, “The LHCb Detector at the LHC”, *JINST* **3** (2008) S08005. [[Cited on page 36.](#)]
- [71] J. Jowett *et al.*, “The 2015 Heavy-Ion Run of the LHC”, in “Proceedings, 7th International Particle Accelerator Conference (IPAC 2016): Busan, Korea, May 8-13, 2016”, p. TUPMW027. 2016. [[Cited on pages 37, 38, and 107.](#)]
- [72] J. Jowett *et al.*, “The 2016 Proton-Nucleus Run of the LHC”, in “Proceedings, 8th International Particle Accelerator Conference (IPAC 2017): Copenhagen, Denmark, May 14-19, 2017”, p. TUPVA014. 2017. [[Cited on pages 39 and 107.](#)]
- [73] J. Jowett, “Colliding Heavy Ions in the LHC”, in “Proceedings, 9th International Particle Accelerator Conference (IPAC 2018): Vancouver, BC, Canada, April 29 - May 4, 2018”, p. TUXGBD2. 2018. [[Cited on pages 40 and 103.](#)]
- [74] T. Sakuma and T. McCauley, “Detector and Event Visualization with SketchUp at the CMS Experiment”, *J. Phys. Conf. Ser.* **513** (2014) 022032, arXiv:1311.4942. [[Cited on pages 41 and 107.](#)]
- [75] **CMS Collaboration** Collaboration, C. Battilana, “The CMS muon system status and upgrades for LHC run-2 and performance of muon reconstruction with 13 TeV data”, Tech. Rep. CMS-CR-2016-437, CERN, Geneva, Dec 2016. [[Cited on page 42.](#)]
- [76] **CMS** Collaboration, J. Mans, J. Anderson, B. Dahmes, P. de Barbaro, J. Freeman, T. Grassi, E. Hazen, J. Mans, R. Ruchti, I. Schimdt, *et al.*, “CMS Technical Design Report for the Phase 1 Upgrade of the Hadron Calorimeter”, 2012. [[Cited on pages 42, 46, and 107.](#)]
- [77] **CMS** Collaboration, A. Tapper and D. Acosta, “CMS Technical Design Report for the Level-1 Trigger Upgrade”, 2013. [[Cited on pages 42 and 54.](#)]
- [78] **CMS** Collaboration, A. Benaglia, “The CMS ECAL performance with examples”, *JINST* **9** (2014) C02008. [[Cited on pages 45 and 107.](#)]

## BIBLIOGRAPHY

---

- [79] **CMS** Collaboration, G. Abbiendi, “The CMS muon system in Run2: preparation, status and first results”, *PoS EPS-HEP2015* (2015) 237, arXiv:1510.05424. [Cited on pages 48 and 107.]
- [80] **CMS** Collaboration, S. Chatrchyan *et al.*, “Performance of the CMS Drift Tube Chambers with Cosmic Rays”, *JINST* **5** (2010) T03015, arXiv:0911.4855. [Cited on pages 49 and 107.]
- [81] A. M. *et al.*, “Beam Test Results on Resistive Plate Chambers for the CMS Experiment”, 1997. [Cited on pages 51 and 107.]
- [82] C. Collaboration, “Resistive Plate Chambers”, 2011. [Online; accessed July 7, 2018]. [Cited on pages 51 and 107.]
- [83] **CMS** Collaboration, V. Khachatryan *et al.*, “The CMS trigger system”, *JINST* **12** (2017), no. 01, P01020, arXiv:1609.02366. [Cited on pages 51 and 52.]
- [84] **CMS** Collaboration, J. J. Brooke, D. G. Cussans, R. Frazier, G. Heath, D. Machin, and D. Newbold, 2003, unpublished. [Cited on pages 53 and 107.]
- [85] A. Zabi *et al.*, “Triggering on electrons, jets and tau leptons with the CMS upgraded calorimeter trigger for the LHC RUN II”, *JINST* **11** (2016), no. 02, C02008. [Cited on page 55.]
- [86] J. Fulcher, J. Lingemann, D. Rabady, T. Reis, and H. Sakulin, “The New Global Muon Trigger of the CMS Experiment”, *IEEE Trans. Nucl. Sci.* **64** (2017), no. 6, 1467. [Cited on page 55.]
- [87] J.-M. André *et al.*, “Performance of the new DAQ system of the CMS experiment for run-2”, in “Proceedings, 20th IEEE-NPSS Real Time Conference (RT2016): Padua, Italy, June 5-10, 2016”. 2016. [Cited on page 56.]
- [88] R. Fruhwirth, “Application of Kalman filtering to track and vertex fitting”, *Nucl. Instrum. Meth.* **A262** (1987) 444. [Cited on pages 56 and 58.]
- [89] **CMS** Collaboration, A. M. Sirunyan *et al.*, “Performance of the CMS muon detector and muon reconstruction with proton-proton collisions at  $\sqrt{s} = 13$  TeV”, *JINST* **13** (2018), no. 06, P06015, arXiv:1804.04528. [Cited on page 57.]
- [90] D. Barney, “CMS Detector Slice”, CMS Collection., Jan 2016, unpublished. [Cited on pages 58 and 108.]

- [91] **CMS** Collaboration, A. M. Sirunyan *et al.*, “Particle-flow reconstruction and global event description with the cms detector”, *JINST* **12** (2017) P10003, arXiv:1706.04965. [[Cited on page 60.](#)]
- [92] **CMS Collaboration** Collaboration, “Performance of missing energy reconstruction in 13 TeV pp collision data using the CMS detector”, Tech. Rep. CMS-PAS-JME-16-004, CERN, Geneva, 2016. [[Cited on page 60.](#)]
- [93] **CMS** Collaboration, S. S. Ghosh, “Performance of MET reconstruction and pileup mitigation techniques in CMS”, *Nucl. Part. Phys. Proc.* **273-275** (2016) 2512–2514, arXiv:1502.05207. [[Cited on page 60.](#)]
- [94] **CMS** Collaboration, V. Khachatryan *et al.*, “Study of W boson production in pPb collisions at  $\sqrt{s_{\text{NN}}} = 5.02 \text{ TeV}$ ”, *Phys. Lett.* **B750** (2015) 565–586, arXiv:1503.05825. [[Cited on page 65.](#)]
- [95] **ALICE** Collaboration, K. Senosi, “Measurement of W-boson production in p-Pb collisions at the LHC with ALICE”, *PoS Bormio2015* (2015) 042, arXiv:1511.06398. [[Cited on page 65.](#)]
- [96] **ATLAS** Collaboration, M. Dumançifá, “W and Z boson production in 5.02 TeV pp and p+Pb collisions with the ATLAS detector”, *Nucl. Part. Phys. Proc.* **289-290** (2017) 193–196, arXiv:1704.00298. [[Cited on page 65.](#)]
- [97] E. Rutherford, “Uranium radiation and the electrical conduction produced by it”, *Philos. Mag.* **47** (1899) 109. [[Cited on page 66.](#)]
- [98] J. Chadwick, “Intensitätsverteilung im magnetischen Spektrum von  $\beta$ -Strahlen von Radium B+C”, *Verhandlungen der deutschen physikalischen Gesellschaft* **16** (1914) 383. [[Cited on page 66.](#)]
- [99] J. Chadwick and C. D. Ellis, “A Preliminary Investigation of the Intensity Distribution in the  $\beta$ -Ray Spectra of Radium B and C”, *Proceedings of the Cambridge Philosophical Society* **21** (1922) 274. [[Cited on page 66.](#)]
- [100] W. Pauli, “Fünf Arbeiten zum Ausschliessungsprinzip und zum Neutrino”, Wissenschaftliche Buchgesellschaft, [Abt. Verlag], 1977. [[Cited on page 66.](#)]
- [101] K. Winter, “Neutrino physics”, Cambridge University Press, 1991. [[Cited on page 66.](#)]

## BIBLIOGRAPHY

---

- [102] J. Chadwick, “Possible Existence of a Neutron”, *Nature* **129** (1932) 312. [[Cited on page 66.](#)]
- [103] E. Fermi, “Collected Papers of Enrico Fermi”, University of Chicago Press, 1965. [[Cited on page 66.](#)]
- [104] E. Fermi, “Versuch einer Theorie der  $\beta$ -Strahlen. I”, *Zeitschrift für Physik* **88** (1934) 161. [[Cited on page 66.](#)]
- [105] T. D. Lee and C. N. Yang, “Question of Parity Conservation in Weak Interactions”, *Phys. Rev.* **104** (1956) 254. [[Cited on page 67.](#)]
- [106] C. S. Wu, E. Ambler, R. W. Hayward, D. D. Hoppes, and R. P. Hudson, “Experimental Test of Parity Conservation in Beta Decay”, *Phys. Rev.* **105** (1957) 1413. [[Cited on page 67.](#)]
- [107] M. Goldhaber, L. Grodzins, and A. W. Sunyar, “Helicity of Neutrinos”, *Phys. Rev.* **109** (1958) 1015. [[Cited on page 67.](#)]
- [108] E. C. G. Sudarshan and R. E. Marshak, “Origin of the Universal VÄA theory”, *AIP Conf. Proc.* **300** (1994) 110, [,0001(1984)]. [[Cited on page 67.](#)]
- [109] J. H. Christenson, J. W. Cronin, V. L. Fitch, and R. Turlay, “Evidence for the  $2\pi$  Decay of the  $K_2^0$  Meson”, *Phys. Rev. Lett.* **13** (1964) 138–140. [[Cited on page 67.](#)]
- [110] M. Kobayashi and T. Maskawa, “CP Violation in the Renormalizable Theory of Weak Interaction”, *Prog. Theor. Phys.* **49** (1973) 652–657. [[Cited on page 67.](#)]
- [111] N. Cabibbo, “Unitary Symmetry and Leptonic Decays”, *Phys. Rev. Lett.* **10** (1963) 531–533, [,648(1963)]. [[Cited on page 67.](#)]
- [112] S. W. Herb *et al.*, “Observation of a Dimuon Resonance at 9.5-GeV in 400-GeV Proton-Nucleus Collisions”, *Phys. Rev. Lett.* **39** (1977) 252–255. [[Cited on page 67.](#)]
- [113] **CDF** Collaboration, F. Abe *et al.*, “Observation of top quark production in  $\bar{p}p$  collisions”, *Phys. Rev. Lett.* **74** (1995) 2626–2631, arXiv:hep-ex/9503002. [[Cited on page 67.](#)]
- [114] P. A. M. Dirac, “The Principles of Quantum Mechanics”, Clarendon Press, 1930. [[Cited on page 67.](#)]

- [115] S. L. Glashow, “The renormalizability of vector meson interactions”, *Nucl. Phys.* **10** (1959) 107. [[Cited on pages 67 and 69.](#)]
- [116] S. Weinberg, “A Model of Leptons”, *Phys. Rev. Lett.* **19** (1967) 1264. [[Cited on page 67.](#)]
- [117] A. Salam, “Weak and Electromagnetic Interactions”, *Conf. Proc. C* **680519** (1968) 367. [[Cited on pages 67 and 69.](#)]
- [118] N. M. A. 2014, “The Nobel Prize in Physics 1979”.  
[http://www.nobelprize.org/nobel\\_prizes/physics/laureates/1979/](http://www.nobelprize.org/nobel_prizes/physics/laureates/1979/), 2018.  
Accessed: 2018-05-23. [[Cited on page 67.](#)]
- [119] G. t. Hooft, “Renormalizable Lagrangians for massive Yang-Mills fields”, *Nuclear Physics B* **35** (1971) 167. [[Cited on page 68.](#)]
- [120] G. t. Hooft and M. Veltman, “Regularization and renormalization of gauge fields”, *Nuclear Physics B* **44** (1972) 189. [[Cited on page 68.](#)]
- [121] C. Rubbia, P. McIntyre, and D. Cline, *Producing Massive Neutral Intermediate Vector Bosons with Existing Accelerators*, pp. 683–687. Vieweg+Teubner Verlag, Wiesbaden, 1977. [[Cited on page 68.](#)]
- [122] S. van der Meer, “Stochastic damping of betatron oscillations in the ISR”, Tech. Rep. CERN-ISR-PO-72-31. ISR-PO-72-31, CERN, Geneva, Aug 1972. [[Cited on page 68.](#)]
- [123] G. Arnison *et al.*, “Experimental observation of isolated large transverse energy electrons with associated missing energy at  $\sqrt{s}=540$  GeV”, *Phys. Lett. B* **122** (1983) 103. [[Cited on page 68.](#)]
- [124] M. Banner *et al.*, “Observation of single isolated electrons of high transverse momentum in events with missing transverse energy at the CERN pp collider”, *Phys. Lett. B* **122** (1983) 476. [[Cited on page 68.](#)]
- [125] **UA1** Collaboration, G. Arnison *et al.*, “Experimental Observation of Lepton Pairs of Invariant Mass Around 95-GeV/c\*\*2 at the CERN SPS Collider”, *Phys. Lett. B* **126** (1983) 398, [,7.55(1983)]. [[Cited on page 68.](#)]
- [126] **UA2** Collaboration, P. Bagnaia *et al.*, “Evidence for  $Z_0 \rightarrow e^+ e^-$  at the CERN anti-p p Collider”, *Phys. Lett. B* **129** (1983) 130, [,7.69(1983)]. [[Cited on page 68.](#)]

## BIBLIOGRAPHY

---

- [127] N. M. A. 2014, “The Nobel Prize in Physics 1984”.  
[http://www.nobelprize.org/nobel\\_prizes/physics/laureates/1984/](http://www.nobelprize.org/nobel_prizes/physics/laureates/1984/), 2018.  
Accessed: 2018-05-23. [Cited on page 68.]
- [128] S. Myers, “The LEP Collider, from design to approval and commissioning”, CERN, Geneva, 1991. Delivered at CERN, 26 Nov 1990. [Cited on page 68.]
- [129] **DØ Collaboration** Collaboration, V. M. Abazov *et al.*, “Improved  $W$  boson mass measurement with the DØ detector”, *Phys. Rev. D* **66** Jul (2002) 012001. [Cited on page 68.]
- [130] R. R. Wilson, “The Tevatron”, *Phys. Today* **30** (1977) 23. [Cited on page 68.]
- [131] **European Muon** Collaboration, J. J. Aubert *et al.*, “The ratio of the nucleon structure functions  $F_{2n}$  for iron and deuterium”, *Phys. Lett. B* **123** (1983) 275–278. [Cited on page 72.]
- [132] **European Muon** Collaboration, M. Arneodo *et al.*, “Shadowing in Deep Inelastic Muon Scattering from Nuclear Targets”, *Phys. Lett. B* **211** (1988) 493–499. [Cited on page 72.]
- [133] **New Muon** Collaboration, D. o. Allasia, “Inelastic  $j/\psi$  production in deep inelastic scattering from hydrogen and deuterium and the gluon distribution of free nucleons”, *Physics Letters B* **258** (1991), no. 3, 493 – 498. [Cited on page 72.]
- [134] S. Dulat, T.-J. Hou, J. Gao, M. Guzzi, J. Huston, P. Nadolsky, J. Pumplin, C. Schmidt, D. Stump, and C. P. Yuan, “New parton distribution functions from a global analysis of quantum chromodynamics”, *Phys. Rev. D* **93** (2016), no. 3, 033006, arXiv:1506.07443. [Cited on pages 72, 73, and 81.]
- [135] K. J. Eskola, V. J. Kolhinen, and C. A. Salgado, “The Scale dependent nuclear effects in parton distributions for practical applications”, *Eur. Phys. J. C* **9** (1999) 61–68, arXiv:hep-ph/9807297. [Cited on page 73.]
- [136] K. J. Eskola, H. Paukkunen, and C. A. Salgado, “An Improved global analysis of nuclear parton distribution functions including RHIC data”, *JHEP* **07** (2008) 102, arXiv:0802.0139. [Cited on page 73.]
- [137] K. J. Eskola, H. Paukkunen, and C. A. Salgado, “EPS09: A new generation of NLO and LO nuclear parton distribution functions”, *JHEP* **04** (2009) 065, arXiv:0902.4154. [Cited on page 73.]

- [138] D. de Florian, R. Sassot, P. Zurita, and M. Stratmann, “Global Analysis of Nuclear Parton Distributions”, *Phys. Rev. D* **85** (2012) 074028, arXiv:1112.6324. [[Cited on page 73.](#)]
- [139] K. Kovarik *et al.*, “nCTEQ15 - Global analysis of nuclear parton distributions with uncertainties in the CTEQ framework”, *Phys. Rev. D* **93** (2016), no. 8, 085037, arXiv:1509.00792. [[Cited on pages 73 and 81.](#)]
- [140] K. J. Eskola, P. Paakkinen, H. Paukkunen, and C. A. Salgado, “EPPS16: Nuclear parton distributions with LHC data”, *Eur. Phys. J. C* **77** (2017), no. 3, 163, arXiv:1612.05741. [[Cited on pages 73 and 81.](#)]
- [141] F. Arleo, É. Chapon, and H. Paukkunen, “Scaling properties of inclusive  $W^\pm$  production at hadron colliders”, *Eur. Phys. J. C* **76** (2016), no. 4, 214, arXiv:1509.03993. [[Cited on pages 75 and 77.](#)]
- [142] **CMS Collaboration** Collaboration, “Luminosity calibration for the pPb/Pbp 2016 runs”, Tech. Rep. CMS-LUM-AN-17-002, CERN, Geneva, 2017. [[Cited on pages 79, 80, and 108.](#)]
- [143] J. M. Campbell and R. K. Ellis, “MCFM for the Tevatron and the LHC”, *Nucl. Phys. Proc. Suppl.* **205-206** (2010) 10–15, arXiv:1007.3492. [[Cited on page 81.](#)]



## LIST OF TABLES

1.1 Basic properties of quarks, leptons and bosons from the SM. The table includes the mass, electric charge, spin and type of interactions of each particle. The values are taken from Ref. [12] . . . . .	5
2.1 LHC beam parameters during the highest luminosity physics fills. The luminosity values are averages for CMS. Information extracted from Ref. [73] . . . . .	40
4.1 Experimental values of the mass, width and branching fractions of weak bosons extracted from the PDG [12]. . . . .	71
4.2 Summary of the information of EPS09, EPPS16 and nCTEQ15 nuclear PDFs. . . . .	76
4.3 Results of the $\chi^2$ statistical test between the measurements and the theory calculations from the CT14 PDF, CT14+EPPS16 nPDF and CT14+nCTEQ15 nPDF models. The value of the $\chi^2$ , the number of degrees of freedom (ndf) and the $\chi^2$ probability (Prob.), are presented for the W differential cross sections, the muon charge asymmetry, the charged muon forward-backward ratios, and the forward-backward ratio of all muons, respectively. . . . .	85
<b>TABLE</b>	<b>Page</b>



## LIST OF FIGURES

1.1	Feynman diagrams of the QCD vertices for quark-gluon coupling (left), triple gluon self-coupling (middle) and quadri gluon self-coupling (right). . . . .	7
1.2	Feynman diagrams of 1-loop contributions to pQCD. . . . .	7
1.3	Summary of measurements of $\alpha_s$ as a function of the energy scale $Q$ . Figure taken from the PDG [12] . . . . .	8
1.4	Sketch of the gluon string breaking between a quark $Q$ and an anti-quark $\bar{Q}$ due to $q\bar{q}$ pair creation. Figure taken from Ref. [23] . . . . .	10
1.5	Feynman diagram of deep inelastic scattering of electrons against protons . .	12
1.6	NLO QCD fits to the to the ZEUS $F_2$ structure function data from 1996, 1997 and proton fixed-target at HERA. The error bands of the fit represent the total experimental uncertainty from both correlated and uncorrelated sources. Figure taken from Ref. [28] . . . . .	12
1.7	Feynman diagram of neutral charged Drell-Yan process . . . . .	13
1.8	Schematic of the QCD phase diagram for nuclear matter. The solid lines show the phase boundaries and the solid circle represents the critical point. Figure taken from Ref. [31] . . . . .	14
1.9	Illustration of two nucleus with impact parameter $b$ before (left) and after (right) colliding. Figure taken from Ref. [31] . . . . .	17
1.10	Schematic representation of the optical Glauber model geometry. . . . .	18
1.11	Schematic sketch of the evolution of a relativistic heavy ion collision. The wavy lines represent photons while the arrows correspond to jets. Figure taken from Ref. [31] . . . . .	20
1.12	Sketch of the deformed medium and the elliptic flow produced in non-central heavy-ion collisions. Figure taken from Ref. [42] . . . . .	22

1.13 Elliptic flow distribution of as a function of transverse momemtum for $\pi^\pm$ mesons, $K_s^0$ mesons, antiprotons and $\Lambda$ baryons measured by STAR collaboration in Au-Au collisions at $\sqrt{s_{NN}} = 200$ GeV. The results are compared with relativistic hydrodynamic calculations. Figure taken from Ref. [46] . . . . .	23
1.14 Sketch of the production of strange hadrons via gluon fusion in the QGP. Figure taken from Ref. [50] . . . . .	25
1.15 Energy distribution of the relative production ratios $K^+/\pi^+$ and $\Lambda/\pi^-$ at mid-rapidity measured at AGS (E802, E866, E895, E896) and SPS (NA44, NA49, NA57) in central Pb-Pb collisions, and at RHIC (STAR, PHENIX) in central Au-Au collisions. The solid line is the result of a statistical model calculation. The dotted line shows the $K^+/\pi^+$ ratio including the additional effect of higher mass resonances. The dashed lines show the energy dependence of the temperature (upper panel) and baryonic density (lower panel). Figure taken from Ref. [52] . . . . .	26
1.16 Sketch of the production mechanism of two jets in proton-proton (top) and heavy-ions (bottom) collisons. Figure taken from Ref. [56] . . . . .	27
1.17 Dijet asymmetry measured by the ATLAS collaboration in lead-lead collisions at $\sqrt{s_{NN}} = 2.76$ TeV (points) and proton-proton collisions at $\sqrt{s} = 7$ TeV (open circles). The top panel shows the dijet asymmetry distributions and unquenched HIJING with superimposed PYTHIA dijets (solid yellow histograms), as a function of collision centrality. The bottom panel shows the distribution of the azimuthal angle between the two jets $\Delta\phi$ , for data and HIJING+PYTHIA, also as a function of centrality. Figure taken from Ref. [57]	28
1.18 Dimuon invariant mass distribution measured by the CMS collaboration in Pb-Pb collisions at $\sqrt{s_{NN}} = 5.02$ TeV. The total fit (solid blue line), the background component (dot-dashed blue line) and the individual $\Upsilon(1S)$ , $\Upsilon(2S)$ and $\Upsilon(3S)$ mass peaks (dotted gray lines) are shown. The dashed red line represents the p-p signal shapes added on top of the Pb-Pb background and normalized to the $\Upsilon(1S)$ mass peak in Pb-Pb. Figure taken from Ref. [60] . . . . .	30
1.19 Nuclear modification factor of $J/\psi$ meson as a function of transverse momentum measured by the ALICE collaboration in the 0% – 20% most central Pb-Pb collisions at $\sqrt{s_{NN}} = 2.76$ TeV compared to results from the PHENIX collaboration measured in the 0% – 20% most central Au-Au collisions at $\sqrt{s_{NN}} = 200$ GeV. Figure taken from Ref. [64] . . . . .	31

1.20 Nuclear modification factor $R_{AA}$ of $Z \rightarrow e^+e^-$ (blue squares) and $Z \rightarrow \mu^+\mu^-$ (red circles) events as a function of the number of participants measured by the CMS collaboration in Pb-Pb collisions at $\sqrt{s_{NN}} = 2.56$ TeV. The open points represent the centrality-integrated $R_{AA}$ and the vertical lines (boxes) correspond to statistical (systematic) uncertainties. The grey bar at $R_{AA} = 1$ represents the uncertainty of the luminosity determined in proton-proton collisions. Figure taken from Ref. [65]	32
2.1 Schematic diagram of the LHC injection chain for protons and Pb nuclei. The proton and Pb ion trajectories are indicated with red and blue arrows, accordingly. The location of each LHC detector is also included.	34
2.2 Schematic diagram of the LHC layout. Figure taken from Ref. [66].	36
2.3 Integrated nucleon-pair luminosity delivered by the LHC to each experiment during Pb-Pb collisions at $\sqrt{s_{NN}} = 5.02$ TeV. The integrated luminosity of p-Pb collisions at $\sqrt{s_{NN}} = 5.02$ TeV and Pb-Pb collisions at $\sqrt{s_{NN}} = 2.76$ TeV are included for comparison. Figure taken from Ref. [71]	38
2.4 Integrated proton-nucleus luminosity delivered by the LHC to each experiment during p-Pb collisions at $\sqrt{s_{NN}} = 8.16$ TeV (solid lines). The integrated luminosity of p-Pb collisions at $\sqrt{s_{NN}} = 5.02$ TeV (dashed lines) is included for comparison. Figure taken from Ref. [72]	39
2.5 Cutaway view of the CMS detector in its configuration used during 2015 and 2016. The labels and basic details of each sub-detector are included. [74]	41
2.6 Schematic of the coordinate system used in the CMS experiment.	42
2.7 View of the CMS tracker in the rz-plane. Each line represents a detector module. Figure taken from Ref. [69].	43
2.8 Schematic layout [69] (right) of the CMS electromagnetic calorimeter, and its corresponding one-quarter geometric view [78] (left).	45
2.9 Geometric view of one quarter of the CMS detector, displaying the subdetectors of the hadron calorimeter. Figure taken from Ref. [76].	46
2.10 Geometric view of one quadrant the CMS detector in the rz-plane. Each chamber of the muon system is shown. Figure taken from Ref. [79].	48
2.11 Schematic layout of a DT cell (left) and a DT chamber (right). Figures taken from [80].	49
2.12 Schematic layout of a CSC. Figure taken from [69].	50
2.13 Cross section view (left) [81] and exploded view (right) [82] of a RPC module.	51
2.14 Diagram of the legacy L1 trigger of CMS. Figure taken from Ref. [84]	53

---

LIST OF FIGURES

2.15 Diagram of the CMS L1 trigger used in 2016. . . . .	54
2.16 Cross section view of the CMS detector showing how particles interact in the CMS. The different types of muon tracks are indicated in boxes. Figure taken from Ref. [90]. . . . .	58
4.1 Feynman diagram of the decay modes of $W^+$ (left) and $W^-$ (right) bosons to fermions. . . . .	71
4.2 Feynman diagram of LO $W$ boson production to final state leptons in $pPb$ collisions . . . . .	76
4.3 Production cross sections for $W^+ \rightarrow \mu^+ \nu_\mu$ (left) and $W^- \rightarrow \mu^- \bar{\nu}_\mu$ (right), as a function of the muon pseudorapidity in the center-of-mass frame. The brackets represent the statistical and systematic uncertainties summed in quadrature, while the error bars show the statistical uncertainties only. The global luminosity uncertainty of $\pm 3.4\%$ [142] is not shown. . . . .	80
4.4 Muon charge asymmetry as a function of the muon pseudorapidity in the center-of-mass frame. The brackets represent the statistical and systematic uncertainties summed in quadrature, while the error bars show the statistical uncertainties only. . . . .	81
4.5 Forward-backward ratios, for the positive (left), all (middle) and negative (right) charged muons. The brackets represent the statistical and systematic uncertainties summed in quadrature, while the error bars show the statistical uncertainties only. . . . .	82
4.6 Differential cross sections for $W^+ \rightarrow \mu^+ \nu_\mu$ (left) and $W^- \rightarrow \mu^- \bar{\nu}_\mu$ (right), as a function of the muon pseudorapidity in the center-of-mass frame. Errors bars represent the statistical uncertainties, while the brackets represent the statistical and systematic uncertainties summed in quadrature. The global luminosity uncertainty of $\pm 3.4\%$ is not displayed. Theoretical predictions with (CT14+EPPS16 shown in dashed green line and CT14+nCTEQ15 shown in dashed brown line) and without (CT14, solid red line) PDF nuclear modifications are also shown, with the uncertainty bands. All theory uncertainty bands include PDF uncertainties. . . . .	83

- 4.7 Muon charge asymmetry of  $W \rightarrow \mu\nu_\mu$ , given for each muon  $\eta_{CM}$  bin. Errors bars represent the statistical uncertainties, while the brackets represent the statistical and systematic uncertainties summed in quadrature. Theoretical predictions with (CT14+EPPS16 shown in dashed green line and CT14+nCTEQ15 shown in dashed brown line) and without (CT14, solid red line) PDF nuclear modifications are also shown, with the uncertainty bands. All theory uncertainty bands include PDF uncertainties. . . . . 84
- 4.8 Forward-backward ratio of  $W \rightarrow \mu\nu_\mu$ , given for each muon  $\eta_{CM}$  bin separated in negative (left), all (middle) and positive (right) charged muons. Errors bars represent the statistical uncertainties, while the brackets represent the statistical and systematic uncertainties summed in quadrature. Theoretical predictions with (CT14+EPPS16 shown in dashed green line and CT14+nCTEQ15 shown in dashed brown line) and without (CT14, solid red line) PDF nuclear modifications are also shown, with the uncertainty bands. All theory uncertainty bands include PDF uncertainties. . . . . 84

<b>FIGURE</b>	<b>Page</b>
---------------	-------------

